Materials physics of half-metallic magnetic oxide films by Pulsed Laser Deposition: Controlling the crystal structure and near-surface properties of Sr_2FeMoO_6 and CrO_2 films

by

Helia Jalili

A thesis
presented to the University of Waterloo
in fulfillment of the
thesis requirement for the degree of
Doctor of Philosophy
in
Physics

Waterloo, Ontario, Canada, 2008

AUTHOR'S DECLARATION

I hereby declare that I am the sole author of this thesis. This is a true copy of the thesis, including any required final revisions, as accepted by my examiners.

I understand that my thesis may be made electronically available to the public.

Abstract

The idea of half-metallic ferromagnets was first introduced by de Groot et al. in 1983 based on their calculations. The density of state at the Fermi level for half-metallic ferromagnet is completely polarized, meaning that only one of the spin up or spin down channel exists and has metallic behaviour while the other spin channel behaves as a semiconductor or insulator. This unusual electronic structure can be seen in different materials including Sr_2FeMoO_6, CrO_2 and Mn-based Heusler alloys. The high spin polarization degree of the half-metallic ferromagnets makes them a perfect candidate to be used as a spin-injector/detector in spin-based electronics device (spintronics). However, the degree of spin polarization of these materials, particularly in the multilayered structure spintronic devices, strongly depends on the surface/interface quality and the presence of defects, which was the subject of the present study. Pulsed laser deposition (PLD) has been used to grow two examples of the half-metallic ferromagnets, namely, Sr_2FeMoO_6 and CrO_2. The effects of the growth conditions (deposition temperature, gas pressure, laser power, target-to-substrate distance, post-annealing) and of the substrate lattice mismatch and thickness evolution have been studied. By optimizing the growth conditions, nanocrystalline Sr_2FeMoO_6 films have been grown on a Si(100) substrate for the first time. This single-phase Sr_2FeMoO_6 film was obtained at a temperature as low as 600°C, and it exhibits a high saturation magnetic moment of 3.4 μ_B per formula unit at 77 K. By using glancing-incidence X-ray diffraction with different incident beam angles, the crystal structure of the film was sampled as a function of depth. Despite the lack of good lattice matching with the Si substrate, a preferential orientation of the nanocrystals in the film was observed for the as-grown Sr_2FeMoO_6 films thicker than 60 nm. Furthermore, effects of the deposition temperature on the epitaxial growth of the Sr_2FeMoO_6 films on MgO(001) have been studied by means of high-resolution X-ray diffraction. The film grown at 800°C was post-annealed in oxygen, producing epitaxial films of $SrMoO_4$ on top of the Sr_2FeMoO_6 film. The corresponding magnetization data showed that the post-annealing treatment lowered the saturation magnetic moment from 3.4 μ_B per formula unit (or /f.u.) for the as-grown Sr_2FeMoO_6 film to 1.4 μ_B/f.u. after annealing. X-ray photoemission measurements as a

function of sputtering time further revealed the presence of $SrMoO_4$ on both the as-grown and annealed films, and their corresponding depth profiles indicated a thicker $SrMoO_4$ overlayer on the annealed film. The intensity ratios of the 3d features of Mo^{4+}, Mo^{5+}, and Mo^{6+} for Sr_2FeMoO_6 remained unchanged with sputtering depth (after 160 s of sputtering), supporting the conclusion that the observed secondary phase ($SrMoO_4$) was formed predominantly on the surface and not in the sub-grain boundaries of the as-grown Sr_2FeMoO_6 film. The epitaxial growth evolution of Sr_2FeMoO_6 films of different thickness on substrates of MgO(001), $SrTiO_3$(100) and $LaAlO_3$(100) have also been studied. For each thickness, surface morphology, grain size, film epitaxy, and crystal quality were determined by atomic force microscopy and X-ray diffraction (ω-2θ scan and reciprocal space mapping). For thicker films (~120 nm), high resolution X-ray diffraction studies revealed that $SrMoO_4$ and other parasitic phases tend to forms on $SrTiO_3$ and $LaAlO_3$ substrates, but not on those grown on MgO substrates.

As a second part of the project, single-phase CrO_2 nanostructured thin films have been grown for the first time directly on MgO(001) by PLD from a metallic Cr target in an O_2 environment. X-ray diffraction shows that these films are strained and consist of CrO_2 crystallites with two possible epitaxial relationships to the substrate: either CrO_2(110) or CrO_2(200) is parallel to MgO(001). X-ray photoemission further confirms that the films are primarily CrO_2 covered with a thin CrO_3 overlayer, and indicates its complete synthesis without any residual metallic Cr.

Acknowledgements

It is my pleasure to thank many people who made this thesis possible. First and foremost, I would like to thank my thesis advisor Prof. Tong Leung for his insight, guidance and unbelievable patience. He provided me with the freedom to do things in the way that I thought it should be done. One simply could not wish for a better and friendlier advisor. My deep gratitude goes to Dr. Nina Heinig for her unlimited help on various parts of this thesis, numerous scientific discussions, many constructive comments, all her excitement even when nothing was working properly in the lab. I would also like to thank Prof. F. Razavi for his time, friendly advices and letting us using the SQUID magnetometer.

I gratefully acknowledge the constant and invaluable academic and personal support received from all faculty members of Guelph-Waterloo Physics Institute; Prof. T. Hesjedal, Prof. R. Hill, Prof. D. Sullivan and Prof. J. Kycia for their suggestion and guidance to improve my work. My appreciation goes to WATlab members, for all their help and good time that we had. I would also like to thank administrative assistant in Physics Dept., machine shop and electronic shop for their great jobs. My gratitude goes to my neighbors C. Treimanis, G. Jocys and landlady L. Buckton, for their goodwill and for making my apartment such a nice place to live. My sincere thanks to my in-laws Diliara and Eugene for their warm wishes and love. I am very grateful for the company of my friends and relatives, thank you very much for being there for me.

Finally, I am forever indebted to my family, my parents Hayedeh and Hassan, my fiancé Iouli Gordon and my sister Kimia, for their understanding, love, support and encouragement when it was most required. Thanks for believing in me. I can only hope you are as proud of me as I am of you.

Dedication

I would like to dedicate this thesis to my parents and my grand parents for all their love and support.

Table of Contents

List of Figures

List of Tables

Chapter 1
Half-Metallic Systems: Background and Applications

1.1 Motivation and structure of the thesis

The discovery of Giant Magnetoresistance (GMR) has been cited as the first demonstration of a nanoscience application and has been awarded the Physics Nobel Prize in 2007 [1]. The idea of GMR has generated a new field of spin-based electronics, or "spintronics". Spintronics refers to phenomena where the spin degree of freedom of the electron should be taken into account for electronic transport properties, and in the last 10 years it has had a huge impact on the data storage industry [2]. Using spintronic devices can have several advantages [3,4]:

- Enhanced multifunctionality of devices, since data storage and processing is not operating with electric charge alone.
- Electric/magnetic field or current can be easily used to manipulate the devices.
- Long coherence and relaxation time of the spin have potential for producing non-volatile memory.
- Devices can be smaller, faster, and consume less energy.

Attempts to replace current microelectronic devices with nanoscale devices has led to a search for new materials with multifunctional properties (multitasking materials that can be manipulated by independent sources). In this regard, transition metal oxides are of great interest due to their wide variety of physical properties, including ferromagnetism, antiferromagnetism, ferroelectricity, superconductivity and many more. They are good candidate materials for fabricating a spintronic device.

The magnitude of any spintronic effect depends strongly on the degree of spin-polarization of the density of states of magnetic materials at the Fermi level. Transition magnetic oxides, in particular, half-metallic ferromagnets (e.g. CrO_2, Sr_2FeMoO_6 and Fe_3O_4), are ideal candidates to be used as a source of electrons with a desired spin orientation. One of the challenges in the fabrication of spintronic devices is growing defect-free multilayer films with high-quality interfaces. These high-quality interfaces are crucial to prevent

scattering during extraction of polarized spins, therefore achieving a higher magnetic switching ratio. Studies of surface/interface quality, including surface defects, formation of secondary phases, grains and grain boundaries, are therefore very important. Physical vapor deposition techniques, such as pulsed laser deposition (PLD), can be used not only to fabricate multilayer films in-situ by using different feed gases and targets, but also to develop high- quality interfaces in appropriate material systems. Moreover, the formation of metastable phases in PLD is possible because the deposition takes advantage of non-equilibrium thermodynamics and processes. In addition to obtaining further insights into the physics of these fascinating half -metallic materials, the goal of my project was to understand how the surface/interface quality of these films grown on different substrates and with different growth conditions affects the physical properties of these magnetic oxides. The structure of this thesis is as follows: first an introduction about transport properties and the density of states in magnetic transition metals, the history of GMR (Giant magnetoresistance) and Tunneling magnetoresistance effect, and it will be following by an overview of half metals and transition magnetic oxides. The second chapter will have a short overview of the experimental apparatus and techniques have been used in this thesis. There will also be short description about the uncommon techniques that have been used in this project.

Two particular half-metallic materials, Sr_2FeMoO_6 and CrO_2, will be discussed in Chapter 3 and Chapter 4, respectively. Chapter 3 will start with an introduction and review of some relevant papers about Sr_2FeMoO_6 (Section 3.1) and then the major results of this thesis will be presented in three sections. First, successful growth of single-phase Sr_2FeMoO_6 on Si(100) substrates, and studies of the growth conditions including deposition temperature and deposition time (Section 3.2). In Section 3.3 and 3.4, the epitaxial growth on the different substrates was the focus of the project. In Section 3.3, the growth condition of the MgO was systematically studied and optimized growth conditions have been obtained. The depth profiles of chemical state for the near-surface regions have also been studied for the best quality film grown on MgO before and after annealing (Section 3.3). In Section 3.4, Sr_2FeMoO_6 films were epixially grown on three substrates of MgO(001), SrTiO3 (100) and $LaAlO_3$, the influence of lattice matching of these substrate on the growth evolution of the

Sr_2FeMoO_6 films will be discussed. Chapter 4 will present work on CrO_2, first with the history and background about this binary alloy followed by the major results of this project regarding the CrO_2 sample. Finally, Chapter 5 will offer the major conclusion of the present work and discussion of future work.

1.2 Background and introduction

The recipients of the 2007 Nobel Prize in Physics, Albert Fert [5] from France and Peter Gruenberg [6] from Germany, independently discovered a very large magnetoresistance effect in magnetic multilayered films. This effect is called giant magnetoresistance (Section 1.2.1) by Fert's group in their original Physical Review Letters paper [5]. The idea of magnetoresistance in ferromagnetic materials, which is the basis of read-out head memories and magnetic field sensors, came from W. Thomson [7] (Lord Kelvin) in 1856, little substantial improvement in this technology occurred in the first 150 years after Thomson's discovery.

In the late twentieth century, development of new experimental setups where one has more control on the growth procedure (e. g. molecular beam epitaxy (MBE), laser ablation, chemical vapour deposition) and characterization methods (e.g. magneto optic Kerr effect and scanning probe microscopy) has led to new advances in science, particularly in Physics and Materials Science.

The GMR effect was observed in a combination of Fe and Cr thin layers and the magnitude of the GMR effect strongly depends on the thickness of the layers. The similar crystal structure of Fe and Cr making it possible to form a super-lattice, and careful control of the epitaxial layer-by-layer film growth by MBE. Furthermore, controlling the interface thickness was very important because the thickness of the barrier must be less than the mean free path of the travelling spin orientation.

1.2.1 Resistance and magnetoresistance

Electrical resistance is the response of a metal to an applied electric current and it can be due to several scattering processes. In a crystal, the vibration of the atoms around their equilibrium positions may scatter the conduction electrons. The existence of impurities and crystal defect will also cause scattering. In normal, non-magnetic metals, thermal vibrations will decrease, with decreasing temperature and there will be less scattering of the conduction electrons and thus the resistance will decrease, as well. In ferromagnetic metals below the

Curie temperature an increase of directional ordering may result in less scattering [8]. There is also a change in the resistance due to applied magnetic field called magnetoresistance. The magnetoresistance ratio is $MR = \frac{R_H - R_0}{R_0} = \frac{\Delta R}{R_0}$, where R_H is resistance of the material in an applied magnetic field and R_0 is resistance in zero magnetic field. In ferromagnetic materials, the Fermi level crosses the d and/or s orbitals and conduction electrons can come from either or both of these orbitals. Sir Nevill Mott studied the conductivity in d orbital transition elements and noticed higher resistivity in magnetic elements. He suggested that conductivity mainly comes from the 4s electrons since they have a wider energy state. However, in magnetic elements the d orbitals are not full, and the 4s electrons can also scatter into the d states at the Fermi level resulting higher resistance [9]. A large magnetoresistance effect (~ 2%), or so called anisotropic magnetoresistance, was seen in ferromagnets. The anisotropic magnetoresistance quantifies the change of the resistance depending on the direction of the applied magnetic field with respect to the current [8]. Spin-orbit coupling, which was first explained by Kondo, has been known as the origin of anisotropic magnetoresistance [10]. A typical MR effect was a few percent, and MR was a research topic of many groups for a long time. Great progress has been made studying the effect of spin direction on the electrical transport properties [11], finally resulting in the GMR effect [5,6] with an order of magnitude higher than MR, as can be seen in Figure 1-1. In GMR devices, two ferromagnetic layers sandwich a nonmagnetic layer, and the magnitude of the coupling of the magnetic moments of the two layers (antiferromagnetic or ferromagnetic) depends on the thickness of the non-magnetic layer. For any given thickness at zero magnetic field, the two magnetic layers will couple antiferromagnetically. This coupling results in a higher resistance since up-spin electrons are scattered by regions of down spin electrons and vice versa. By applying an external magnetic field, the magnetic moments of the both layers can be made parallel and conduction electrons with the same spin will be able to move through the heterostructure with minimal scattering, and therefore the overall resistance will decrease (Figure 1-1).

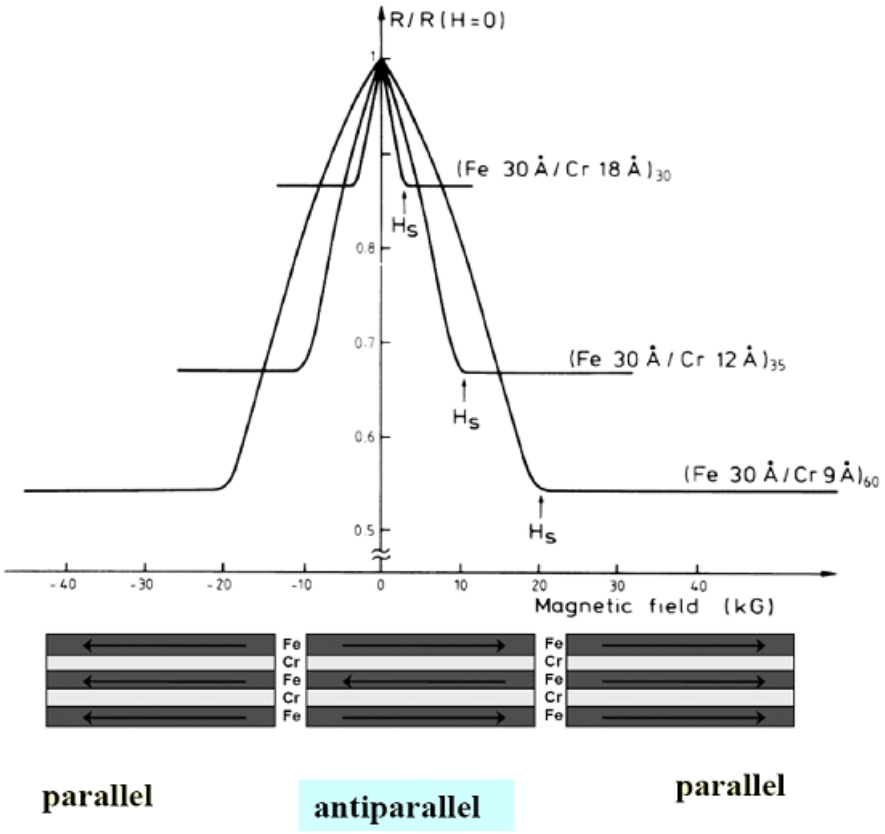

Figure 1-1: Magnetoresistance of Fe/Cr superlattices at 4.2 K. The magnetic field is applied along the [110] axis of the layers. The Figure is adapted from Ref. [5].

1.2.2 Ferromagnetic metals

The origin of magnetism in d orbital transition metals, e.g. Fe, Ni and Co, comes from the filling of the d orbitals. In 3d transition metals, the 4s and 3d orbitals are host to the valence electrons. The 3d orbitals are rather narrow in energy (4-7 eV), whereas the 4s orbitals are wide and spread out over a large range of energy (15-20 eV), so that there is an overlap between neighboring atoms. In the ground state, all the lowest energy levels are filled by electrons in accord with the Pauli Exclusion Principle (i.e. each level can have just two electrons, each with opposite spin). The highest occupied energy level is called the Fermi energy E_F. In a nonmagnetic metal (paramagnet), as shown in Figure 1-2, spin up and spin

down electrons occupy an equal number of states and there is no net magnetic moment. However, in ferromagnetic metals, even though the densities of states available between up and down electrons are nearly the same, the states are shifted in energy with respect to each other. This shift is the source of a net magnetic moment and results in an unequal filling of the energy bands [12]. This is quantified by the spin polarization factor known as $P = \frac{N_\uparrow - N_\downarrow}{N_\uparrow + N_\downarrow}$, where $N_\uparrow$ is the number of electrons with spin up and $N_\downarrow$ is number of electrons with spin down at the Fermi level.

1.2.3 Half-metals

A half-metallic material is a solid with unusual electronic structure at the Fermi level. The density of states for one of the electron channels with spin up or down has metallic behavior while there is gap in the energy band at the Fermi level in the other channel, leading to behavior as a semiconductor or insulator for one spin orientation [13,14]. One of the hallmarks of half-metallicity is that the magnetic moment is always an integer number of Bohr magnetron per unit cell. In a half-metallic antiferromagnet, the net magnetic moments of the two different sublattices cancel each other and the net magnetic moment is zero [8]. Half metals respond differently to external electric or magnetic fields. There is no high field magnetic susceptibility but there is an electric conductivity response. The hybridization of d and s orbitals plays an important role in the electronic structure of solids. Even though ferromagnets are spin polarized to a certain degree not all of them are half-metallic. For example, in ferromagnets such as Co and Ni, all the 3d spin up bands, are filled and only 3d spin down electrons exist at the Fermi level. Even though they are spin polarized [12], Co and Ni are therefore not half-metals since their Fermi level also crosses the unpolarized 4s bands. In order to have a half metal from spin polarized material it is necessary to prevent the 4s band from crossing the Fermi level. This is usually achieved by hybridization of the 4s band. All half-metals therefore contain more than one element. CrO_2[15], double perovskites such as Sr_2FeMoO_6 [16], Mn-based Heusler alloys [13] and sulfides are all examples of half-metal oxides. Of all of these, CrO_2 has the simplest binary structure [13].

Figure 1-2 shows the schematic density of states for nonmagnetic, ferromagnetic and half-metallic metals. On the left of Figure 1-2 is a schematic of the density of states for a non-magnetic metal, the numbers of states are equal and the polarization factor is zero. The middle figure shows the density of states for a ferromagnetic material, the density of spin up electrons are more than spin down electrons and P>0. The figure on the right is a schematic diagram for the density of states of a half metallic material, where electrons with spin up behave as a metal whereas and semiconducting gap can be seen for spin down electrons.

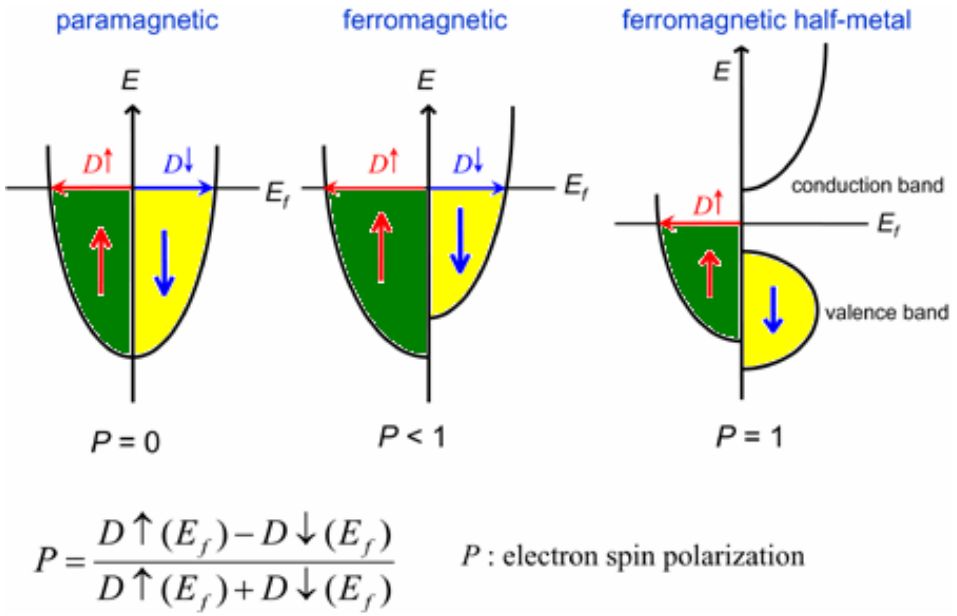

Figure 1-2: The left figure is a schematic diagram of density of states for a non-magnetic metal. The number of states is equal and polarization factor is zero. The middle figure shows the density of states for a ferromagnetic material. The density of spin up electrons is more than spin down and P>0. The right figure is schematic diagram of a half metallic material. Electrons with spin up direction behave as a metal whereas a semiconducting gap can be seen for spin down electrons.

One of the fundamental devices operating based on the GMR effect is the spin valve. Figure 1-3 shows a schematic picture of a spin valve. There is a thin barrier layer, in this case a non-magnetic metallic layer (shown in yellow, light shaded area), sandwiched between two layers of ferromagnets. The resistance of the device depends on the direction of magnetic moments of the ferromagnetic layers. When the magnetic moments of both ferromagnetic layers are parallel, there is less spin scattering and therefore the total resistance is lower, whereas for antiparallel magnetic moments the total resistance is higher. In the actual spin valve devices, one of the ferromagnetic layers is the so-called soft layer and its magnetic moment is easy to reverse, while the other hard layer is difficult to reverse. The soft layer is sensitive to the change of the magnetic field and it can be used to control the valve [12].

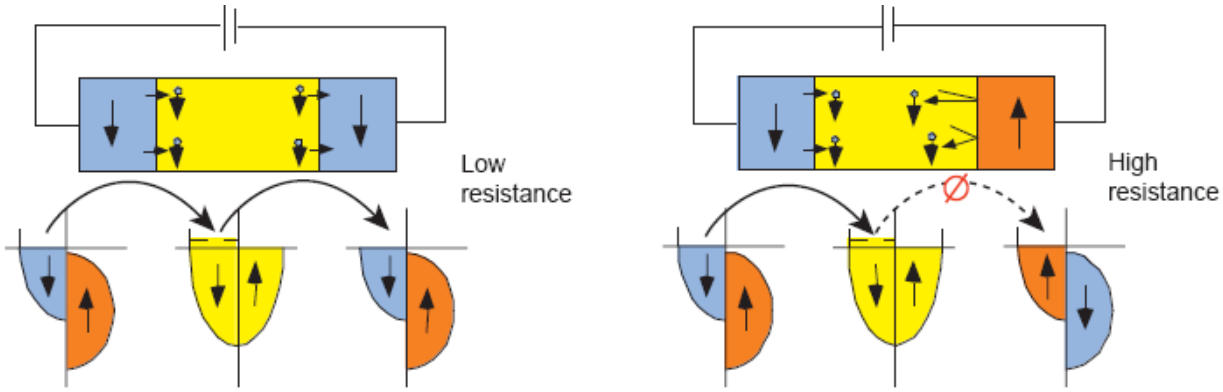

Figure 1-3: Schematic of the spin valve. This diagram shows the magnetic configuration in a multilayer junction-. The metal layer sandwiched between two ferromagnetic layers in parallel states with lower resistance (left) and in antiparallel states with high resistance (right). The picture is adapted from Ref. [12].

Magnetic tunnel junction [17] is another type of spin valve where the ferromagnetic layers are altered by insulating layers as shown in Figure 1-4. The thickness of the insulating layer should be only a few atomic layers thick so that the electrons can tunnel through the barrier without losing their spin information. This can lead to tunneling magnetoresistance, which is not a new effect and in fact it has first been observed in 1975 by Jullliere [18]. Julliere's experiment was done at low temperature and the tunneling MR effect was 14%. He

proposed that the spin is conserved during the tunneling and the tunneling current is proportional to the available density of states. Since then, considerable progress had been made after reports of the GMR effect. In 1995, Moodera et al. [19,20] were able to observe the tunneling MR effect at room temperature.

As discussed in Section 1.1, one of the main challenges regarding fabrication of spin-based devices particularly tunneling-based device is the quality of the interface. It has been shown that the role of the ferromagnet-insulator interface and the nature of their bonding not only are crucial to controlling the magnitude of the spin polarization factor but also will change the sign of polarization [21]. The goal of this thesis was to seek better understanding of the effect of growth parameters on the physical properties of the half-metallic magnetic oxides (Sr_2FeMoO_6, CrO_2) and on the interface quality.

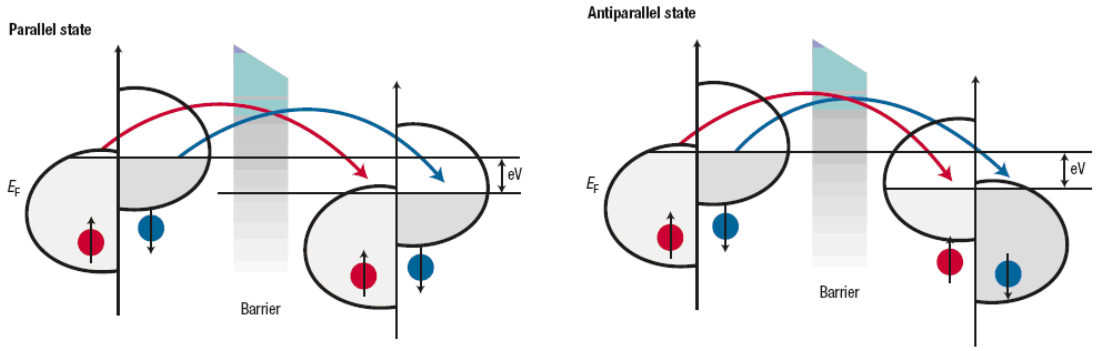

Figure 1-4: The schematic diagram of the band diagram in a magnetic tunnel junction (MTJ). Two ferromagnet layers are separated by the insulating barrier. Since the direction of the spin is conserved during the tunneling process, it is easier for the spin to tunnel in the parallel state (left figure) rather than antiparallel (right figure). This Figure have been modified from Ref. [17].

Chapter 2
Experimental Techniques

2.1 Pulsed laser deposition system

Pulsed laser deposition (PLD) [22] is a powerful yet very simple technique with a wide range of applications. The system consists of a high power laser as an external source to vaporize the material for deposition, a set of optical components to focus and raster the laser beam on the target surface and a vacuum chamber to grow the film material. The laser beam is often intense enough to vaporize the hardest and most heat resistant materials. The high laser energy and short pulse duration produce high heating rates (10^8 K/s) on the target surface, and therefore materials are dissociated from the target surface and ablated on the substrate surface with nearly the same stoichiometry as the target. Maintaining the target stoichiometry is one of the important features of PLD and it enables one to fabricate complex oxides films. In contrast to the simple system set-up, the nature of the deposition process is a complex phenomenon. The process involves the interaction of the laser radiation with the target surface, the dynamics of the ablated materials, and the nucleation and growth of the ablated material on the substrate surface. Each step in this process is important in determining the epitaxial growth quality of the thin films (stoichiometry, defects, and surface roughness).

The set-up used in this work was a NanoPLD system (PVD Products) as shown in Figure 2-1 with a base pressure better than 5×10^{-7} Torr achieved by a turbomolecular pump. The system is equipped with a 248-nm excimer laser (Lambda Physik COMpex 205) with a maximum laser fluence of 600mJ/pulse and a maximum repetition rate of 50 Hz, which is used to ablate the targets. A set of optics focus, raster and direct the laser beam inside the chamber. The black box underneath the optical set-up shown in Figure 2-1 is the control electronics of the system. It is equipped with a gas flow meter for 2 different feed gases, a current source for the substrate heaters, and a monitor to read the substrate temperature.

Figure 2-2 shows inside the chamber, where six rotating target holders for in-situ multilayer deposition can be seen. In order to keep the targets cold, the targets were covered by a water-cooled cold plate. The maximum growth temperature was 900°C and it was produced by infrared lamps irradiating the back side of the substrate. The temperature was monitored by an optical pyrometer and a thermocouple connected to the back of the substrate holder. One of the main problems in thin film growth by PLD is particulate deposition on the films. Since the size of these particulates is sometimes on the order of microns, it can affect the quality of the films. In order to minimize particulate growth, the target surface was sanded down using 2400 grit sandpaper and ethanol before each deposition. During deposition, rastering the laser beam on the target surface, rotating the target, and vertical positioning of the substrate with respect to the target surface normal also proved to be helpful.

The whole process was controlled by commercial software written in Labview but modified here at WATLab. Two different 1-inch diameter targets of Sr_2FeMoO_6 (99.95% purity, MTI Corp.) and metallic Cr (99.95% purity, ACI Alloys) were obtained commercially. Oxygen and/or Ar were introduced into the chamber by a variable leak valve to a typical growth pressure of 0-400 mTorr. The substrates (5×5 mm^2 and/or 5×10 mm^2 and/or 10×10 mm^2 all 0.5 mm thick) used in the present work were cut from wafers of MgO(001), $SrTiO_3$(100), and $LaAlO_3$(100) substrates (MTI), and from wafers of Al_2O_3(0001) or Si(100) (University Wafers, all with 99.99% purity). The target-to-substrate distance can be varied between 36-58 mm and thin films were deposited for a preselected period of time (5-60 min).

Figure 2-1: Photograph of Pulsed laser deposition system (PVD product) at WATLab.

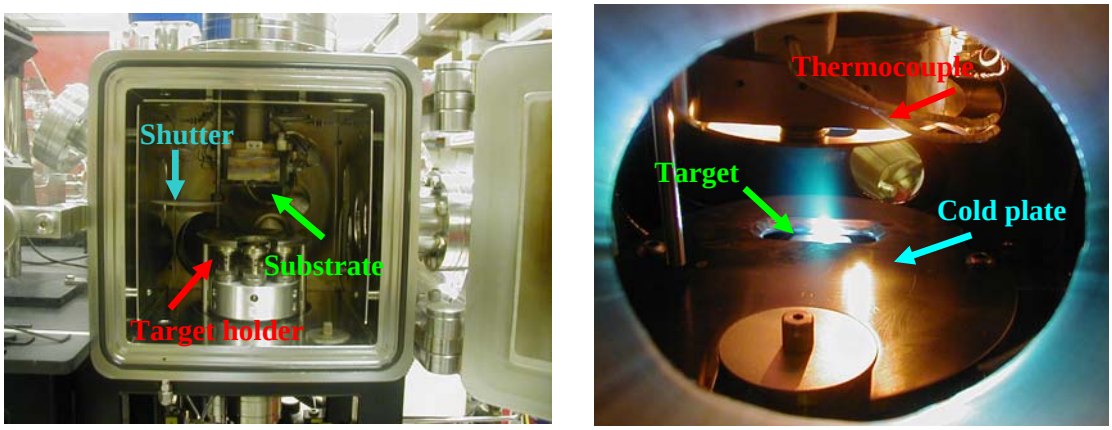

Figure 2-2: Photographs of the PLD system, depicting the growth chamber, shutter, cold plate, target holders and substrate holder inside.

2.2 Morphology analysis of the surface

The surface morphology of the samples was studied by Atomic Force Microscopy

(AFM, DI Nanoscope IV) operated in tapping mode and contact mode. AFM [23,24,25] measures the atomic forces (~10^{-9} N) between the probe (cantilever tip) and the sample. The motion of the laser light on the cantilever is monitored by the system and a feedback loop is used to maintain a constant tip-sample force (contact mode) or constant tip oscillation (tapping mode) during scanning.

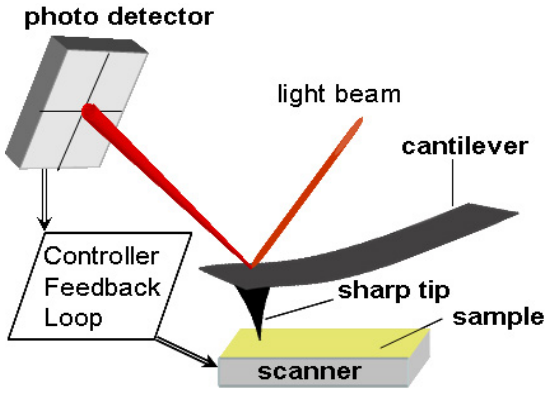

Figure 2-3: A typical AFM set-up. The figure has been adapted from Ref. [25].

The resolution of the AFM is limited by the sharpness of the tip. For a contact tip (SiN), the diameter of the tip is 30-50 nm while a tapping tip (Si) gives a higher resolution with a tip diameter of ~10 nm. In tapping mode, the tip is oscillating at its resonance frequency (~ 300 kHz) across the sample surface with constant oscillation amplitude. In contrast to contact mode, there is less chance to damage the sample due to lateral forces in tapping mode. However, tapping tips are more expensive and scan speeds are slightly lower than in contact mode. Since AFM operates based on tip-surface forces, it can be easily used for insulating samples with nanometer resolution. AFM can also provide information about the height of the particles, the grain sizes and the roughness of the sample. In tapping mode, two images can be obtained, one contains the topographical information about the sample, and the other one called the phase image. Phase imaging is the mapping of the phase lag between the original signal that has been sent to drive the cantilever and the signal that comes back from the cantilever. Changes in this phase lag often indicate changes in the properties of the sample surface, including variation in composition, adhesion, friction, viscoelasticity, electric and magnetic response.

In this thesis, magnetic force microscopy (MFM) [23] was used to map the local magnetic moments in some samples. MFM needs a special probe (tip), which is mostly a tapping tip sputtered with ferromagnetic material such as Co-Cr. The operation procedure is similar to tapping mode except for an additional step of lift mode, which is needed due to the long range nature of the magnetic field. In step 1, the cantilever oscillates near the resonance frequency (~ 70 kHz) and it senses changes of the force on the surface and gives topographical information. In step 2, the tip is lifted up about 10-100 nm from the surface, and the sensor can feel the interaction between the magnetic moments of the tip and the magnetic domains of the film. MFM measurement has been performed for most of the samples in the present work. However, due to artifacts such as a rough surface or the formation of secondary/stable phases on the surface, only a few samples showed a magnetic contrast.

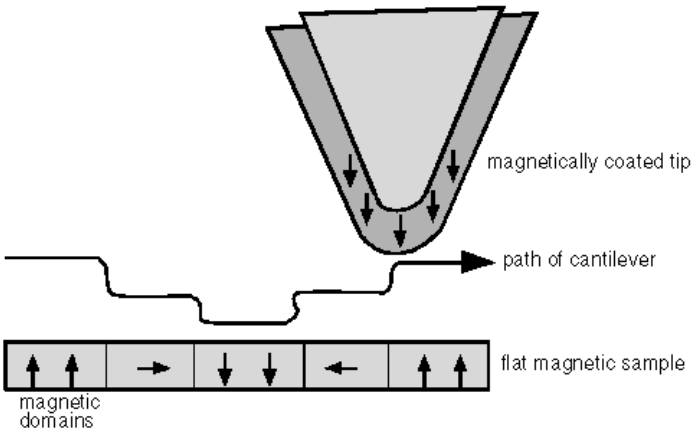

Figure 2-4: MFM tip coated with a magnetic film, interacting with the domain structure of the magnetic thin film. This picture has been adapted from Ref. [23].

For conductive samples, the morphology of the resulting films were also characterized by field-emission scanning electron microscopy (FE-SEM, LEO 1530) and Energy dispersive X-ray spectroscopy (EDAX) [26].

2.3 Structural characterization of crystals

The crystalline structure of the epitaxial films was analyzed by using a high-resolution X-ray diffractometer (XRD, PANalytical X'Pert Pro MRD), equipped with a two-bounce hybrid monochromator and a Cu K_α source. In order to determine the crystalline quality of the sample, rocking curves were performed by fixing the incident beam at the desired 2θ position and rocking the detector around the ω (or θ) angle (Figure 2-5). Any kind of defect or imperfection would broaden the peak width. For the nanocrystalline samples, glancing-incidence X-ray diffraction (GIXRD) measurements was performed. The GIXRD set-up is equipped with a X-ray mirror as the incident beam optics and a parallel plate collimator as the diffracted beam optics. Figure 2-7 illustrates the glancing incidence and X-ray reflectivity set-up.

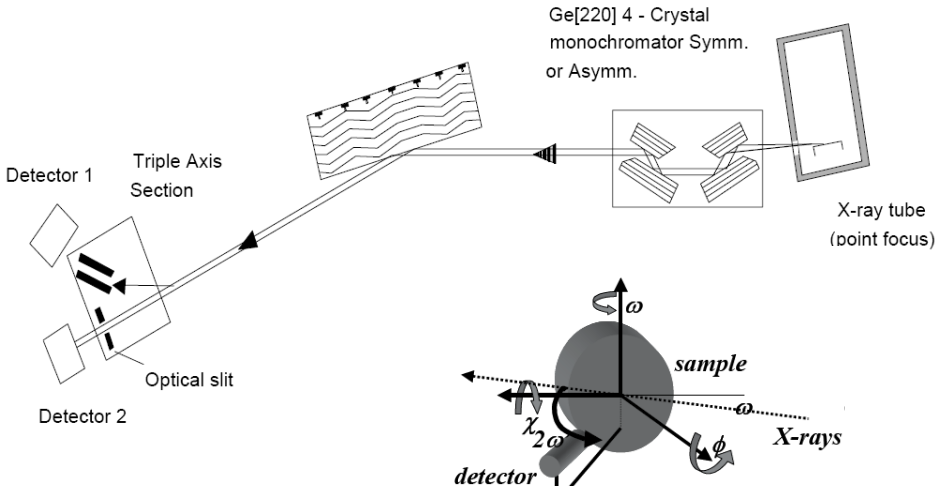

Figure 2-5: Schematic diagram of high resolution and reciprocal space map set-up and possible scanning orientation. This Figure is adapted from Ref. [29].

GIXRD is a surface sensitive technique useful for studying the crystal structure of surfaces and thin films [27,28]. The geometry of this diffraction process preferentially probes the surface and near-surface region of a film, allowing detection of a much smaller amount of material than is possible with a conventional powder scan. In GIXRD, the incident X-ray beam is fixed at a small angle of α_i near α_C, where α_C is the critical angle for total reflection. When the X-ray beam strikes the surface at a small incident angle, part of

the beam is reflected (Figure 2-6). If $\alpha_i < \alpha_C$, part of the incident beam becomes evanescent, propagating parallel to the surface with a penetration depth of a few nanometers (Figure 2-6). On increasing α_i, part of the beam becomes refracted and the penetration depth increases to a few hundred nanometer. This portion of the X-ray (both evanescent and refracted) can be diffracted by the sample and can be measured by scanning 2θ. The process is shown by the schematic diagram in Figure 2-6.

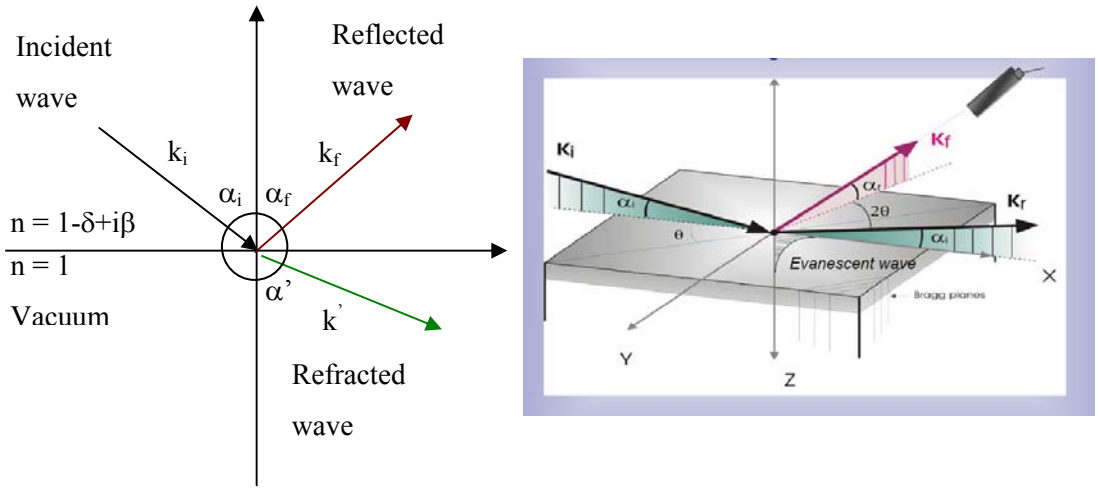

Figure 2-6: The figure on the right side is a schematic diagram of the glancing incidence process and evanescent scattering. k_i is the incident beam and k_r and k_f are the diffracted beams. This Figure is adapted from Ref. [28]. The left figure is a schematic diagram of the Incident, Refracted and reflected beam at the interface, where n is the index of refraction, δ is the dispersion term and β is the absorption constant.

To measure the thickness of an epitaxially grown film, X-Ray Reflectivity (XRR) was performed using a divergence slit of 1/16°, an X-ray mirror to produce a parallel beam geometry and an automatic beam attenuator for the incident beam, and a parallel plate collimator for the reflected beam as is shown in Figure 2-7. XRR is similar to diffraction, but the incident beam is reflected from the interfaces with different density, composition and refraction indices. Samples can be either crystalline and/or amorphous and/or multilayered. The thickness of the measured layers can range from the nanometer to micrometer scale [29].

In reflectivity experiments, the X-ray reflection of a sample is measured around the critical angle. Above this angle the penetration depth increases rapidly. At every interface where the electron density changes, a part of the X-ray beam is reflected. The XRR pattern is the interference of these reflected beams from different interfaces and it contains information about film thickness, density and roughness of the films and the interfaces. The thickness of the film (t) is related to the separation between interference fringes ($\delta\omega$) with the following formula: $t=\lambda/(2\delta\omega)$ where λ is the wavelength of the X-rays. Despite of well-established physics behind the XRR process, obtaining good data can be difficult, because getting a good XRR interference pattern depends strongly on the surface/interface roughness, and having highly parallel layers.

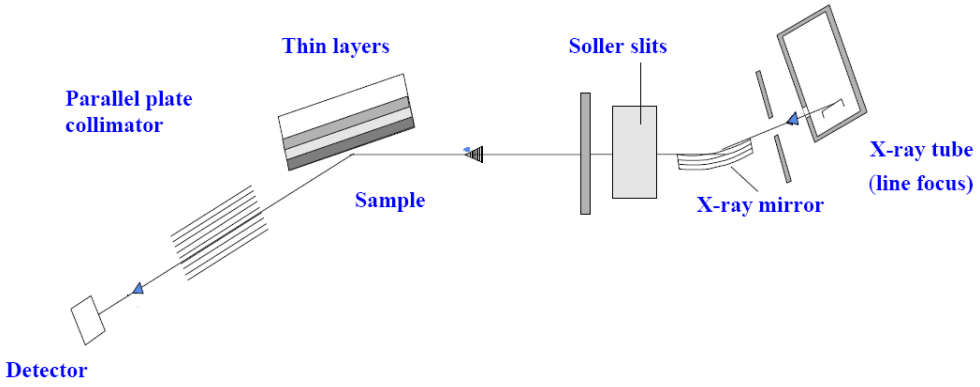

Figure 2-7: Schematic diagram of glancing incidence and X-ray reflectivity instrumental setup. The XRR scan is an ω-2θ scan. This diagram has been adapted from Ref. [29].

To study strain relaxation, crystalline quality and lattice distortion, Reciprocal Space Mapping (RSM) has been conducted using a Panalytical X-Pert-Pro MRD X-ray diffractometer (XRD), with the Cu K_α source operated at 45 kV tension and 40 mA current. A Ge(220) 2-bounce hybrid monochromator with a 1/2° slit and a channel-cut Ge(220) analyzer in the triple-axis section for the diffracted beam optics. In RSM, the lattice misfit and degree of relaxation is independent of the ω and 2θ scanning ratio and the miscut of the diffraction lattice planes with respect to the surface. A triple-axis diffractometer can provide high enough resolution to resolve close-lying features in a RSM [30]. As shown in Figure 2-8, the diffraction pattern in reciprocal

space for single-crystal samples consists of a family of planes (e. g. 224, $\bar{2}24$, $2\bar{2}4$, $\bar{2}\,\bar{2}4$) with different directions but same length of $d^* = \frac{1}{d_{hkl}}$, where d^* and d_{hkl} are d-spacing in reciprocal space and real space, respectively [31]. The RSM consists of a series ω-2θ scans around a particular plane, as shown in Figure 2-9. The broadening seen in the RSM carries information about the crystalline quality, and if the broadening is in the ω-2θ direction, it indicates microstrains and crystallite size, while broadening in ω is due to misorientation and mosaic properties of the film.

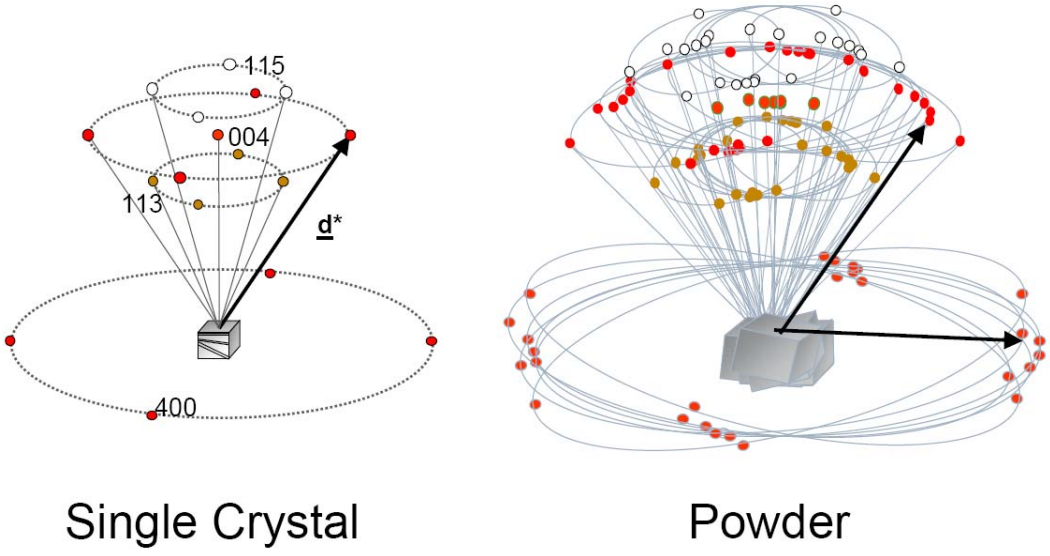

Figure 2-8: Reciprocal lattice of powder vs. single crystal configuration. This Figure has been adapted from Ref. [29].

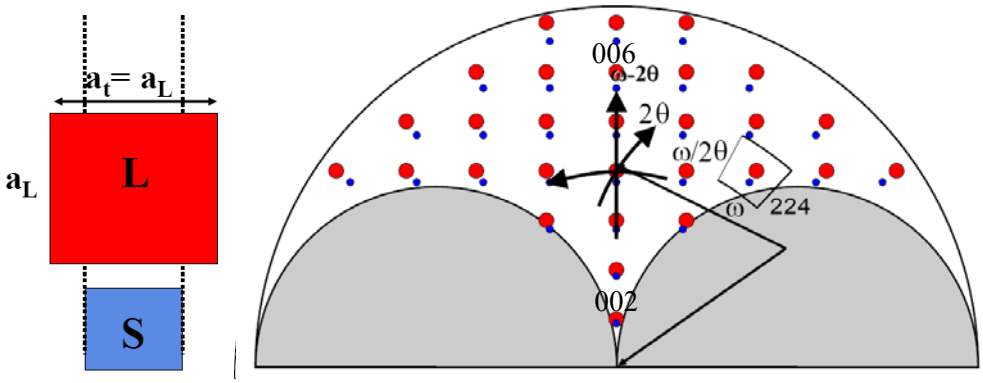

Figure 2-9: An epitaxially grown film (large circles) on the single crystal substrate (small circles) shown on the left figure. Reciprocal space map of this epitaxially grown film shown on the right figure. Direction of ω-2θ, ω and 2θ scans are indicated on the right figure. The grey area shows the diffraction forbidden regions for ω≤0 and 2θ≤ω. This Figure has been adapted from Ref. [29].

The reciprocal space map is usually presented in terms of Q_x and Q_y. The relation between the scan parameters ω and 2θ and the reciprocal space vectors Q_x is given by the following formula:

$$Q_x = K[\cos\omega - \cos(2\theta - \omega)]$$
$$Q_y = K[\sin\omega + \sin(2\theta - \omega)]$$

where $K=2\pi/\lambda$ and is the magnitude of the X-ray wave vector, ω is the angle between primary X-ray beam and the sample surface, and the 2θ is the angle between incident and diffracted X-ray beam [27]. The commercial software from Panalytical called Expert Epitaxy was used to analyze the data.

2.4 Chemical state and electronic structure analysis

The chemical-state composition of the film was studied by using a X-ray photoelectron spectrometer. X-ray Photoelectron Spectroscopy[32] (XPS), also known as Electron Spectroscopy for Chemical Analysis (ESCA), is a technique widely used to identify the chemical composition of the surface and near surface regions. It is a surface-sensitive technique (~ 2 nm depth) and the process is based on photoelectric effect. The energy of the ejected electrons is given by the Einstein equation: $BE=hv-KE-\Phi$, where KE is the kinetic energy of the photoelectron, hv is the photon energy of the X-ray, BE is the binding energy of the photoelectron and Φ is the work function of the spectrometer. XPS spectral lines show from which shell the electrons are ejected and each element has its own characteristics core-shell spectral lines. The system used in this work was a Thermo-VG Scientific ESCALab 250 Microprobe, equipped with a monochromatic Al K_α X-ray source (1486.6 eV) operated at a typical energy resolution of 0.4-0.5 eV full-width-at-half-maximum. For the non-conductive samples, a sample holder with a metallic clip was used to mount the sample, and an electron flood gun was used in order to compensate for the lack of electrons on the surface. In order to obtain depth information, the samples were sputtered down by Ar ions in specified steps. The collected XPS data were fitted, where appropriate, with a combination of Gaussian-Lorentzian lineshapes, after correction with the Shirley background by using the CasaXPS software.

2.5 Bulk magnetic and transport properties

The total magnetic moment of the selected samples was measured using a superconducting quantum interference device (SQUID) magnetometer manufactured by Quantum Design[33]. The Quantum Design magnetometers at Brock University and at McMaster University were used in this work. A SQUID is used to measure the magnetic moments as a function of temperature or applied magnetic field up to 5.5-7 T. The sensitivity of the system is 2×10^{-6} emu. In order to obtain the magnetization (M(H)) curve for the ferromagnetic layers, the linear diamagnetic or paramagnetic contribution of the substrates at higher applied magnetic field were subtracted from the total magnetic moment.

The magnetoresistance measurements were also performed at Brock University for selected samples using 4- probe method. To measure the resistance of the samples, the sample was mounted on a home-made probe and inserted inside SQUID magnetometer. The magnetic field up to 5.5 T was applied by the SQUID magnet. The current of 10 mA was supplied by a current source and the voltage drop across the samples was measured to calculate the resistance. In order to eliminate the thermal voltage, each data point was calculated from the difference between the voltage as a direct and reversed polarity of the current source.

Chapter 3

Pulsed laser ablation of double perovskite Sr_2FeMoO_6

3.1 Introduction

The double perovskite Sr_2FeMoO_6 has long been known as a conducting ferromagnet (or ferrimagnet) with a relatively high Curie temperature (T_C) of 410-450 K[34]. In 1998, a report by Kobayashi et al.[16] showed that Sr_2FeMoO_6 has a low-field magnetoresistance (LFMR) response at room temperature, drawing attention to the spin and electronic properties of this type of double perovskite as a potential material for spintronics applications. Their electronic structure calculations further showed that ordered Sr_2FeMoO_6 is half-metallic (Figure 3-1), and it exhibits tunneling-type magnetoresistance (MR) at room temperature. According to the Web of Science, Kobayashi's paper has been cited more than 753 times. In 2007, Serrate et al. [35] published a review paper entitled: "Double perovskites with ferromagnetism above room temperature". In this review paper, they compared much of the theoretical and experimental results published about transition metal based double perovskites. In order to compare physical properties of these double perovskites, there has been a large amount of work on the double perovskites $A_2B_xB'_{(1-x)}O_6$, where A is divalent or trivalent and B and B' are different transition metals [36,37,38,39,40,41,42,43,44,45,46,47,48,49]. In general, the saturation magnetic moments and T_C of almost all doped double perovskites are lower than that of Sr_2FeMoO_6. The crystal structure of Sr_2FeMoO_6 is tetragonal [34] and it consists of Fe and Mo ions where each FeO_6 linked to six MoO_6 and vice versa (Figure 3-1). The large distance between the Fe sites has provoked intriguing questions about the nature of the mechanism controlling the magnetic and electronic properties that result in the half metallic ground state. The arrangement of magnetic moments consists of the Fe^{3+}, $3d^5$, $\mu_{Fe}=5\ \mu_B$ per formula unit (/f.u.), magnetic

moments antiferromagnetically coupled to the Mo^{5+}, $4d^1$, μ_{Mo}=1 μ_B/f.u. moments to give a total saturation magnetic moment of 4 μ_B/f.u. at low temperature [16]. However, some experimental results indicate that a Fe^{2+} ($3d^6$, μ_{Fe}=4 μ_B/f.u.) and Mo^{6+} ($4d^0$, μ_{Mo}=0 μ_B/f.u.) configuration is responsible for the magnetic moment of 4 μ_B/f.u.[50,51], while others propose a combination of these two pictures [52]. The strong antiferromagnetic coupling between the localized electron of Fe^{3+} and the delocalized electron of Mo^{5+} gives rise to a high Tc and it has been explained by a superexchange or a standard double exchange [16,53] mechanism.

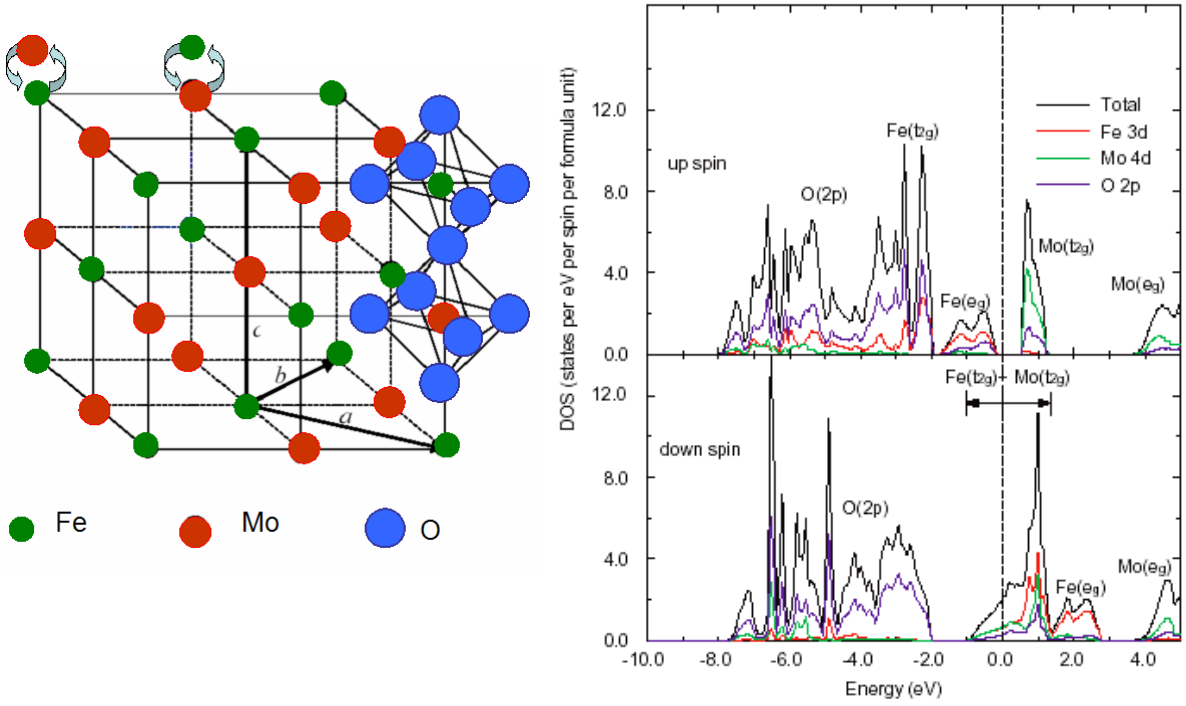

Figure 3-1: The left figure is the crystal structure of Sr_2FeMoO_6. The structure is color-coded by atomic species. Green circles (small circles) represent Fe atoms, red (midium sized circles) are Mo and O atoms are represented by blue circles (large circles). The possibility of misplacing the Fe and Mo atoms is shown by the arrows. The crystal has a tetragonal lattice structure with a=b=5.5870 Å and c=7.9180 Å and the space group of $p_{4/2m}$. The a, b and c axes are indicated by the arrows in bold. The figure on the right shows the density of states of Sr_2FeMoO_6, as calculated by Kobayashi [16]. The Fermi level crosses the spin-down bands but not the spin-up bands, suggesting the half metallic nature of this material. This Figure has been modified from Ref. [16].

Experimentally, it has been difficult to prepare Sr_2FeMoO_6 samples with this high magnetic moment of 4 μ_B/f.u. [54,55,56,57,58,59]. One possible explanation for this difficulty is the presence of antisite defects. When the Fe^{3+} cation is misplaced with the Mo^{5+} cation, an antisite (AS) defect is formed, changing the transport and magnetic properties of the resulting material. Balcells et al. [54] studied batches of bulk polycrystalline samples annealed at different temperatures. Using X-ray diffraction patterns, they found that the antisite defect density can be determined by the ratio of the (112) and (002) peak intensities to the (101) peak intensity of Sr_2FeMoO_6. Their result shows that samples grown at higher temperatures have less antisite defects and higher magnetic moments (Figure 3-2). Garcia-Hernandez et al. [60] reported that disorder at the Fe and Mo sites is responsible for the linear dependence of the saturation magnetization on the LFMR. By annealing the Sr_2FeMoO_6 samples in H_2/Ar at different temperatures, Navarro et al. [61] produced samples with different concentrations of antisite defects. They suggested that antisite defects could promote magnetic frustration and lower the magnetic moments, and could also be responsible for the high-field MR. Saha-Dasgupta et al. [62] used ab-initio band structure calculations to show that the presence of antisite defects destroys the half-metallic nature of Sr_2FeMoO_6 and reduces the magnetic moments at the Fe sites. Stoeffler et al. [63] also used ab-initio calculations and they showed that while an antisite defect density of 15% can lower the magnetic moment by 1 μ_B/f.u., where oxygen vacancy of 8.5 % lower the magnetic moment by 2 μ_B/f.u. Furthermore, Monte Carlo calculations by Ogale et al. [64] demonstrated that both the saturation magnetic moment and T_C of Sr_2FeMoO_6 strongly depend on the antisite defect density, and that the oxygen content could play an important role in the magnitude of the magnetic moment, especially in samples with more disorder.

The other common types of defects that could account for LFMR in Sr_2FeMoO_6 are the presence of secondary phases and antiphase grain boundaries [16,53,57,65,66,67,68,69]. Sarma et al. [68] measured high-field and low-field MR for ordered and disordered Sr_2FeMoO_6 samples, and showed that the disordered sample was not half metallic and only the ordered sample exhibited a sharp LFMR peak. They concluded that the observed LFMR is dominated by intergrain spin-dependent scattering of highly polarized charge carriers in

this half metal. For Sr_2FeMoO_6 grown on $SrTiO_3$(100) bicrystals, Yin et al. [57] also attributed the LFMR to spin-dependent scattering across grain boundaries and not to an intra-granular effect. In contrast, Huang et al. [56] compared the transport and magnetic properties of a series of Sr_2FeMoO_6 samples with different grain sizes and disorder and also with homo-composite samples (consisting of mixtures of perfectly ordered Sr_2FeMoO_6 as the main component and less-ordered Sr_2FeMoO_6 as the second or third component). Those samples with larger grain size and lower disorder were found to have higher saturation magnetic moments and MR. The homo-composite samples with a large amount of grain boundaries also showed high LFMR. They therefore concluded that both inter- and intra-granular effects are responsible for LFMR (Figure 3-3). Niebieskikwiat et al. [65] showed that for polycrystalline $Sr_2FeMoO_{6+\delta}$ samples, the magnetization and lattice parameters were the same but the MR was enhanced for δ=0.04. This latter result led them to propose that extra oxygen near the surface of the grain boundary is responsible for the enhancement. Zhong et al. [69] used a wet-chemistry method to produce Sr_2FeMoO_6 bulrush-like nanostructures. They showed that the MR can be improved by controlling the grain size and the concentration of $SrMoO_4$ at the grain boundary. The presence of the $SrMoO_4$ at the grain boundary was also suggested by MacManus-Driscoll et al. [67].

Due to the sensitivity of the magnetic and transport properties to crystal defects such as the aforementioned antisite defects and grain boundaries, the methodologies and conditions of sample preparation are very important for controlling the physical properties of the Sr_2FeMoO_6 films. While solid-state synthesis is one of the most common methods for growing polycrystalline Sr_2FeMoO_6 [65,66], magnetron sputtering [70] and wet-chemical methods [56,71] can also be used to produce single-crystal film and bulk polycrystalline samples, respectively. However, the deposition temperatures in almost all of the reported cases were higher than 800°C. Furthermore, many of the reported samples have been post-annealed at even higher temperatures. Manako et al. [59] studied effect of the oxygen pressure and growth temperature on growth by pulsed laser deposition (PLD), in order to get epitaxial Sr_2FeMoO_6 on $SrTiO_3$(100) and $SrTiO_3$(111). The phase diagram reported by them shows that only a narrow range of oxygen pressures (10^{-5}-10^{-6} Torr) and temperatures higher

than 900 °C (which is not easy to access by PLD) lead to a single-phase, good quality samples (Figure 3-4). In contrast, Santiso et al. [72] also studied the effect of growth conditions on the formation of secondary phases of Sr_2FeMoO_6 on $SrTiO_3$ substrates. Their results show that for Sr_2FeMoO_6 films grown at 950 °C in ultra high vacuum (pressure less than 10^{-8} mbar), metallic iron precipitates can form, whereas in a flow of oxygen (pressure of 10^{-6} mbar), iron oxides can be obtained. Their in-situ XPS analyses suggest the presence of secondary phases including $SrMoO_4$ and $SrFeO_3$ on their samples grown at lower pressures (above 10^{-4} mbar).

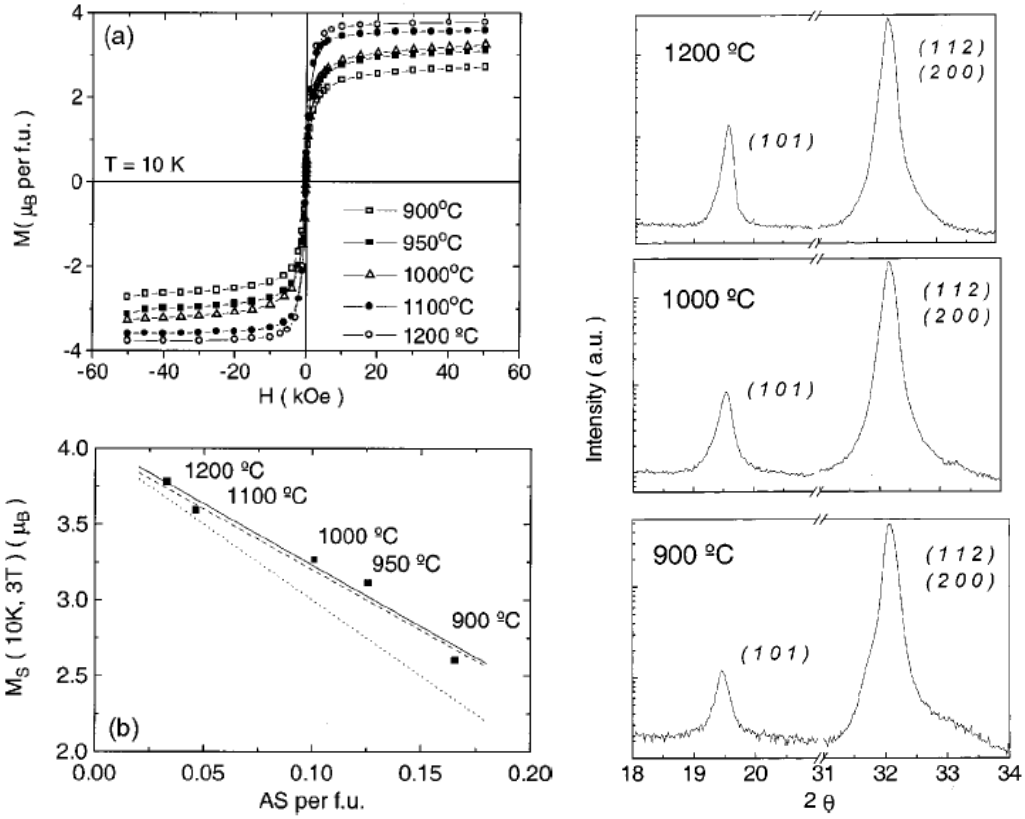

Figure 3-2: (a) Magnetization curve as a function of applied magnetic field for polycrystalline Sr_2FeMoO_6 samples grown at different temperatures. (b) Dependence of saturation magnetic moment to the antisite defect density (left). Analyzing the antisite defect by comparing the I(112)+I(200))/I(101). Growing at higher temperatures leads to a larger diffracted signal from the (101) planes, and thus a lower antisite defect density (right figures). Graphs have been adapted from Ref. [54].

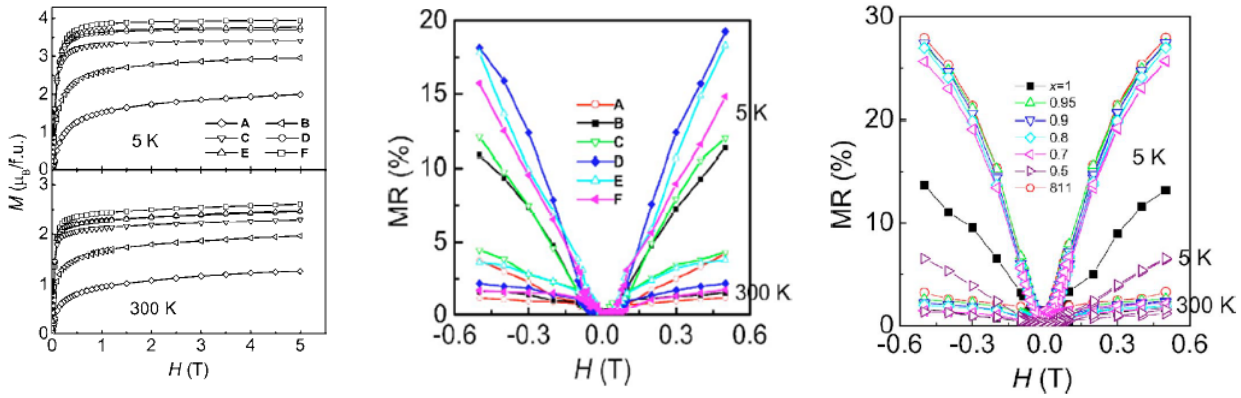

Figure 3-3: Figure on the left shows magnetization curve as a function of applied magnetic field for polycrystalline Sr_2FeMoO_6 sintered in the temperature range of 900-1150ºC (sample A-F), where F sample had the longest annealing time. Figure on the middle shows low-field MR for the same (A-F) samples. (c) Figure on the right shows the low-field MR for homocomposite samples. x is the weight ratio of the highly ordered samples to the disordered samples . Graphs have been adapted from Ref. [56].

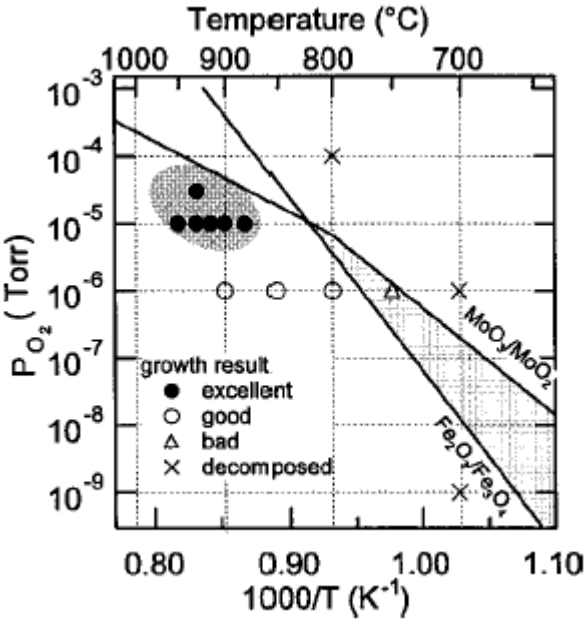

Figure 3-4: Diagram of crystal quality dependence of oxygen pressure and growth temperature. Good quality single phase Sr_2FeMoO_6 films are shown by closed circles, single phase with antisite disorder shown by open circles. Triangles show a mixed phase of the samples, while x shows nothing was detected by XRD. The grayed area shows the optimum growth conditions. This Figure has been adapted from Ref. [59].

Another important factor that can affect the crystal quality of the Sr_2FeMoO_6 films is the choice of substrate. In magnetic oxide films (e.g., $La_xSr_{(1-x)}MnO_3$), it is possible to control the formation of domains and secondary phases by manipulating the lattice parameters with different growth conditions (temperature, deposition time), hydrostatic pressure, or use of substrates with a different crystal lattice mismatches to the films [73,74,75,76,77]. The most popular substrate for growing Sr_2FeMoO_6 films is $SrTiO_3(100)$ due to the close lattice matching between the two materials [57,58,59,78]. However, the possible presence of oxygen vacancies [79] and low-level magnetic impurities in the $SrTiO_3$ substrate could lead to unusual electrical behaviour, potentially causing difficulties in interpreting the data. Other substrates including MgO(001) and $LaAlO_3(100)$ [57,70,80] have also been used to obtain epitaxial films of Sr_2FeMoO_6. Yin et al. [57] found their magnetic and transport properties to be independent of the substrates. However, Asano et al. [70] and Borges et al. [80] showed that the magnetic and transport properties of epitaxial Sr_2FeMoO_6 films on $SrTiO_3$ and MgO are different, with smaller magnetic moments found on MgO (1.0 μ_B/f.u. at 300 K [70] and 2.3 μ_B/f.u. at 20 K [80]) than on $SrTiO_3$ (1.3 μ_B/f.u. at 300 K [70] and 3.5 μ_B/f.u. at 20 K [80]).

Despite the huge amount of work that has been done on Sr_2FeMoO_6, the results are still controversial and many problems remain unanswered. In particular, as it was discussed earlier, one of the most important considerations for fabrication of the multilayered spintronic devices is the surface/interface quality of the films. The growth parameters including various substrates with different lattice mismatch can affect the growth evolution and therefore the quality of the surface. Another obstacle that can slow down the process of using these materials as a source of spin injector is the high growth temperature and complicated growth process required, which has been partially address by earlier work [59]. For applications in the microelectronic industry, a lower deposition temperature is generally preferred. In the present work, it will be shown by optimizing the other growth parameters it is possible to obtain good quality films at considerably lower deposition temperatures.

In this chapter, three different subjects in the general area of Sr_2FeMoO_6 growth evolution and surface/interface properties will be discussed. In Section 3.2, it will be shown that by optimizing the growth condition, single-phase, polycrystalline Sr_2FeMoO_6 can be grown directly on Si(100) at a temperature as low as 600°C. This is the first time that successful growth of Sr_2FeMoO_6 on Si has been achieved by using the PLD method. In this section, it will also be shown that despite the lack of lattice matching, partially oriented growth of nanocrystals in the Sr_2FeMoO_6 film can be obtained on Si(100). The present results open up the prospect of integrating these oriented, nanocrystalline Sr_2FeMoO_6 films into Si device fabrication.

In Section 3.3 will be demonstrated that the Sr_2FeMoO_6 films can be deposited by PLD on MgO(001) from 400°C to 800°C, and epitaxially grown films can be obtained at a temperature as low as 600°C. MgO is chosen as the substrate because MgO has a reasonably good lattice match to Sr_2FeMoO_6 (6.2%). MgO is non-magnetic and therefore will not introduce any magnetic signature, and it can be used as an inert support for constructing spin-based devices. The saturation magnetic moment is found to be almost the same (3.4 μ_B/f.u.) for Sr_2FeMoO_6 samples grown at 600°C and 800°C, with the coercivity field of the former higher than the latter. The high quality of the Sr_2FeMoO_6 films grown at 800°C is indicated not only by the low coercivity field and high saturation magnetic moment, but also by the narrow width (0.3°) of the rocking curve of the (004) plane. In addition to the growth temperature, post-annealing in oxygen could also affect the near-surface quality of the Sr_2FeMoO_6 samples. A detailed study of the electronic structure and chemical-state composition of the Sr_2FeMoO_6 film as grown on MgO(001) at 800°C and upon annealing in oxygen will be provided by depth-profiling XPS. The XPS analyses for the as-grown and post-annealed samples both show the existence of $SrMoO_4$ as a secondary phase predominantly on the film surface and not in the sub-grain boundaries in the bulk.

In section 3.4, the effect of the substrate-induced strain on the Sr_2FeMoO_6 films grown epitaxially on MgO(001), $SrTiO_3$(100) and $LaAlO_3$(100) will be discussed. In this section, the PLD was used to deposit Sr_2FeMoO_6 films with different thicknesses on the aforementioned substrates, in order to provide a systematic study of the strain/relaxation

induced by the substrate-film lattice mismatch and of their effects on the growth evolution. The optimized growth conditions to obtain epitaxial single-phase Sr_2FeMoO_6 films on MgO (Section 3.3) have been employed. Furthermore, to minimize variations in the growth conditions, the Sr_2FeMoO_6 films are deposited simultaneously on all three substrates (MgO, $SrTiO_3$ and $LaAlO_3$). Their surface roughness and morphology are determined by atomic force microscopy (AFM), while the lattice parameters and crystal quality are characterized by high-resolution X-ray diffraction with ω-2θ scans and reciprocal space mapping.

3.2 Formation of Nanocrystalline Film of Sr_2FeMoO_6 on Si(100) by Pulsed Laser Deposition: Observation of Preferential Oriented Growth[1]

3.2.1 Experimental detalis

A NanoPLD system (PVD Products) with a base pressure better than 5×10^{-7} torr was used for the film growth experiments. A laser fluence of 400 mJ/pulse was used and the repetition rate was set to 10 Hz. The Si(100) substrates (99.99% purity, Waferworld), 10×10 mm^2 in size, were mounted on the substrate holder. The 1-inch diameter Sr_2FeMoO_6 target (99.95% purity) was obtained commercially (from MTI). With the target-to-substrate distance set to 42 mm, thin films were deposited on the Si substrates for a preselected period of time, with the substrates held at a fixed temperature between 400°C and 800°C. For each growth condition, the morphology of the resulting film was characterized by field-emission scanning electron microscopy (FE-SEM, LEO 1530) and atomic force microscopy (AFM, DI Nanoscope IV) operated in tapping mode. The local magnetic moments were measured by magnetic field microscopy (MFM) using a Co-Cr tip. The total magnetic moment was measured by using a SQUID magnetometer (Quantum Design). The structure of the film was analyzed by glancing-incidence X-ray diffraction (GIXRD) in a PANalytical X'Pert Pro MRD system, equipped with a X-ray mirror as the incident beam optics and a parallel plate collimator as the diffracted beam optics.

3.2.2 Results and Discussion

3.2.2.1 Effect of growth temperature on the crystal structure and magnetic properties

The Figure 3-5a shows the GIXRD data collected at an incidence angle ω=0.5° for the films grown on Si(100) at three different temperatures. For a laser fluence of 400 mJ/pulse [4-5 J/cm^2][2] and a deposition time of 30 minutes, the resulting film thicknesses are estimated to be 114 nm by lift-off lithography and AFM. For the sample grown at 800°C, we

---

[1] This work is being published in J. Appl. Phys. (In press 2009).

[2] The laser energy density reported here was measured on the target surface. We have noticed phase separation of the Sr_2FeMoO_6 for higher laser fluences of 550 mJ/pulse [5.5-7.5 J/cm^2] .

observe a series of peaks at 2θ = 32.0°, 39.5°, 45.8°, 66.8° and 76.0° (identified by • in Figure 3-5a), corresponding respectively to the (112), (202), (004), (224), and (116) planes of Sr_2FeMoO_6 (JCPDS 70-4092), and a small feature at 2θ=44.6° (identified by ○ in Figure 3-5a) that is attributed to the (110) plane of α-Fe (JCPDS 87-0721). The presence of metallic iron has been observed previously by Besse et al. in a PLD-grown Sr_2FeMoO_6 film on a $SrTiO_3$ substrate at 856°C [78]. For the sample grown at 600°C (Figure 3-5a), the α-Fe feature is not evident and only single-phase Sr_2FeMoO_6 is observed. The weak features generally found in the 2θ=50-60° region (shown in the inset of Figure 3-5a) can be attributed to the Si substrate, because they are also observed solely on bare Si substrates [81]. The prominent peak at 2θ=45.0° observed for the sample grown at 400°C (identified by ▲ in Figure 3-5a) can be assigned to the (204) plane of $SrMoO_4$ (JCPDS 70-2537). Upon searching the PDF database, the remaining two peaks at 2θ=31.4° and 65.6° (denoted by Δ in Figure 3-5a) can be attributed to Sr_xFeMoO_y, with the best match being $Sr_3FeMoO_{6.5}$ (JCPDS 52-1715). Evidently, the growth at a lower temperature (400°C) does not produce the stoichiometric Sr_2FeMoO_6 phase.

The corresponding SEM and AFM images for the Sr_2FeMoO_6 films grown on Si(100) at the respective temperatures are also compared in Figure 3-5. The film grown at 400°C appears to be fairly smooth (Figure 3-5d), with a root mean squared (RMS) roughness of 1.8 nm for a 4 μm^2 sampling area as determined by AFM. On the other hand, the largely Sr_2FeMoO_6 films grown at 600°C (Figure 3-5c) and 800°C (Figure 3-5b) look more granular, with RMS roughnesses of 6.9 nm and 34.3 nm for a 4 μm^2 sampling area, respectively. Accordingly, the average grain size for the film grown at 600°C (Figure 3-5c) as estimated by AFM (210 nm) is found to be less than half of that for the film grown at 800°C (540 nm, Figure 3-5b). The morphology of the Sr_2FeMoO_6 film grown at 600°C in the present work (Figure 3-5c) is very similar to that obtained by other groups [56,82]. Energy dispersive X-ray analysis at 20 kV has also been used to identify the elemental stoichiometry of the as-grown films. In particular, the ratio of the atomic percent of Fe to Mo changes from 0.7 to 1.2 to 0.9 for the films grown at 400°C, 600°C and 800°C, respectively. This is consistent with the GIXRD results (Figure 3-5a) that show the film

grown at the lower temperature (400°C) contains additional Mo-rich crystalline phase such as $SrMoO_4$.

By applying the Scherrer analysis to the prominent diffraction peaks at 2θ=45.05°, 45.66°, and 45.88° for the films grown at 400°C, 600°C and 800°C respectively, we estimate the respective grain sizes to be 66.2 nm, 68.8 nm and 172.5 nm, which follow the similar trend of increasing grain size with increasing growth temperature as depicted by the SEM and AFM images (Figure 3-5). This is also consistent with the increasing roughness with increasing growth temperature seen with AFM. However, the average grain sizes for the films grown at 800°C (540 nm) and 600°C (210 nm), as shown in their respective SEM images (Figure 3-5b and Figure 3-5c), appear much larger than that obtained by the Scherrer analysis, which suggests that the grains in the SEM and AFM images may consist of multiple nanocrystals and/or contain a substantial number of defects. On the other hand, for the primary $SrMoO_4$ film obtained at 400°C, the average grain size as depicted by SEM and AFM appears smaller than that obtained by the Scherrer analysis. The results shown in Figure 3-5 illustrate that a good-quality, single-phase Sr_2FeMoO_6 film can be obtained on a Si substrate at a growth temperature as low as 600°C. Figure 3-6a shows the corresponding magnetic moment as a function of applied magnetic field up to 5 T, measured at 77 K using a SQUID magnetometer. The magnetic field is applied parallel to the film surface. The diamagnetic contribution from the Si(100) (a linear contribution with slope of -6.04×10^{-9} emu/T) substrate has been subtracted from the data. A saturation magnetic moment of $3.4\pm0.1\ \mu_B$ per formula unit (after appropriate normalization to the film volume) is observed. The corresponding coercive field is found to be 1.5 kOe. For the film grown at 800°C, we also obtain the same saturation magnetic moment (of $3.4\pm0.1\ \mu_B$ per formula unit) but a lower coercive field of 0.8 kOe. With 1-2% of Fe second phase in the film grown at 800°C, the actual magnetic moment of the Sr_2FeMoO_6 film is still 2.84-2.27, as determined using the analysis of Besse et al. [78]. The larger coercive field found for the film grown at 600°C is consistent with the smaller grain size obtained at this lower temperature.

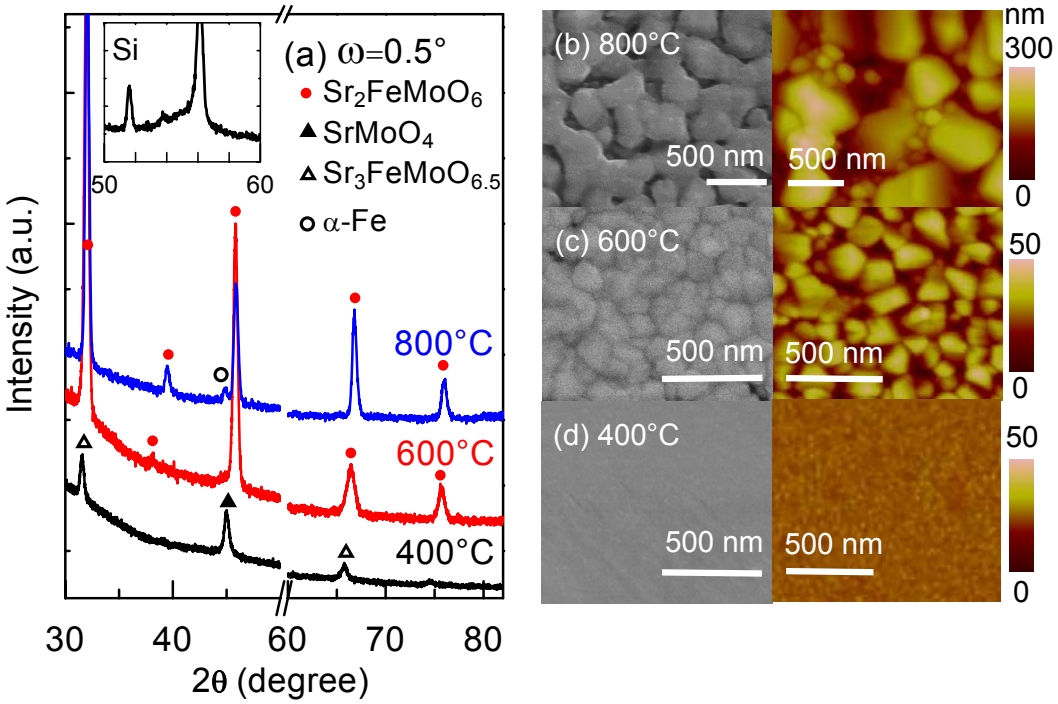

Figure 3-5: GIXRD spectra recorded at incident angle ω=0.5° (left column), SEM (centre column) and AFM images (right column) for samples grown on Si(100) with a laser fluence of 400mJ/pulse for 30 minutes at (a,b) 800°C, (a,c) 600°C, and (a,d) 400°C. Features corresponding to Sr_2FeMoO_6 (JCPDS 70-4092), $SrMoO_4$ (JCPDS 70-2537), α-Fe (JCPDS 87-0721) and a rarely observed $Sr_3FeMoO_{6.5}$ phase (JCPDS 52-1715) are identified by solid circles (•), solid triangles (▲), open circles (○) and open triangles (Δ), respectively. The y-axis is in log scale. For the AFM images (b), (c) and (d), the respective RMS roughness parameters are 34.3 nm, 6.9 nm and 1.8 nm.

Figure 3-6b and Figure 3-6c show the corresponding AFM and MFM images (taken at room temperature) for the film grown at 600°C, respectively. In accord with the SEM image (Figure 3-5c), the AFM image (Figure 3-6b) reveals an uniform distribution of regularly shaped grains with an average size of 210 nm. With the magnetic tip magnetized prior to the measurement, several MFM images have been recorded at different lift heights of 30, 50, 80 and 120 nm. All of these MFM images are found to be similar except for the one at 120 nm lift height that shows very low contrast. A lift height of 30 nm has been used for collecting the MFM image shown in Figure 3-6c, which clearly reveals ferromagnetic

behaviour at room temperature. The magnetic domains appear to have an irregular, elongated shape of 0.5×1 μm^2, which is considerably larger than the grain size (210 nm), indicating that the Sr_2FeMoO_6 grains are well connected electromagnetically. For the samples grown at 400°C and 800°C, we were not able to obtain a MFM image. This is consistent with the lower coercive field for these films, as obtained by SQUID magnetometer measurements at 77K.

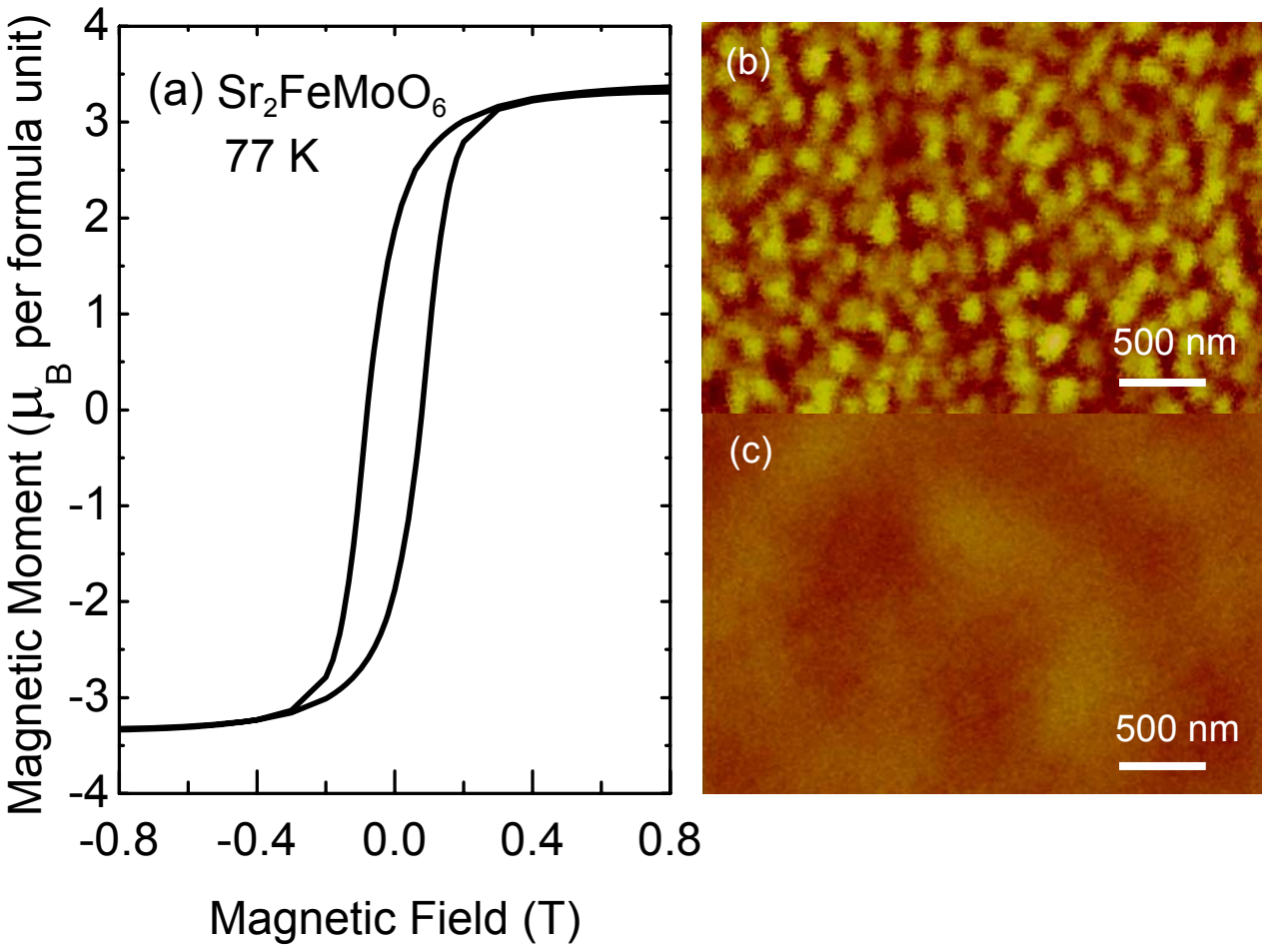

Figure 3-6: (a) Magnetic moment as a function of applied magnetic field collected at 77 K for the Sr_2FeMoO_6 film grown on Si(100) at 600°C, and the corresponding (b) AFM image, and (c) MFM image obtained at a lift height of 30 nm, both collected at room temperature. The height contrast range for the AFM image is 50 nm full-scale.

3.2.2.2 Effects of deposition time

In order to study the growth evolution of Sr_2FeMoO_6 on Si(100) at 600°C, we have obtained films for different deposition times of 1, 10, 20, 30 and 60 minutes. We characterize the morphology of the as-grown films, their respective film thicknesses and average crystal sizes by using SEM, AFM and GIXRD, respectively. The growth characteristics of these films are summarized inTable 3-1. Evidently, the corresponding growth rate appears to have stabilized at ~ 4 nm/minute after about 20 minutes of deposition. The film thicknesses were determined by lift-off lithography and AFM, and while there is some scatter in the data, Table 3-1shows that the film thickness increases linearly with deposition time. The respective SEM and AFM images for the as-grown films shown in Figure 3-7 all reveal uniform distributions of grains. The film with the shortest deposition time (1 minute) exhibits the smallest grain size, with a RMS roughness of 0.8 nm over an area of 4 μm^2 (Figure 3-7a). Above a deposition time of 10 minutes, the RMS roughness of the thicker film appears to be relatively constant (Table 3-1). For the 60-minute film (Figure 3-7e), a network of cracks is seen to develop over the entire film surface, which may be due to differences in the thermal expansion characteristics between the Si(100) substrate and the thick Sr_2FeMoO_6 film. Furthermore, the average crystal size has been deduced from the full width at half maximum (FWHM) of the (004) peak of Sr_2FeMoO_6 by using the Scherrer analysis. The average crystal size is found to clearly increase with increasing deposition time (Table 3-1).

Table 3-1: Film thickness, RMS roughness and crystal size for Sr_2FeMoO_6 films grown on Si(100) at 600°C with different deposition times.

Deposition time (minute)	Film thickness[a] (nm)	RMS roughness ± 2 (nm)	Crystal size[b] (nm)
1	7	0.8	c
10	60	7.6	12.3
20	84	6.6	33.2
30	114	6.9	86.3
60	268	8.1	123.2

[a] The accuracy of the film thickness measurement is ±5 nm.

[b] The average crystal size is obtained by applying the Scherrer analysis to the (004) diffraction line of Sr_2FeMoO_6. The (110) diffraction line of a strain-free W target at $2\theta = 40.26°$ with FWHM=0.4° has been used as a standard.

[c] For the 1-minute film, no diffraction lines are observed.

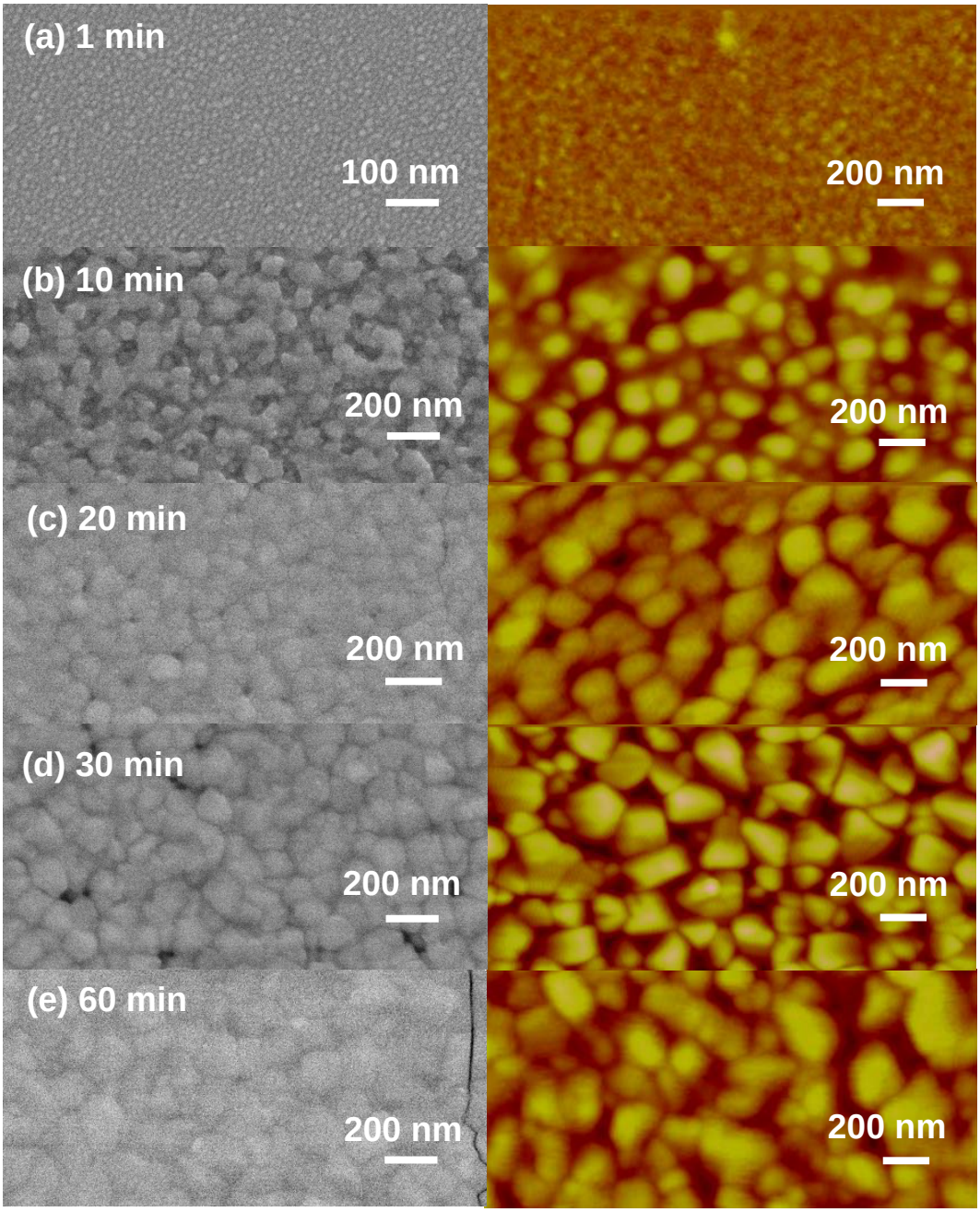

Figure 3-7: SEM (left) and AFM images (right) of the Sr_2FeMoO_6 films grown on Si(100) at 600°C with a laser fluence of 400 mJ/pulse for deposition times of (a) 1, (b) 10, (c) 20, (d) 30, and (e) 60 minutes. The height contrast range in all the AFM figures is 70 nm, except for the film grown for 1 min shown in (a) with a height contrast range of 10 nm.

In addition to providing the average crystal size, GIXRD can also be used to obtain the composition of the crystal phase and orientation as a function of depth by varying the incident angle. This technique has been used to study the residual strain and stress in thin films and to characterize crystalline phases and structures of the near-surface in thin films and organic materials [83,84,85]. The dependence of X-ray 1/e penetration depth, D, as a function of the incident angle, ω, can be determined by the following equation:

$$D(\omega) = \frac{\lambda}{4\pi}\left(\frac{\sqrt{(\omega^2-\omega_c^2)^2+4\beta^2}+\omega^2-\omega_c^2}{2}\right)^{-(\frac{1}{2})} \qquad \text{Equation (1)}$$

where λ is the wavelength of the X-ray (1.54 Å for Cu K_α radiation), ω_c is the critical angle where total reflection occurs, $\beta = \frac{\mu\lambda}{4\pi}$ and μ is the corresponding mass attenuation coefficient (1175 cm^{-1}) [83,84,86]. Depending on the material, the typical value for ω_c ranges from 0.2° to 0.6° for Cu K_α radiation. D(ω) has been measured and calculated for different materials [83,84,85,87], and it generally ranges from a few nanometers for ω=0.1° to a micrometer for ω=1°. For our Sr_2FeMoO_6 samples, the critical angle has been found to be ω_c=0.34°±0.02° by a reflectivity measurement on an epitaxial film grown on a MgO(001) substrate in a separate experiment [88]. The corresponding penetration depth increases from 57 nm for ω=0.1° to 560 nm for ω=1.0°.

For the sample obtained by the 1-minute deposition (Figure 3-7a), no diffraction features are found at incident angles larger than ω=0.2°, which is consistent with a very thin film (~7 nm, Table 3-1). A small diffraction peak at 2θ=28.5° is observed for ω=0.2° (not shown) and it could be assigned as SrO_2(101). However, there is no trace of the corresponding higher-intensity (110) peak of SrO_2, which makes the nature of this film uncertain. Figure 3-8 a compares the GIXRD spectra recorded with different incident angles for the samples obtained with 10-minute (Figure 3-7b), 30-minute (Figure 3-7d), and 60-minute depositions (Figure 3-7e). For the thinner 10-minute film (60 nm, Table 3-1), two peaks at 2θ=31.8° and 2θ=45.7°, corresponding respectively to the (112) and to the (004) and possibly (220) planes of Sr_2FeMoO_6, are observed at the surface of the film with ω=0.2°.

For higher incident angles of 0.5° and 0.9°, both diffraction features appear to shift to a lower 2θ angle. The width of the shifted (112) peak is unchanged while that of the shifted (004)+(220) feature becomes larger, suggesting the presence of a second phase of α-Fe with the (110) line at 2θ=44.6° (JCPDS 87-0721). The peak shift observed with increasing X-ray penetration depth into the film is consistent with the crystal lattice expansion of the film in the Sr_2FeMoO_6/Si interface region. This could be caused by a number of factors, including different thermal expansion coefficients[3] [51,22] between Sr_2FeMoO_6 and Si, and local oxygen deficiencies due to the presence of native silicon oxide. For the thicker 30-minute (114 nm,Table 3-1) and 60-minute films (268 nm, Table 3-1), the same two Sr_2FeMoO_6 features for the (112) and (004)+(220) planes can be seen at ω=0.2° (Figure 3-8a). At higher incident angles, additional features attributed to Sr_2FeMoO_6(002) at 2θ=22.4° and α-Fe(110) at 2θ=44.6° become evident. The peak shifts for the 30-minute and 60-minute films are less than that observed for the 10-minute film. This is to be expected because the Sr_2FeMoO_6/Si interface region contributes a smaller percentage of the total diffraction signal for these thicker films.

In Figure 3-8b, we show the corresponding intensity ratio of the (004)+(220) to (112) lines as a function of the incident angle for the three films. For the 10-minute film, this ratio (0.4±0.1) is found to be close to the literature values for randomly oriented, polycrystalline Sr_2FeMoO_6 powders (0.442). In contrast, the relative intensity ratio found for the 60-minute film is much larger, and decreases almost monotonically from 2.2 to 1.4, as the incident angle is increased from 0.3° to 0.9°. There is some scatter in the data below the critical angle, ω_c=0.34°. As the X-rays should be reflected below ω_c, diffraction peaks below ω_c could be caused by imperfections in the sample surface (i.e. surface roughness) and artifacts of sample geometry, which also lead to the larger intensity scatter observed in this region. The intensity ratios for films grown with intermediate thicknesses (e.g. the 30-minute film) follow a progression from the thin-film value (0.4) to the thicker-film value (1.4). This suggests that the grain orientation differs throughout the thickness of the film, where the

[3] Thermal expansion coefficient for Si is 2.6×10^{-6} $^{\circ}C^{-1}$ [22] and for double perovskite Sr_2FeMoO_6 reported to be around 10×10^{-6} $^{\circ}C^{-1}$ [50].

Sr_2FeMoO_6 grains are more oriented at the film surface than the Sr_2FeMoO_6/Si interface. For the thicker films, we also see an increase in the intensity of the (002) peak at $2\theta=22.4°$.

These results indicate preferential growth of (001) oriented Sr_2FeMoO_6 grains, during long film depositions. Since the GIXRD data is convoluted with sample imperfections such as surface roughness and possible parasitic second phases (including metallic iron and $SrMoO_3$), it is difficult to estimate the extent of the preferential growth. The observed preferential oriented growth may be due to the influence of the laser plume on the Sr_2FeMoO_6 film growth during the PLD process, similar to the well-known ion-beam assisted deposition PLD technique, which has been used to introduce textured films on non-epitaxially matched substrates. Furthermore, developing the capability of synthesizing a high-quality oriented Sr_2FeMoO_6 film on Si will open up prospects for many potential applications. More detailed understanding of the mechanism behind this preferential growth will be presented in future work, as we investigate how the oriented growth depends on other variables including laser fluence, substrate-target distance, and gas enviroment during growth.

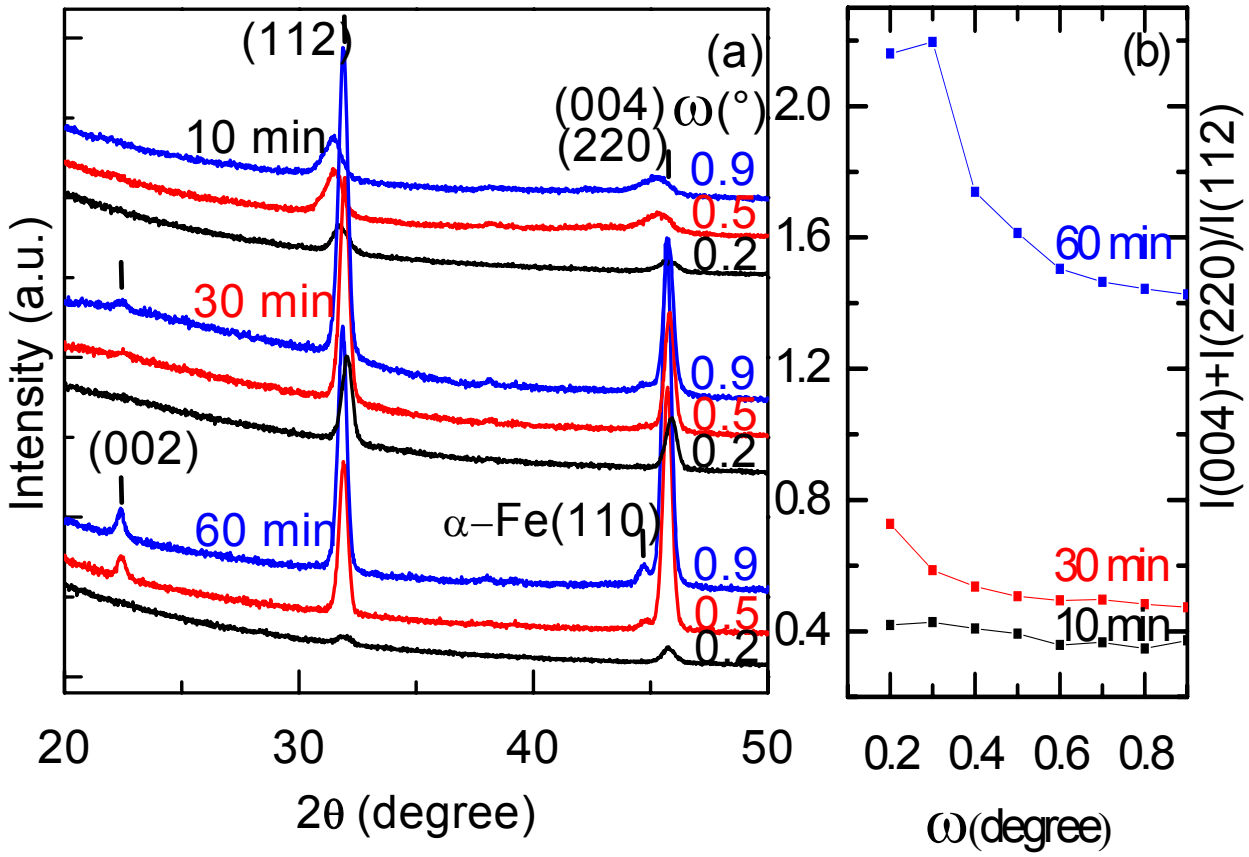

Figure 3-8: (a) GIXRD spectra collected at different incident angles, ω = 0.2°, 0.5° and 0.9°, for Sr_2FeMoO_6 films grown on Si(100) for 10 minutes (top), 30 minutes (middle) and 60 minutes (bottom) deposition time. The y-axis is in log scale. (b) shows the corresponding intensity ratios of the (004)+(220) to (112) diffraction lines as a function of ω for the three films.

3.2.3 Concluding Remarks

Using PLD, we have deposited and fully characterized Sr_2FeMoO_6 thin films on Si(100) substrates under different growth temperatures and deposition times. In contrast to the earlier work, nanocrystalline, single-phase Sr_2FeMoO_6 films could be obtained at a lower growth temperature (600-800°C). Furthermore, the ferromagnetic films on Si(100) grown at 600°C are found to be of high quality, with saturation magnetic moments (3.4 μ_B per formula unit at 77 K) that are comparable to the best Sr_2FeMoO_6 films epitaxially grown on lattice-matched substrates (such as $SrTiO_3$ and MgO) reported to date. As revealed by MFM, the as-grown film also exhibits micrometer-sized magnetic domains at room temperature, which are signficantly larger than the grain sizes (200-250 nm). The low growth temperatures and the non-magnetic nature of the Si substrate are useful for reducing chemical diffusion that may impair the magnetic properties of the Sr_2FeMoO_6 film. Moreover, by changing the X-ray incident beam angle, we also measure the diffraction patterns and determine the respective crystal structures of the film as a function of depth. For the as-grown Sr_2FeMoO_6 films thicker than 60 nm, a preferential orientation of the nanocrystals in the film is observed. The mechanism for the preferential oriented growth on Si, despite the lack of lattice matching, is unknown and additional studies will be conducted to further investigate this intriguing effect.

3.2.4 Preliminary results on target-to-substrate distance effect: Preferential orientation of nanocrystalline Sr_2FeMoO_6 growth on Si

The origin of the preferential orientation growth on nanocrystalline Sr_2FeMoO_6 remained a puzzle when we submitted the above work to J. Appl. Phys. In order to further investigate the origin of this effect, additional experiments were done. In particular, films were deposited at exactly the same conditions (60 min deposition time) as discussed in Section3.2.1, but the target-to-substrate distance was changed from 34 to 58 mm. The GIXRD result of those films is chosen in Figure 3-9. The distance between the target and the substrate clearly affects the ratio of the (004)+(220) to (112) lines, and at d=42 mm, the highest ratio can be obtained.

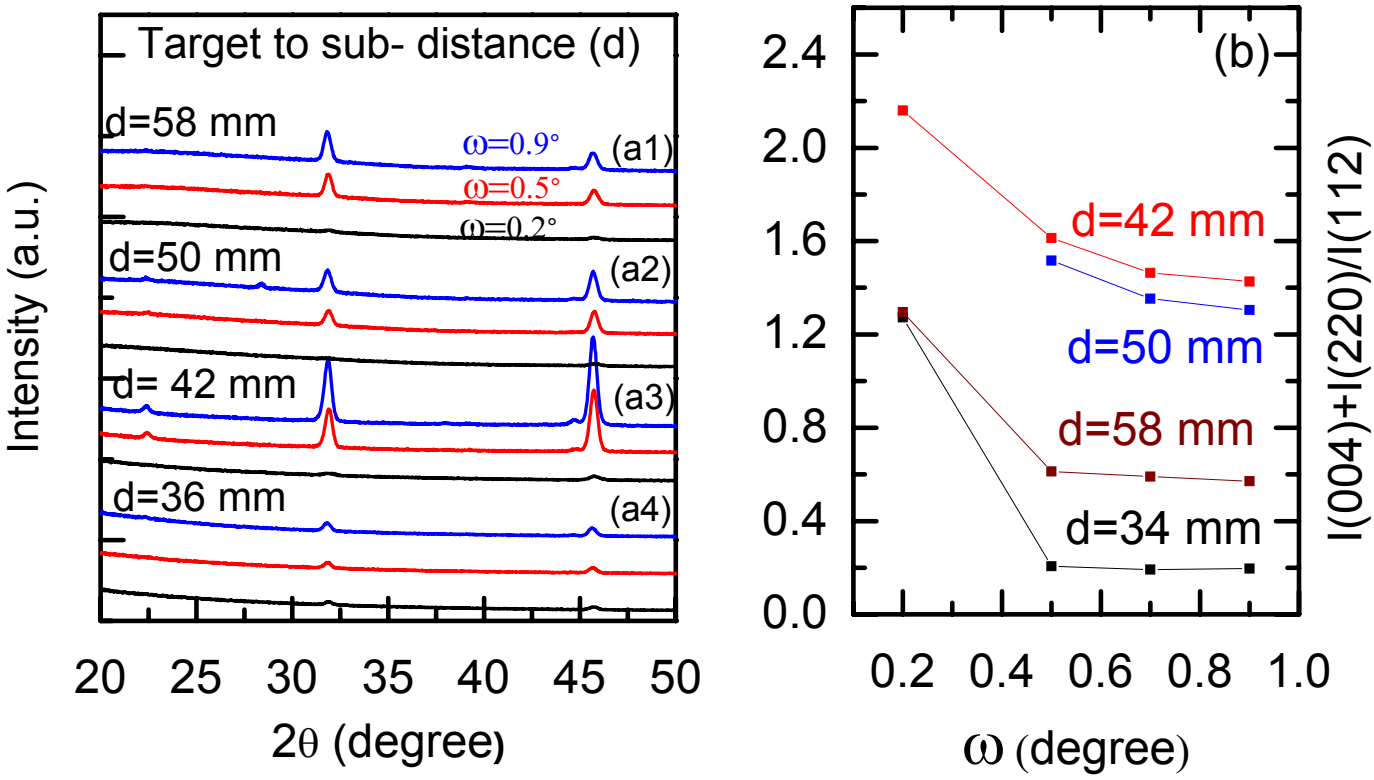

Figure 3-9: (a) GIXRD spectra collected at different incident angles, ω = 0.2°, 0.5° and 0.9°, for Sr_2FeMoO_6 films grown on Si(100) for target to substrate distance of (a1) d= 36 mm, (a2) d=42 mm, (a3) d=50 mm and (a4) d=58 mm. (b) The corresponding intensity ratios of the (004)+(220) to (112) diffraction lines as a function of ω for the four films.

3.3 X-ray photoemission study of Sr_2FeMoO_6 and $SrMoO_4$ films epitaxially grown on MgO(001): Near-surface chemical-state composition analysis[4]

3.3.1 Experimental Details

A NanoPLD system with a laser fluence of 400 mJ/pulse was used for the film growth experiments. An 1-inch diameter Sr_2FeMoO_6 target was obtained commercially (MTI Corp.). A 5×10 mm^2 MgO(001) epi-polished substrate was mounted face-down above the target with a target-to-substrate distance of 42 mm. The substrate was heated by infrared lamps irradiating the back side, and the substrate temperature was monitored by a thermocouple and an optical pyrometer. With the substrate held at a preselected temperature between 400°C and 800°C, deposition was performed in vacuum for 30 min. For the post-annealing experiment, the sample was held at 800°C in 10 mTorr of O_2 gas at a flow rate of 20 sccm for 40 min, followed by 2 hours of annealing at the same temperature in vacuum.

The morphology and stoichiometry of the as-grown and post-annealed films were characterized by using scanning electron microscopy and energy-dispersive X-ray spectrometry (EDX), respectively. To obtain the crystal structures of the as-grown films, high resolution X-ray diffraction (XRD) data were collected with ω-2θ scans. by using a PANalytical X'Pert Pro MRD X-ray diffractometer, equipped with a two-bounce hybrid monochromator and a Cu K_α source for the incident beam optics and a triple-axis section as the diffracted beam optics. To determine the film thickness, an X-ray reflectivity measurement was made with an X-ray mirror as the incident beam optics and a parallel-plate collimator as the reflected beam optics. Magnetization data of the as-grown films were obtained by using a SQUID magnetometer (Quantum Design) capable of operating at a 7 T magnetic field. The chemical-state composition of the films were studied by using a Thermo-VG Scientific ESCALab 250 X-ray photoelectron spectrometer (XPS), equipped with a monochromatic Al K_α X-ray source (1486.6 eV) at a typical energy resolution of 0.4-0.5 eV full-width-at-half-maximum (FWHM). For the depth-profiling experiments, argon

[4] This work has been submitted to Phys. Rev. B (Dec 2008).

sputtering was performed over a rastered area of 3×3 mm^2 of the sample at an ion beam energy of 5 keV. The collected XPS data were fitted, where appropriate, with a combination of Gaussian-Lorentzian lineshapes, after correction for the Shirley background, by using the CasaXPS software.

3.3.2 Results and Discussion

A series of Sr_2FeMoO_6 film samples were grown in vacuum at several temperatures of 400°C, 500°C, 600°C, 700°C, and 800°C, and the resulting as-grown films all appeared as black. The SEM images for the films grown at 400°C, 600°C, and 800°C shown in Figure 3-10 reveal generally smooth surfaces, with root-mean-square roughness of 0.6, 7.1, and 8 nm over 12 μm^2, respectively, as measured by atomic force microscopy. Randomly distributed nanoparticles (<20 nm in size) are also found on top of the latter two films. Consistent with the XPS data, they may be attributed to oxides of Fe and Mo segregating on the surface during the deposition. The film grown at 800°C has also been further annealed in O_2 using the procedure discussed earlier. Unlike the other as-grown films, the post-annealed film appeared yellow-brown in colour and was non-conducting. The corresponding SEM image (Figure 3-10d) also shows a smooth surface with a greater number of larger nanoparticles (20-100 nm in size) mostly with a cubic shape. The presence of these cubic nanoparticles has also been reported by Besse et al. [89], who attributed them to be iron oxide based on their XRD measurement. We also deposited a Sr_2FeMoO_6 film at 800°C in an argon atmosphere of 10 mTorr (not shown), and the resulting film did not show any discernible difference from the film shown in Figure 3-10c, which was grown in vacuum.

Figure 3-11a shows the ω–2θ XRD scans for films grown at 600°C, 700°C, and 800°C before and after annealing in O_2. In addition to the strong (002) peak of the MgO substrate at 42.9° (JCPDS 4-0829), the strong peak at 45.7° and the weaker peak at 22.4° can be attributed respectively to the (004) and (002) planes of Sr_2FeMoO_6 (JCPDS 70-4092). Evidently, a single-phase epitaxial Sr_2FeMoO_6 film has already been formed at a deposition temperature as low as 600°C. Rocking curve analysis of the (004) plane of the as-grown films (not shown) indicates that the peak width narrowed from 1.1° FWHM for the film

grown at 600°C to 0.3° FWHM for the film grown at 800°C, consistent with improved crystal quality for films grown at a higher temperature. Before post-annealing in O_2, the as-grown film at 800°C consists of Sr_2FeMoO_6 oriented with the (001) direction parallel to the MgO(001) plane. After post-annealing in O_2, the amount of Sr_2FeMoO_6 is reduced, and two new peaks at 29.7° and 61.5° attributed to the (004) and (008) planes of $SrMoO_4$ (JCPDS 70-2537) are observed (Figure 3-11a, top curve). This indicates the formation of a significant amount of an oriented $SrMoO_4$ phase, with its (001) plane parallel to the MgO(001) plane [as well as to the (001) plane of Sr_2FeMoO_6], upon post-annealing in O_2. For the samples grown at temperature lower than 600°C (e.g. Figure 3-10a), no features other than the substrate peaks are observed, despite the presence of discernible films on the substrates. The lack of any observable Sr_2FeMoO_6 peaks may be due to the Sr_2FeMoO_6 forming an amorphous film on the MgO(001) substrate.

Figure 3-11b shows the ϕ-scans for the Sr_2FeMoO_6(112) plane, corresponding to the diffraction peak at 2θ=32.01°, ω=16.00° and ψ=45.0°, for the films grown at (A) 600°C, (B) 700°C, and (C) 800°C. The presence of four equally spaced diffraction peaks indicates that the Sr_2FeMoO_6 films form epitaxial single crystals on the MgO, and not just c-axis aligned polycrystalline films. A similar ϕ-scan for the $SrMoO_4$(112) plane, corresponding to the diffraction peak at 2θ=27.67°, ω=13.84° and ψ=57.6°, for the 800°C sample post-annealed in O_2 is shown as (D). As with Sr_2FeMoO_6, the 4-fold symmetry of the (112) plane for $SrMoO_4$ indicates that this material is also epitaxially aligned with the MgO substrate.

The magnetization curves for the as-grown film at 800°C before and after annealing in O_2 have been measured at 5 K for a magnetic field up to 5 kOe by using a SQUID magnetometer and are shown in Figure 3-12a. The diamagnetic signal due to the MgO(001) substrates has been removed from the data. In order to calculate the saturation magnetic moment, the film thickness is required and may be deduced from a measurement of the X-Ray reflectivity for the as-grown film, shown in Figure 3-12b. The thickness of the film (t) is related to the separation between interference fringes ($\delta\omega$) by the formula: $t = \frac{\lambda}{2\delta\omega}$, where λ is the wavelength of the X-ray (1.54 Å for Cu K_α). The presence of well-defined fringes also

indicates that the film thickness is almost constant over the entire film, and the film surfaces are smooth. Using the film thickness obtained from the reflectivity measurements (98 nm) and the dimensions of the sample measured by a micrometer, the maximum saturation magnetic moments were found to be 3.4±0.1 μ_B/f.u. for the as-grown film and 1.4 ±0.1 μ_B/f.u. upon post-annealing. The saturation magnetic moment of the Sr_2FeMoO_6 film as-grown on MgO(001) is therefore considerably larger than the values reported earlier (1.0 μ_B/f.u. at 300 K [70] and 2.3 μ_B/f.u. at 20 K [80]), which indicates the superior quality of the as-grown film. The formation of $SrMoO_4$ upon post-annealing of the as-grown film reduces the saturation magnetic moment (the effect of the antisite disorder cannot be excluded), which could also account for the lower saturation magnetic moment found in the earlier work. However, the coercive fields (0.56 kOe) for both the as-grown and post-annealed films are found to be the same (Figure 3-11a), supporting the result from the φ-scans in Figure 3-11b that post-annealing in O_2 has no effect on grain formation. The coercive field for the film grown at 600°C was also measured (not shown), and the larger value (1.2 kOe) is consistent with the rocking curves with larger FWHMs found in samples grown at a lower temperature.

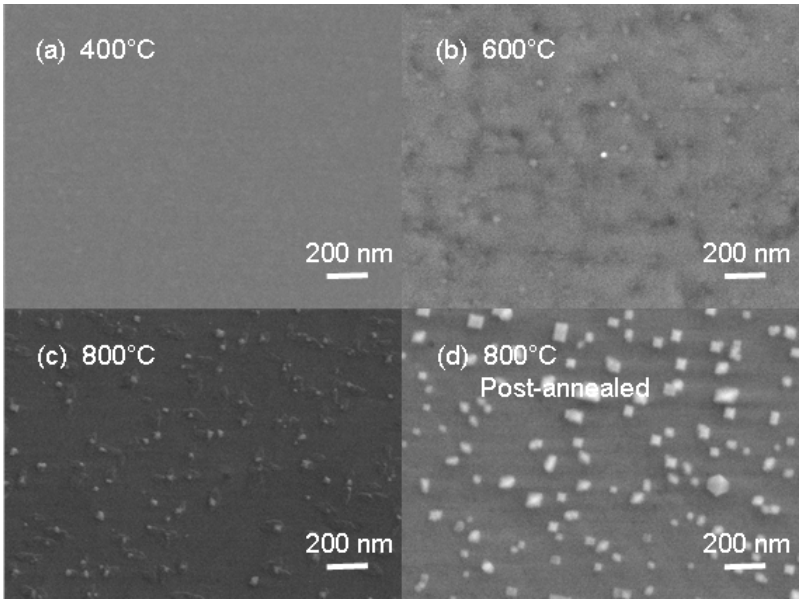

Figure 3-10: SEM images of Sr_2FeMoO_6 PLD-grown on MgO(001) in vacuum at (a) 400°C, (b) 600°C and (c) 800°C, and (d) of sample (c) after post-annealing in O_2.

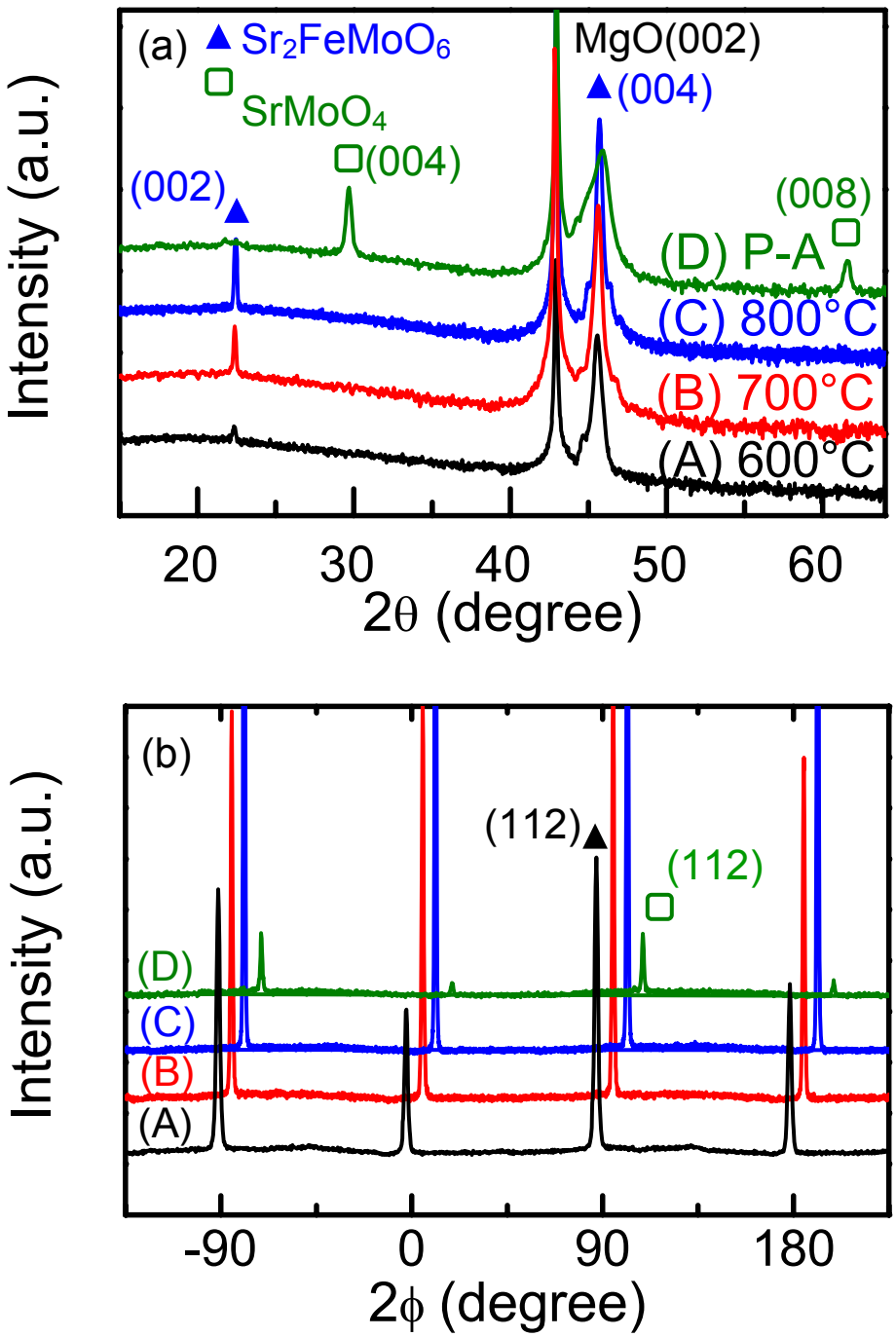

Figure 3-11: (a) ω–2θ scans of Sr_2FeMoO_6 films PLD-grown on MgO(001) in vacuum at (A) 600°C, (B) 700°C, and (C) 800°C. The top curve (D) corresponds to sample (C) post-annealed (P-A) in 10 mTorr of O_2. (b) shows the corresponding ϕ-scans of (A,B,C) the Sr_2FeMoO_6(112) plane (2θ=32.01°, ω=16.00° and ψ=45.0°) and (D) $SrMoO_4$(112) plane (2θ=27.67°, ω=13.84° and ψ=57.6°). All data are plotted with a logarithmic y-axis, with the curves offset for clarity.

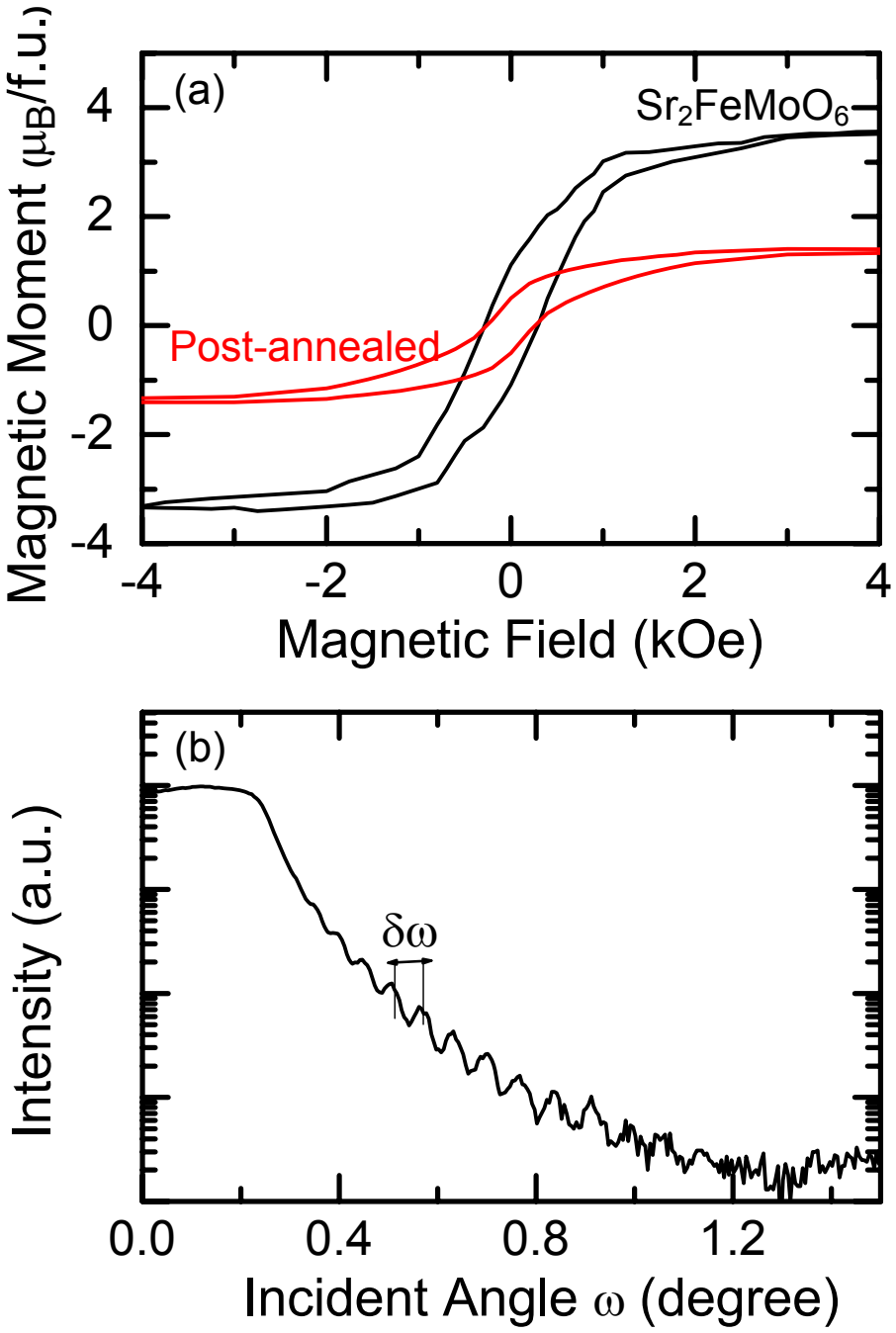

Figure 3-12: (a) Magnetization as a function of applied magnetic field for a Sr_2FeMoO_6 film PLD-grown on MgO(001) in vacuum at 800°C and upon post-annealing in O_2. (b) X-ray reflectivity measurement of the as-grown Sr_2FeMoO_6 at 800°C as a function of incident angle. Since we could not calculate the thickness of the $SrMoO_4$ overlayer, the uncertainty remains in the calculation of the saturation magnetic moment for the post-annealed sample.

Figure 3-13 compares the XPS spectra of the valence band and O 1s regions as a function of sputtering time for the as-grown Sr_2FeMoO_6 film before and after annealing in O_2. For the as-grown Sr_2FeMoO_6 film, three well-defined features at 0.9 eV, 5.7 eV and 8.3 eV can be observed (Figure 3-13b). Sputtering the film for 10 s appears to remove the feature at 0.9 eV and strengthen the features at 5.7 eV and 8.3 eV, and to expose two new features at 1.8 eV and 11.3 eV. Further sputtering for 40 s sharpens all four features, and a small shoulder is seen to emerge at 0.4 eV. Continued sputtering for extended periods (over 160 s) substantially reduces the feature at 8.3 eV, while all other features at 0.4 eV, 1.8 eV, 5.7 eV and 11.3 eV remain essentially unchanged. The depth profiles of these valence-band features suggest that the "overlayer" region, with a discernibly different composition from the bulk region, can be removed after ~40 s of sputtering. The observed features at 0.4 eV, 1.8 eV, 5.7 eV, 8.3 eV and 11.3 eV are found to be in good accord with the photoemission measurement made for polycrystalline Sr_2FeMoO_6 by Ray et al. [90]. Their ab-initio calculations further showed that their observed features near 0.4 eV, 1.8 eV, 5.6 eV, and 8.3 eV originate from the Mo 4d, Fe 3d, O 2p and Mo 4d bands, respectively. Similar assignments have also been made by Kuepper et al. [91] in their combined study involving XPS and a local-density-approximation band structure calculation of polycrystalline Sr_2FeMoO_6.

For the Sr_2FeMoO_6 film after the annealing treatment, the evolution of the observed features with sputtering (Figure 3-13d) appears to be similar to that of the as-grown film (Figure 3-13b). The notably stronger relative intensity of the feature at 8.3 eV for the post-annealed film (Figure 3-13d) than that of as-grown film after 40 s of sputtering (Figure 3-13b) suggests a thicker overlayer region for the former.

The difference in the overlayer region of the as-grown Sr_2FeMoO_6 film before and after annealing can be better illustrated in their respective O 1s XPS spectra. In particular, two peaks at 530.4 eV and 532.0 eV with nearly equal intensities can be observed for the as-grown film (Figure 3-13a). Just 10 s of sputtering appears to reduce the feature at 532.0 eV, and to substantially enhance the feature at 530.4 eV. The spectrum becomes essentially unchanged after further sputtering for 40 s. In contrast, the O 1s spectrum of the annealed

film exhibits a singular, intense feature at 532.0 eV (Figure 3-13c). Only after sputtering for 160 s has the feature at 532.0 eV been reduced sufficiently to expose the feature at 530.4 eV, the intensity of which remains unchanged upon further sputtering. The observed evolution of these O 1s features with respect to sputtering time (depth) is consistent with a thicker overlayer found for the annealed film than that for the as-deposited film, as inferred earlier from the valence-band spectra (Figure 3-13b, d). Based on the XRD spectra of the annealed film (Figure 3-11, Curve D), the overlayer can be attributed to $SrMoO_4$. Given the detection limit of XRD is about 1% (for the bulk), the lack of $SrMoO_4$ XRD features in the as-grown film (Figure 3-11) is consistent with the thin $SrMoO_4$ overlayer as reflected in the depth-profiling XPS spectra (with a detection limit of 0.5% for the surface). It should be noted that the notable increase in the overall spectral intensity for the 10-s spectra (for both as-grown and annealed films) relative to the original spectra (i.e. before sputtering) is due to the removal of surface carbonaceous layer commonly found on materials exposed to air.

Figure 3-14 shows the corresponding XPS spectra of Sr 3d and Fe 2p regions for the as-grown Sr_2FeMoO_6 film before and after annealing. Evidently, both samples exhibit a doublet of Sr $3d_{5/2}$ ($3d_{3/2}$) at 133.7 eV (135.5 eV), with a spin-orbit splitting of 1.8 eV and an intensity ratio of 3:2 (Figure 3-14b, d). The binding energy positions of these Sr 3d features are in good accord with the literature values for Sr^{2+} in a perovskite structure [92,93]. Sputtering did not appear to change the overall intensity or the profile of the doublet, which indicates that the $SrMoO_4$ overlayer and the Sr_2FeMoO_6 film have similar local chemical environments for the Sr atoms. Sr is coordinated to four Mo atoms in the tetragonal hole in $SrMoO_4$ [94] and to four Mo and four Fe atoms in the tetragonal hole in the Sr_2FeMoO_6 lattice. However, given the fact that a Mo atom is larger and has more electrons that a Fe atom, the local Sr chemical environment in Sr_2FeMoO_6 is expected to be dominated by the larger Mo atoms. The prominence of the Mo electron densities in Sr_2FeMoO_6 apparently leads to Sr 3d binding energy shifts that are too small to be distinguishable from those in the $SrMoO_4$ overlayer and therefore not detectable by our present XPS system.

The depth-profiling Fe 2p XPS spectra for the as-grown Sr_2FeMoO_6 film (Figure 3-14a) are also found to be essentially the same as those of the film after annealing (Figure

3-14c). In particular, the as-deposited film exhibits a doublet of Fe $2p_{3/2}$ ($2p_{1/2}$) at 710.8 eV (723.8 eV), the intensity of which becomes reduced upon sputtering above 10 s. A new doublet at 708.8 eV (722.0 eV) emerges upon sputtering, first appearing as a shoulder after 10 s of sputtering and increasing in intensity with increasing sputtering time. In accord with the literature values for the Fe 2p binding energies of FeO and Fe_2O_3 [95], we can assign the Fe $2p_{3/2}$ ($2p_{1/2}$) features at 710.8 eV (723.8 eV) and 708.8 eV (722 eV) to Fe^{3+} and Fe^{2+} oxidation states, respectively. After sputtering for 40 s, a sharp doublet at 707.4 eV (720.5 eV) is found and becomes the prominent feature upon further sputtering above 160 s. This lowest-binding-energy feature can be attributed to metallic Fe (Fe^0), which is produced by reduction of the higher Fe oxidation states due to Ar ion sputtering [96]. It should be noted that the lack of a metallic Fe peak for the as-grown film (Figure 3-14a) confirms the high film quality of the present PLD-grown Sr_2FeMoO_6 film and the absence of any significant amount of Fe phase in the film, in contrast to the earlier work that reported an additional metallic Fe peak for their as-deposited film [97]. The as-grown film is found to have mixed oxidation states, with Fe^{3+} as the majority oxidation state relative to the Fe^{2+} oxidation state. Furthermore, the nearly identical intensity evolution with respect to sputtering time found for both as-grown and post-annealed films suggests that the cubic nanoparticles seen in the post-annealed film in Figure 3-10c consist of Fe_2O_3, which has the same Fe^{3+} oxidation state as in Sr_2FeMoO_6. The decrease of the saturation magnetic moment in the post-annealed film (Figure 3-12a) is consistent with the nanoparticles mainly consisting of antiferromagnetic α-Fe_2O_3.

Figure 3-15 compares the XPS spectra of the Mo 3d region as a function of sputtering time for the as-grown Sr_2FeMoO_6 film before and after annealing, both of which depict evolution of rather complex sets of peaks. In Figure 3-15c, we select the spectrum for the as-grown film after 40 s of sputtering as the spectrum representative of the interface region, in order to illustrate the fitting of the complex spectral envelope into four sets of Mo $3d_{5/2}$ ($3d_{3/2}$) doublets. A spin-orbit splitting of 3.1 eV [98] and a $3d_{5/2}$:$3d_{3/2}$ intensity ratio of 3:2 have been used for the fitting, after appropriate correction of the background with a single Shirley (Gaussian-step) function. Using the literature values for different Mo oxides

[95,99,100] we assign the observed Mo $3d_{5/2}$ ($3d_{3/2}$) features at 228.5 eV (231.6 eV), 230.8 eV (233.9 eV), 232.2 eV (235.3 eV), and 233.7 eV (236.7 eV) to Mo^0 (i.e. metallic Mo), Mo^{4+}, Mo^{5+}, and Mo^{6+} states, respectively. An excellent fit has been obtained when the peak widths for the Mo^0, Mo^{4+} , Mo^{5+} and Mo^{6+} features were set to 1.0±0.2 eV, 2.4±0.2 eV, 1.2±0.2 eV and 1.3±0.2 eV FWHM, respectively.[5] Although the peak widths are inherently related to the natural lifetimes of the states, the larger widths found for the Mo^{4+} features could be due to the presence of close-lying many-body states or defects states as hypothesized by Kuepper et al. [91]. It should be noted that the Mo 3d spectrum shown in Figure 3-15c is in excellent accord with the experimental [53,91] and calculated spectra [53] of polycrystalline Sr_2FeMoO_6 reported in the literature.

The depth profiles of the fitted areas for the Mo^0, Mo^{4+}, Mo^{5+}, and Mo^{6+} $3d_{5/2}$ features with respect to the total area of the spectrum are shown for both as-grown and post-annealed films in a. Before sputtering, the as-grown Sr_2FeMoO_6 film exhibits primarily the strong Mo^{6+} features (Figure 3-15a), with the other Mo features appearing only as a weak shoulder at the lower binding energy side. Upon sputtering for 10 s to 160 s, the intensities of the Mo^{6+} features are reduced while those for the Mo^{5+} features are enhanced dramatically. In the meantime, the removal of the prominent Mo^{6+} features has exposed the underlying Mo^{4+} features. The intensities of which appear to undergo a more gradual reduction upon sputtering for 10 s to 160 s than those for Mo^{6+} features. Further sputtering above 160 s appear not to affect the relative intensities of the Mo^{4+}, Mo^{5+}, and Mo^{6+} (Figure 3-16a), and the spectral envelope remains relatively stable (Figure 3-15a). Like the Fe 2p features (Figure 3-14), the emergence of the metallic Mo^0 features at 228.5 eV (231.6 eV) after 40 s of sputtering (Figure 3-15) can be attributed to reduction of the higher oxidation states by Ar ion sputtering. The metallic Mo features could also introduce additional uncertainty to the relative intensities of the other Mo states for the spectra with sputtering for longer than 40 s.

---

[5] The residual standard deviation of the fit for all the spectra was 1-2. In order to keep the same FWHM for all the oxidation states, two additional peaks were needed in the fitting to obtain nearly the same goodness of the fit. Clearly, more complicated fitting strategies can be used in conjunction with elaborate calculations, e.g. Ref. [54]. However, this will not affect the main observation that the relative populations of these features reach their constant values shown in Figure 3-16.

The intensities of the metallic Mo features also become nearly constant after sputtering longer than 460 s.

For the Sr_2FeMoO_6 film post-annealed in O_2, the corresponding spectral evolution of the Mo $3d_{5/2}$ ($3d_{3/2}$) features as a function of sputtering time, shown in Figure 3-15b and Figure 3-16b, is found to be similar to that of the as-grown film (Figure 3-15a, Figure 3-16a). In particular, the relative intensities of the Mo^{4+}, Mo^{5+}, and Mo^{6+} states appear to reach nearly the same stable values after 460 s of sputtering for the film before and after annealing. Interestingly, a similar observation has been made for polycrystalline Sr_2FeMoO_6 grown on a Si substrate [101]. These results suggest that the $SrMoO_4$ growth occurs largely on the surface and not in the subgrain boundaries of the bulk, which confirms our earlier hypothesis that the reduction in the saturation magnetic moment (Figure 3-12a) is due to $SrMoO_4$ on the surface and not in the bulk. A notable difference between the two depth profiles (Figure 3-16) is that there appears to be a latent period (of ~10 s of sputtering) before the on-set of the changes for the post-annealed film (Figure 3-16b). Consistent with the presence of $SrMoO_4$ in the XRD data of the post-annealed film (Figure 3-11a), this indicates a thicker $SrMoO_4$ overlayer for the post-annealed film, which primarily gives rise to the Mo^{6+} features. The similarity of Mo 3d spectra for the as-grown film before and after annealing without any sputtering (Figure 3-15a, b) suggests that the formation of $SrMoO_4$ on the surface of the as-grown Sr_2FeMoO_6 film occurs readily upon exposure to air.

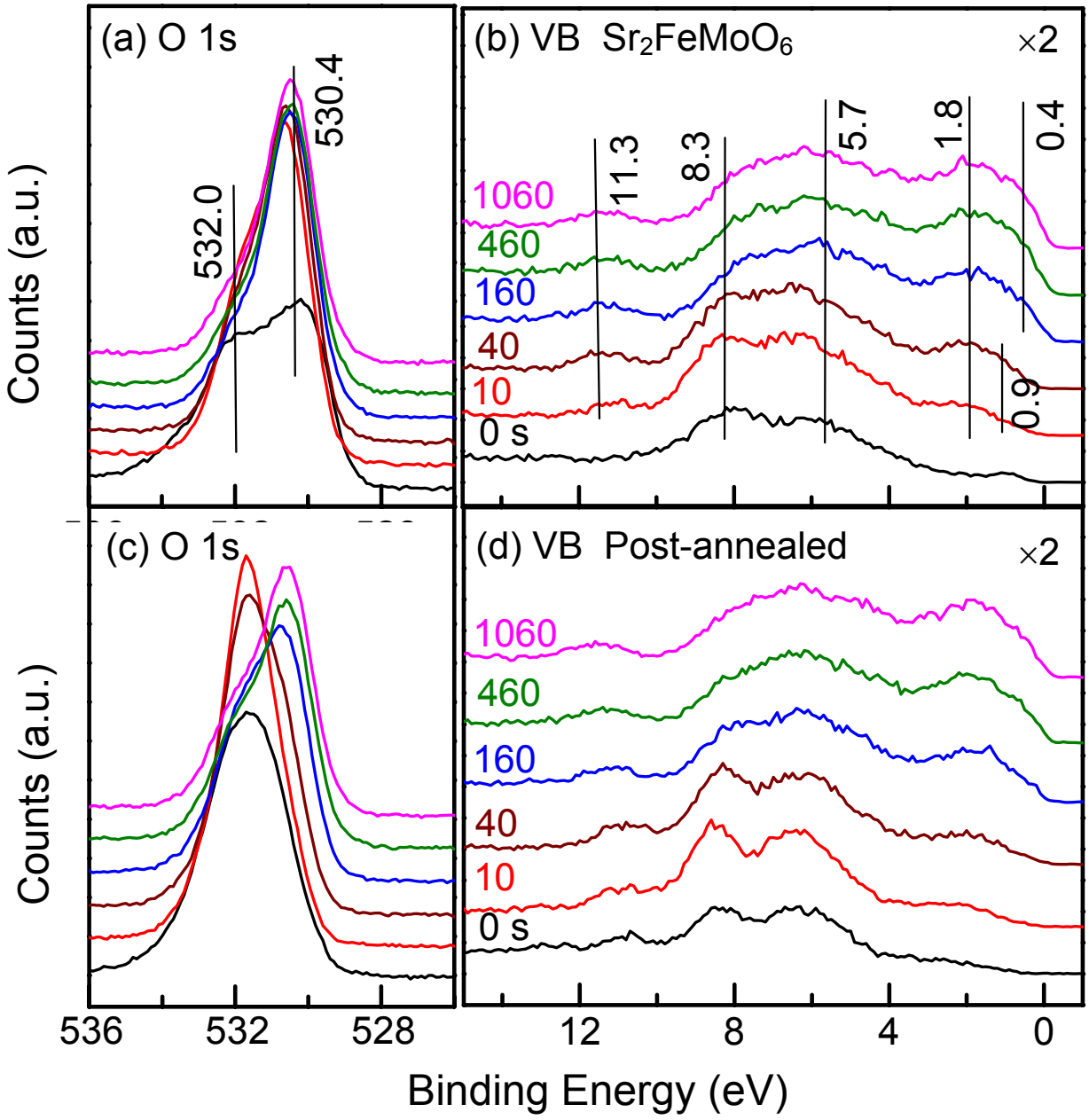

Figure 3-13: XPS spectra of (a,c) O 1s and (b,d) valence-band (VB) regions as a function of sputtering time for the PLD-grown Sr_2FeMoO_6 film on MgO(001) at 800˚C (a,b) before and (c,d) after post-annealing in O_2.

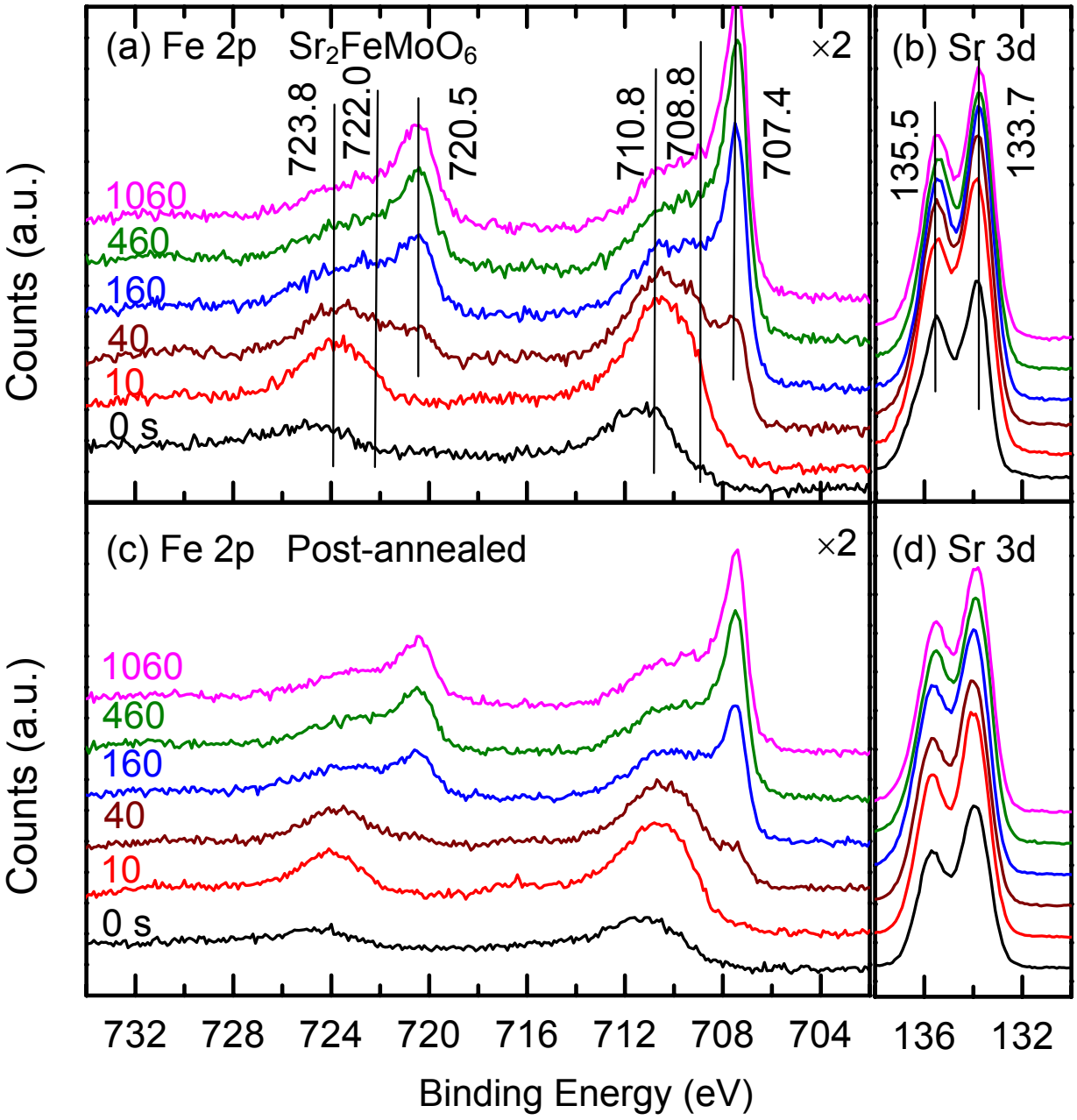

Figure 3-14: XPS spectra of (a,c) Fe 2p and (b,d) Sr 3d regions as a function of sputtering time for the PLD-grown Sr_2FeMoO_6 film on MgO(001) at 800˚C (a,b) before and (c,d) after post-annealing in O_2.

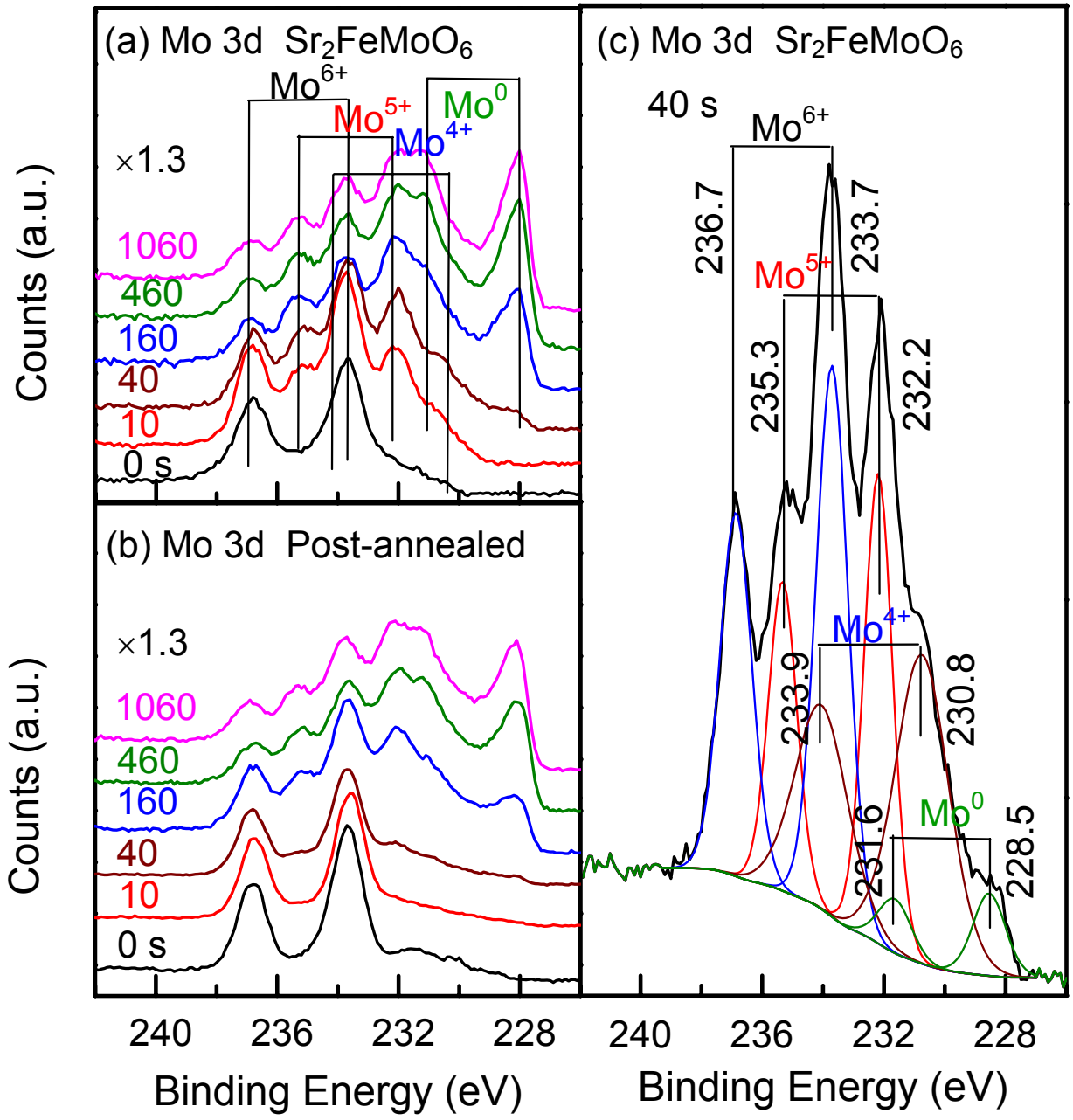

Figure 3-15: (a,b) XPS spectra of Mo 3d region as a function of sputtering time for the PLD-grown Sr_2FeMoO_6 film on MgO(001) at 800˚C before and after post-annealing in O_2. (c) Peak fitting of the spectrum for the as-grown Sr_2FeMoO_6 film after 40s of argon sputtering.

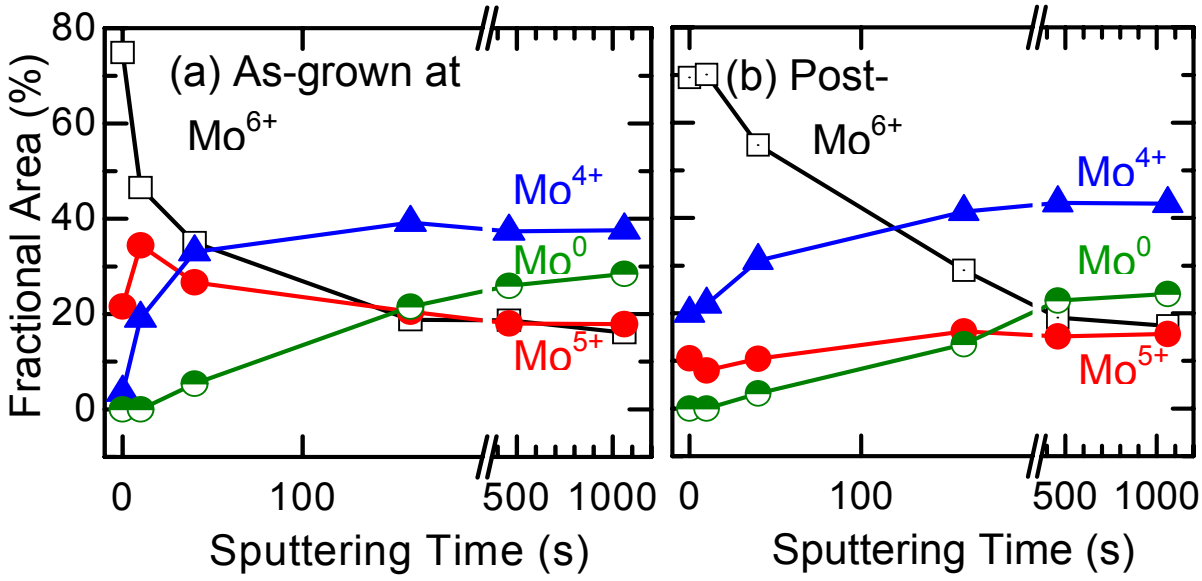

Figure 3-16: Fractional area of Mo^{n+} (with respect to the area of the overall Mo 3d spectrum) as a function of sputtering time for the PLD-grown Sr_2FeMoO_6 film on MgO(001) at 800°C (a) before and (b) after post-annealing in O_2.

3.3.3 Concluding Remarks

In summary, thin films of Sr_2FeMoO_6 have been grown on MgO(001) substrates at several temperatures (400°C, 500°C, 600°C, 700°C, and 800°C) by pulsed laser deposition. High resolution X-ray diffraction studies reveal epitaxial growth of a single-phase (double perovskite) Sr_2FeMoO_6 film on MgO(001) at a temperature as low as 600°C, with the best film quality obtained at 800°C. The film grown at 800°C was subsequently annealed in O_2, producing an additional epitaxial overlayer of $SrMoO_4$ on the Sr_2FeMoO_6 film. The magnetization data showed that the post-annealing treatment lowered the saturation magnetic moment from 3.4 μ_B/f.u. to 1.4 μ_B/f.u. with no discernible change in the observed coercive fields (0.56 kOe). This result indicates that post-annealing in O_2 has no notable effect on the grain formation in the bulk and suggests that the (thicker) $SrMoO_4$ overlayer is responsible for the observed reduction in the saturation magnetic moment. Furthermore, the lower optimal saturation magnetic moment (3.4 μ_B/f.u.) obtained for the as-grown Sr_2FeMoO_6 film than the expected value (4.0 μ_B/f.u.) could also be due to the presence of a thin $SrMoO_4$ overlayer that formed upon exposure to air. To study the film quality and chemical-state composition of the near-surface region, depth-profiling X-ray photoemission measurements of the valence-band, O 1s, Sr 3d, Fe 2p and Mo 3d regions have been performed on the as-grown and post-annealed films. The similarity in the respective depth profiles supports the formation of $SrMoO_4$ overlayers on the surfaces of both the as-grown and post-annealed Sr_2FeMoO_6 films, the thickness of which was found to be greater in the post-annealed film. Furthermore, the intensity ratios of the 3d features of Mo^{4+}, Mo^{5+}, and Mo^{6+} for Sr_2FeMoO_6 remain unchanged with sputtering depth (after 160 s), supporting the model that the observed secondary phase ($SrMoO_4$) is formed predominantly on the surface and not in the subgrain boundaries of the as-grown Sr_2FeMoO_6 film.

3.4 Growth evolution of laser-ablated Sr_2FeMoO_6: Effects of substrate-induced strain and of film thickness on the film quality and presence of secondary phase

3.4.1 Experimental Details

A NanoPLD system equipped with a KrF excimer laser was used for the film growth experiments in a base vacuum better than 5×10^{-7} torr. The laser was operating at a repetition rate of 10 Hz and a laser fluence of 400 mJ/pulse, delivering a power density of 4-5 J/cm^2. MgO(001), $SrTiO_3$(100) (STO) and $LaAlO_3$(100) were used as substrates for growing the epitaxial films, with a 1-inch diameter Sr_2FeMoO_6 (SFMO) target. With the substrates held at a fixed temperature of 800°C and a target-to-substrate distance set to 42 mm, thin films were deposited on all three substrates simultaneously for a preselected period of time (5, 10, 30, 40 and 50 minutes). For each growth condition, the morphology of the resulting film was characterized by atomic force microscope (AFM) operated in tapping mode. To study strain/relaxation and crystalline quality of the film, high-resolution powder diffraction and reciprocal space mapping (RSM) were carried out using a X-ray diffractometer. For powder XRD studies, a Ge(220) 2-bounce hybrid monochromator with a 1/2° slit and a triple-axis section with a 1/16° slit were used to define the incident and diffracted beams, respectively. For RSM measurement, the 1/16° slit was replaced by a channel-cut Ge(220) analyser in the triple-axis section for the diffracted beam optics (without changing the incident beam optics).

3.4.2 Results and Discussion

To minimize the strain induced by the STO(100), LAO(100) and MgO(001) substrates, the growth direction along the c-axis of SFMO will be parallel to the c-axes of the substrates [70,80,89,102], with the a and b axes of SFMO lying in the (110) and $(1\ \bar{1}\ 0)$ directions, respectively, of the substrates. Figure 3-17 shows a schematic diagram depicting the crystallographic relation of the SFMO film with respect to the substrate lattice. The lattice mismatch between the SFMO (a=b=5.5870 Å, c=7.9180 Å, JCPDS 70-4092) and cubic substrates of MgO (a=b=c= 4.2100 Å, JCPDS 4-0829), STO (a=b=c=3.9051 Å, JCPDS 5-0634) and LAO (a=b=c=3.7890 Å, JCPDS 85-0848) can be calculated by using the

following expression: $\frac{a_{substrate} - \frac{\sqrt{2}}{2} a_{SFMO}}{a_{substrate}}$, where $a_{substrate}$ and a_{SFMO} are the lattice parameters of the substrate and SFMO, respectively. The lattice mismatch values obtained for MgO, STO and LAO, are +6.2% , −1.2% and −4.3%, respectively. An alternative epitaxial relationship with SFMO on STO has been observed by Borges et al. [80], where the (surface normal) c axis of the substrate is parallel to the SFMO(220) direction, and the SFMO c-axis lies along the STO(a,b) surface. This type of orientation also gives a low mismatch strain, but was not observed in our films. While it is difficult to distinguish the (004) and (220) peaks from the powder (ω-2θ) scan alone, we confirmed the identification of the (004) peak by registering the presence of the high intensity (112) peak in a position consistent with a c-axis aligned film.

Figure 3-18 shows the AFM images of the SFMO films grown on MgO, STO and LAO for selected deposition times of 5, 10, and 50 minutes. Based on our previous analysis [101], the rate of deposition was estimated to be 4±2 nm/minute. Although the films were all grown simultaneously under the same growth conditions, there are clear differences among the morphologies of the films on the three substrates. The AFM image of the SFMO on MgO (Figure 3-18a) shows a large number of square terraces with an epitaxial relationship to one another, and presumably with the MgO substrate. After 10 minutes of growth (Figure 3-18b), the SFMO terraces have become larger, along with emerging growth spirals. At a higher deposition time (Figure 3-18c), the surface looks smooth but with cuboid nanoparticles atop. Given that the XRD measurement for this film does not reveal any peaks other than SFMO (002) and (004), either the amount of these nanoparticles is not sufficiently large to be detected by XRD or these nanoparticles are not crystalline. Further analysis is required to determine the nature of these nanoparticles. For the SFMO film growth on STO, the 5-minute film appears to have layered structures with larger square terraces (Figure 3-18d), which have evidently become layers in the 10-minute film and the resulting surface appears smooth (Figure 3-18e). Similar morphology has been noticed by Manako et al. [59]. The elevated square features in Figure 3-18d and Figure 3-18e have also been observed by other groups [103,104]. The resulting film on STO after 50 minutes of deposition remains

smooth with atop nanoparticles (Figure 3-18f), as was similarly observed for MgO (Figure 3-18c).

Figure 3-18g shows flake-like nanostructures for the 5-minute SFMO film grown on LAO, which become larger in the 10-minute film (Figure 3-18h). The surfaces of these films appear to be the least ordered relative to the corresponding films grown on MgO and STO, with the largest density of nucleation sites and few obvious terraces or growth spirals. The 50-minute SFMO film grown on LAO appears smooth (Figure 3-18i), with a discernibly larger density of cuboid nanoparticles than films grown on MgO and STO. The differences in morphology among the SFMO films grown on the three substrates are most obvious for the thinner films, and the appearances of the films become similar with increasing deposition time. The presence of nanoparticles on the 50-minute films grown on all three substrates suggests that these nanoparticles could originate from the same particulate formation mechanism possibly due to changes in the surface condition of the SFMO target after extended ablation.

The AFM data indicate that SFMO grows differently on different substrates. The SFMO films deposited on STO (Figure 3-18d,e,f) and, to a lesser extent, on MgO (Figure 3-18a,b,c) tend to grow more two dimensionally as in Frank-van der Merve or Stranski-Krastanov growth, while the films on LAO (Figure 3-18g,h,i) tend to show the Volmer-Weber growth mode, where there is isolated island growth in three dimensions [105]. The root-mean-square (RMS) roughness determined over the 12 μm^2 scanned area of the respective AFM images of the films grown on the three substrates is plotted as a function of deposition time in Figure 3-19. While all the films deposited on MgO, STO and LAO have similar RMS roughness of 3-4 nm after 5 minutes of growth, SFMO films grown on MgO and STO show greatly increased roughness after 10 minutes of growth. The increased RMS roughness for the SFMO films after 10 minutes growth on the MgO and STO substrates is consistent with the larger terraces and growth spirals observed in Figure 3-18b and Figure 3-18e. As the growth of these films continues to 40 minutes of deposition, the reduction in their RMS roughness parameters is in accord with the layer-by-layer growth mode. On the other hand, the SFMO films grown on LAO have a relatively constant roughness up to 40

minutes of growth, which is consistent with the Volmer-Weber growth mode observed in Figure 3-18. The sudden increase in the RMS roughness for the SFMO films grown on all three substrates after 50 minutes of deposition can be attributed to particulate formation as noted above. The layer-by-layer growth seen in the SFMO film on STO is expected due to the low strain caused by small lattice mismatch (−1.2%) between STO and SFMO. However, layer-by-layer growth is also found for the SFMO film on MgO, where the lattice mismatch is considerably larger (+6.2%). This is surprising especially when the Volmer-Weber growth is observed for SFMO film growth on LAO, where the lattice mismatch (−4.3%) is smaller.

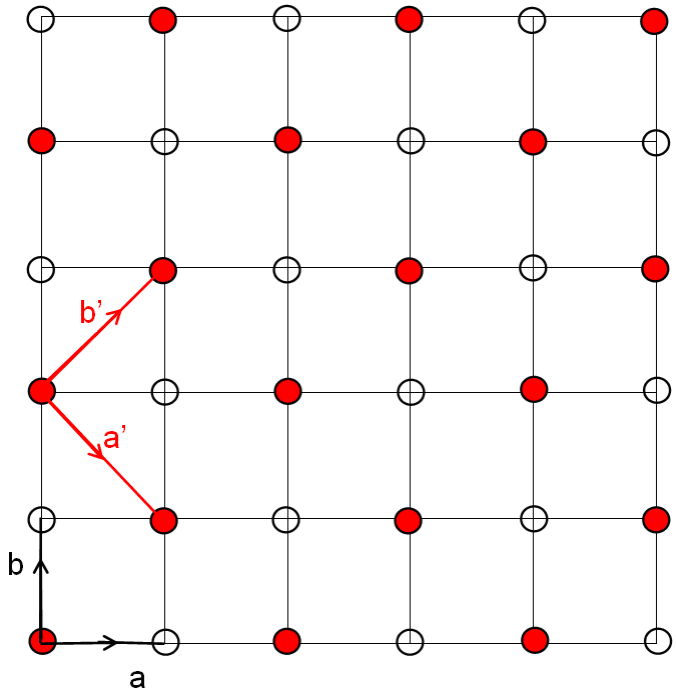

Figure 3-17: Two-dimensional schematic diagram of the cubic lattice structure of the substrate (open circles) with a and b lattice vectors, and the (110) plane of Sr_2FeMoO_6 (solid circles) with a' and b' lattice vectors. The c axes are out of plane.

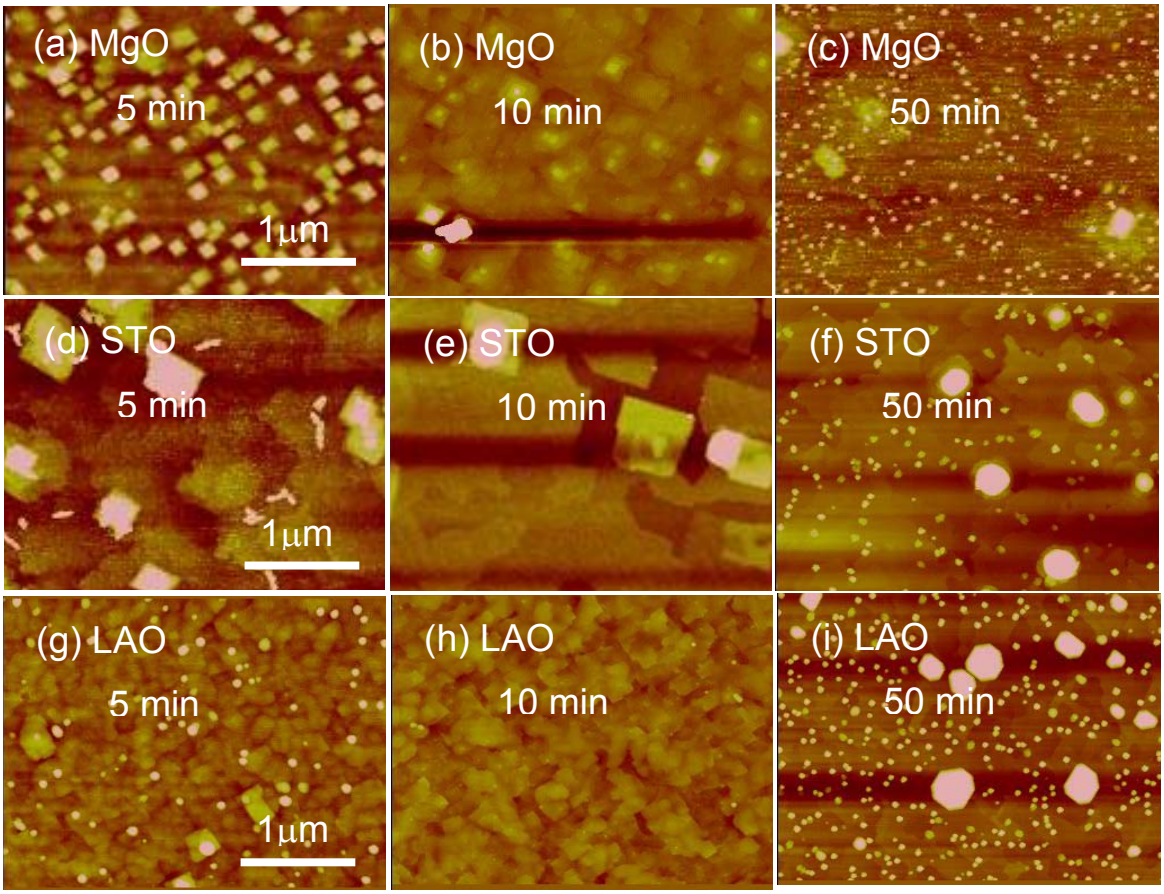

Figure 3-18: AFM images of Sr_2FeMoO_6 films grown for selected deposition times of 5 minutes (left column), 10 minutes (centre column), and 50 minutes (right column) on MgO(001) (top row), $SrTiO_3$(100) (middle row) and $LaAlO_3$(100) (bottom row). The ranges for the height contrast for the AFM images of 5-, 10- and 50-minute films are 30, 30 and 60 nm, respectively.

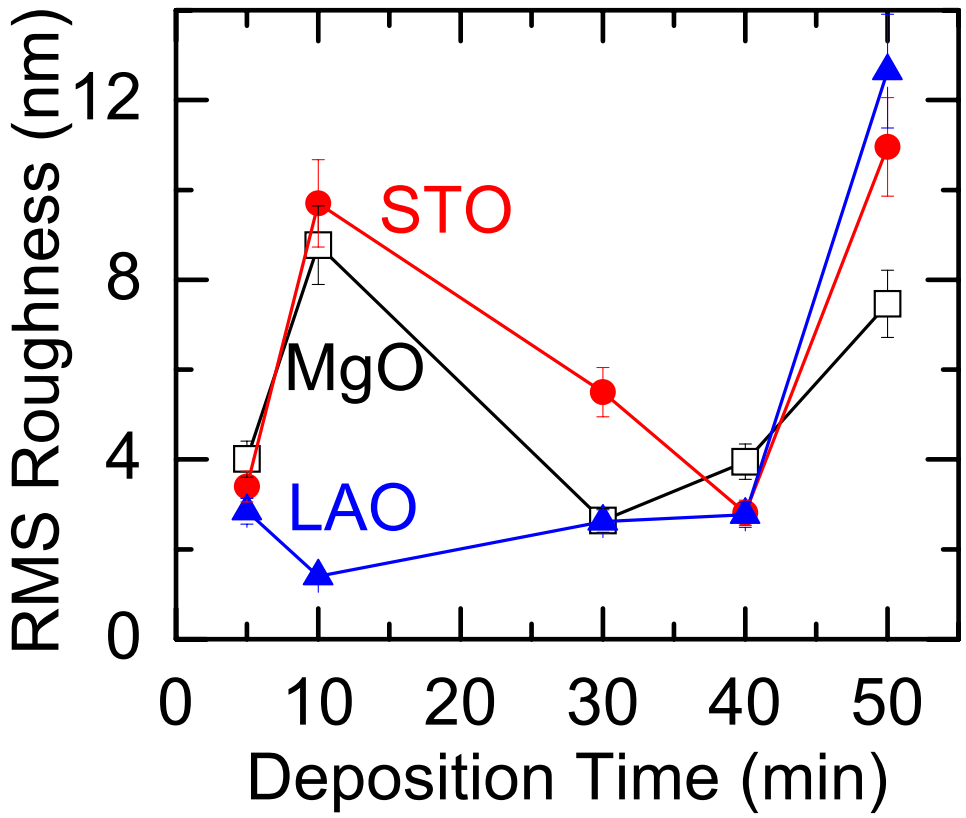

Figure 3-19: Root-mean-square (RMS) roughness as a function of deposition time for Sr_2MoFeO_6 films grown on MgO(001) (open squares, □), $SrTiO_3$(100) (solid circles, ●) and $LaAlO_3$(100) (solid triangles, ▲). The RMS roughness is obtained over the 12 μm^2 scanned area of the respective AFM image.

To further investigate the crystal quality of the SFMO films grown on the three substrates, detailed X-ray diffraction studies were carried out. Figure 3-20 shows the ω-2θ scans for selected SFMO films deposited for 10 and 50 minutes on MgO(001), LAO(100), and STO(100). Evidently, in addition to the (100) substrate peaks, two prominent SFMO planes of (002) and (004) can be observed, which indicate that the SFMO films were all epitaxially grown along the c-axis of the substrates. For the films grown on MgO, no other feature can be seen regardless of the deposition time. However, for the films deposited on

STO and LAO, even though thinner films (with deposition time less than 20 minutes) are single phase, increasing the deposition time promotes the parasitic phases with a predominant $SrMoO_4$ phase (JCPDS 70-2537), and minor Fe_2O_3 (JCPDS 40-1139) and MoO_2 phases (JCPDS 32-0671). This result is in contrast with the work by Boucher [106], who grew SFMO films with different thicknesses on several substrates and measured their cation compositions. He concluded that the compositions of the thicker films are the same regardless of the substrate, but those of the thinner films were affected by the MgO and LAO substrates.

Rocking curve analysis has been performed to extract the peak widths of the (004) plane of SFMO films grown on the three substrates for different deposition times, shown in Figure 3-21. STO has the best lattice match with SFMO and therefore gives the lowest value for the FWHM of the rocking curve (0.34°±0.1°). There is no significant change in the FWHM for the longer deposition times, indicating the consistent crystalline quality even for thicker films. For the SFMO films grown on MgO, the corresponding rocking curve has a larger FWHM value of 0.63°±0.1° for the 5-minute deposition, and then decreases slowly to 0.37°±0.1° for 50-minute deposition, indicating an improvement in crystal quality for thicker films. Consistent with the AFM images presented in Figure 3-18, the SFMO films on LAO exhibit the largest FWHM values between 0.9° and 1.7°, and no trend in the FWHM value with deposition time was evident.

In order to study the evolution of the crystal quality during epitaxial growth, reciprocal space map measurements were performed to extract in-plane and out-of-plane lattice parameters for all the samples. In RSM, the lattice mismatch and degree of relaxation are independent of the ω and 2θ scanning ratio and the miscut of the surface with respect to the diffraction lattice plane. By using the Ge(220) analyser in the triple-axis section to condition the diffracted beam, it is possible to achieve high enough resolution to resolve close-lying features [30]. A series of ω-2θ scans around the symmetric SFMO (004) plane and asymmetric SFMO (112) plane were performed to construct the RSMs. The relationships between the scan parameters, ω and 2θ, and the reciprocal space vectors, Q_x and Q_y, are given by the following formulae:

$$Q_x = K[\cos\omega - \cos(2\theta - \omega)]$$
$$Q_y = K[\sin\omega + \sin(2\theta - \omega)]$$

where K (=$2\pi/\lambda$) is the magnitude of the X-ray wavevector, ω is the angle between primary X-ray beam and the sample surface, and the 2θ is the angle between incident and diffracted X-ray beam [27]. Commercial software, Panalytical Expert Epitaxy, was used to analyze the data. It should be noted that different colour contrast indicate different intensities in a log scale, and because the step sizes and dwell times were not the same for the scans in all the measurements, the intensities from map to map are not comparable. In each of the RSMs shown in Figure 3-22, shows the RSMs for the SFMO (004) plane, each of which depicts an intense (002) substrate peak and a considerably weaker and broader (004) SFMO peak. Evidently, the positive lattice mismatch between MgO and SFMO puts the SFMO film under tensile strain. On the other hand, the negative lattice mismatches between the STO and LAO substrates with the SFMO films induces compressive strains in the SFMO films. The size of the SFMO lattice with respect to those of the substrates is clearly reflected by the relative location of the SFMO(004) peak with respect to the (002) peak of the substrate. The SFMO(004) peak lies at a larger Q_y value than the MgO(002) peak (with a +6.2% lattice mismatch) but at a smaller Q_y value than the STO(002) peak (with a −1.2% lattice mismatch) and LAO(002) peak (with a −4.1% lattice mismatch). The characteristic twinning of the (002) peak along the Q_x direction for the LAO substrate can also be observed. Furthermore, the SFMO peak is moving along the Q_y direction, towards the location of the substrate peak with increasing deposition times (for the STO and LAO substrates), indicating that the c axis lattice length of the SFMO film is undergoing rearrangement to approach that of the bulk SFMO. For the STO (Figure 3-22, middle row) and LAO substrates (Figure 3-22, bottom row), the emergence of a second weak feature in the broad SFMO peak along the Qy direction can be clearly observed after 30 minutes of growth, which indicates the formation of a secondary phase, as also observed in the corresponding ω-2θ scans for STO and LAO in Figure 3-20. The creation of this secondary phase appears to release the strain, allowing the SFMO film lattice parameters to more closely approach those of bulk SFMO.

The behaviour of the SFMO film lattice parameters during growth on the three substrates can be quantified by examining the changes in the a, b and c-axis lengths as a function of deposition time, as shown in Figure 3-23. From the RSM in Figure 3-22, the c-axis length can be determined from the separation of the film and substrate peak positions. From the RSM of the Sr_2FeMoO_6 (112) plane (not shown) and the c-axis length determined from Figure 6, we obtain the corresponding a and b axis lengths [107]. For the STO substrate, despite its smallest lattice mismatch (−0.9%), the c-axis lengths of the SFMO films are found to be the largest, in agreement with the earlier work [108,102,106,103,109,110]. This large c-axis strain is consistent with a high degree of epitaxy and the quasi-2-D growth observed in Figure 3-18d and Figure 3-18e. Furthermore, the decrease in the c-axis length toward to the bulk value [obtained for SFMO powder, 7.918 Å (JCPDS 70-4092)] with increasing deposition time can be viewed as strain relief in a thicker film. Similar trends in the a and b axis lengths are also observed, where the a and b values for the 50-minute film reach the bulk values (5.58 Å). For the SFMO films grown on LAO (with a lattice mismatch of −4.3%), the c-axis length also follows a decreasing trend with increasing deposition time from 10 minutes to 50 minutes of deposition, similar to that found for the SFMO films on STO. The corresponding a and b-axis lengths, however, do not follow the same trend (as that on STO), with the a and b values becoming even smaller than the bulk values for the longer deposition times. It may be that the poorer crystal quality of the SFMO films grown on LAO can introduce some uncertainty in locating the SFMO peak maxima in the respective RSMs, especially for the shorter deposition times. While Boucher [106] did not determine the a and b axis lengths, he also found that the c-axis lengths for the SFMO films on LAO are smaller than those for SFMO films on STO. Interestingly, the a, b and c-axis lengths for the SFMO films on MgO (with a lattice mismatch of +6.2%) are found to be the closest to the bulk value, and they appear almost constant and independent of the film thickness. Using the lattice parameters, the unit-cell volumes of the SFMO films have been calculated. For the SFMO grown on STO, the volume increases from 248.6 $Å^3$ (for the 10-minute film) to 250.1 $Å^3$ (for the 50-minute film), while the corresponding volume for the SFMO films grown on

MgO was almost constant (249.4±0.3 $Å^3$). The unit cell volume values obtained for all the SFMO films grown on different substrates are larger than the bulk value of 246 $Å^3$.

For all the SFMO films, the c-axis length is larger than the bulk value. The larger out-of-plane lattice (c) constant for SFMO films has also been noted by several other groups [103,108,109,110], although few groups have also determined the SFMO a and b axis lengths. The observed larger value has been attributed to several origins, including a change in the ordering of the Fe and Mo atoms in the lattice [110], thermal strain induced by different thermal expansion coefficients upon cooling from the growth temperature [109], changes in the oxygen concentration during growth [108,110], lattice mismatch for the SFMO grown on STO [108,109], or existence of parasitic phases [106]. In particular, Sanchez et al. [103] reported the variation of c-axis length for SFMO on STO as a function of growth temperature and film thickness. Their results showed that the c-axis length decreases towards the bulk value with increasing growth temperature and led them to state that the film quality improves at a higher growth temperature. However, several other groups have noted the growth of different parasitic phases, such as $SrMoO_4$ [102,103], at high temperatures and different background oxygen pressure. As we observe in the RSM (Figure 3-22), the formation of the secondary phases could help to relief the strain, therefore reducing the c-axis length. For SFMO films on LAO (−4.3%), because its lattice mismatch is much larger than that on STO (−1.2%), one might expect the former films to also have larger c-axis lengths than those on STO. On the other hand, the SFMO films on LAO are found to have more nucleation sites and more defects than those on STO, as seen from the rocking curve data in Figure 3-21. The presence of more defects in the former films therefore helps to relieve the strain caused by the lattice mismatch and reduce the c-axis lengths. For the SFMO films on MgO, the tensile strain (as a result of a positive lattice mismatch of +6.2%) would lead one to expect the SFMO c-axis length to be less than the bulk value, in contrast to that observed in Figure 3-22. Furthermore, the c-axis length is found to be relatively constant with increasing film thickness. Boucher also observed the near-independence of the c-axis length with thickness for SFMO films deposited on MgO by magnetron sputtering [106]. He attributed this result to reorganization of the SFMO films on MgO, similar to what was seen in

$La_{0.7}Sr_{1.3}MnO_3$ on MgO by Gommert et al. [111]. In $La_{0.7}Sr_{1.3}MnO_3$, the mismatch strain with MgO was found to be completely compensated in a narrow interface region of the substrate, after which the film grows with few defects and little strain. The observation from Figure 3-23, that the SFMO unit cell volume is increased for all the films from that of the bulk, would tend to support the hypotheses that found the changes in c-axis length are due to more than just lattice mismatch (strain) effects, and the film quality of epitaxially grown films is strongly influenced by additional factors such as Fe/Mo ordering, oxygen concentration, lattice defects (vacancies and interstitials), and substrate-film interdiffusion.

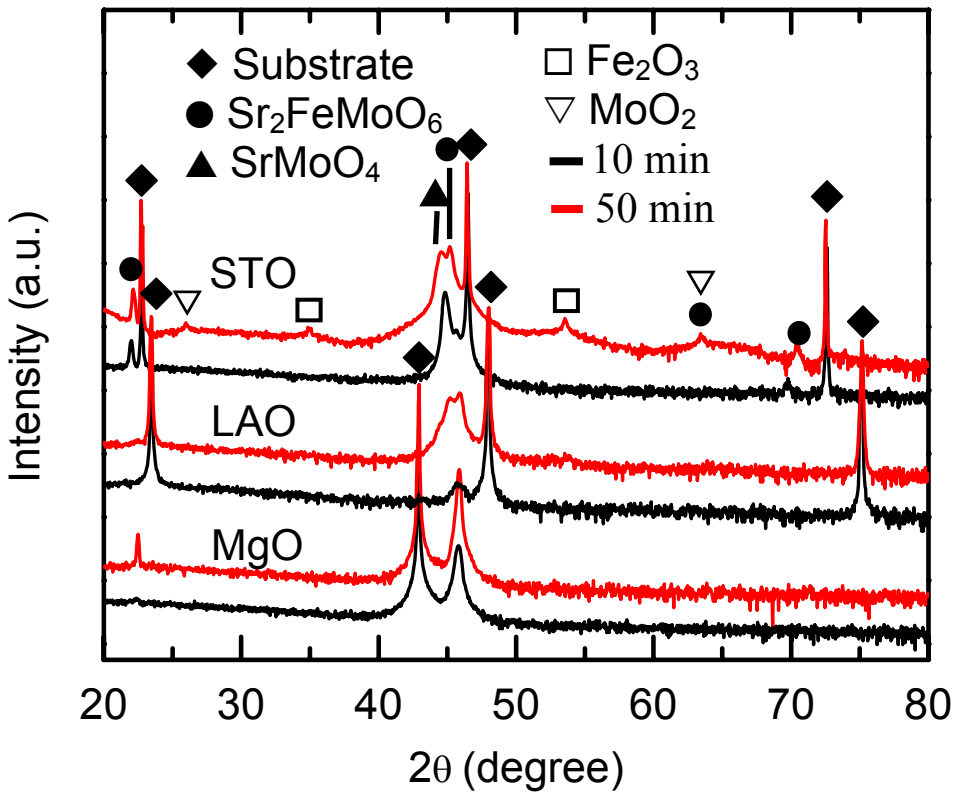

Figure 3-20: (ω–2θ) scan of Sr_2FeMoO_6 films PLD-grown on MgO(001) (bottom), $LaAlO_3$(100)(middle) and $SrTiO_3$(100) (top) in vacuum with a laser fluence of 400 mJ/pulse at temperature of 800°C for 10 min (darker lines) and 50 min (lighter lines). Features corresponding to Sr_2FeMoO_6 (JCPDS 70-4092), $SrMoO_4$ (JCPDS 70-2537), Fe_2O_3 (JCPDS 40-1139), MoO_2 phase (JCPDS 32-0671) and the substrates are identified by solid circles (●), solid triangles (▲), open rectangular (□), open triangles (▽) and solid lozenge (◆), respectively.

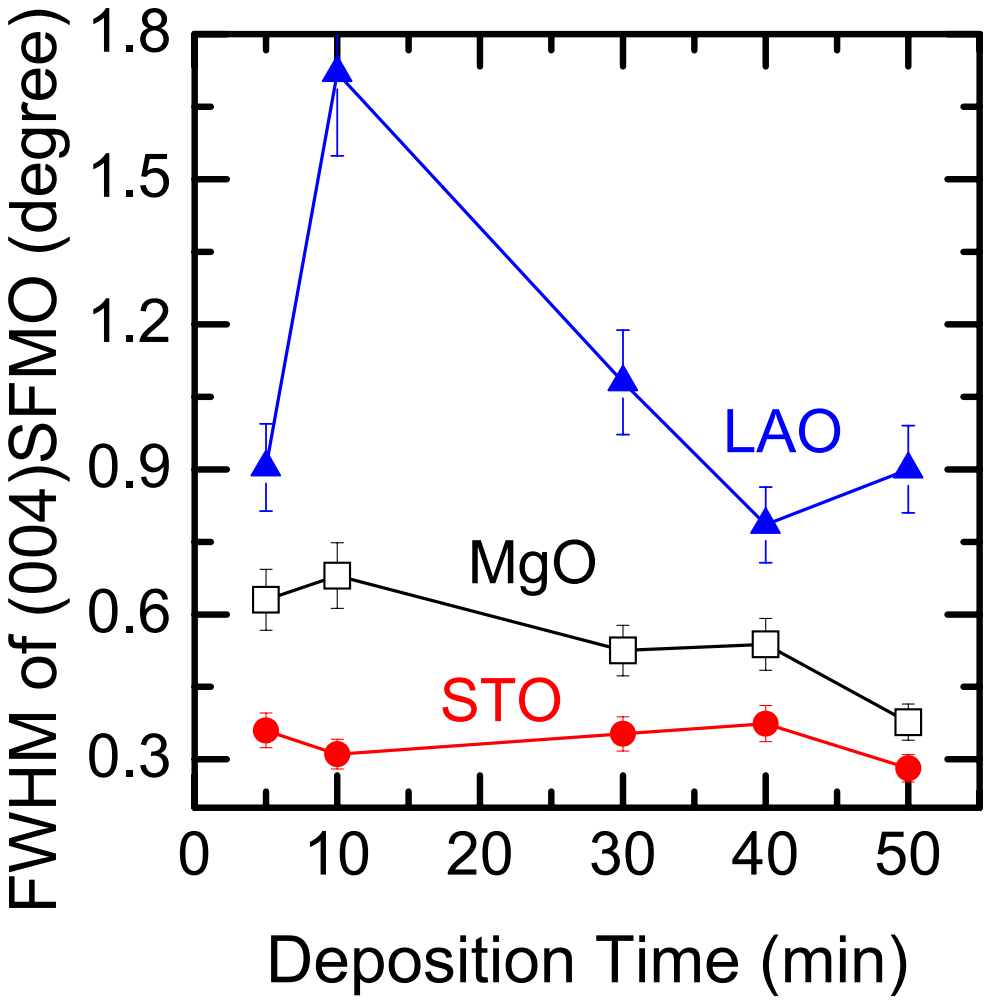

Figure 3-21: FWHM of the SFMO(004) peak in the rocking curve measurement as a function of deposition time for S_2FeMoO_6 films grown on MgO(001) (open squares, □), $SrTiO_3$(100) (solid circles, ●) and $LaAlO_3$(100) (solid triangles, ▲).

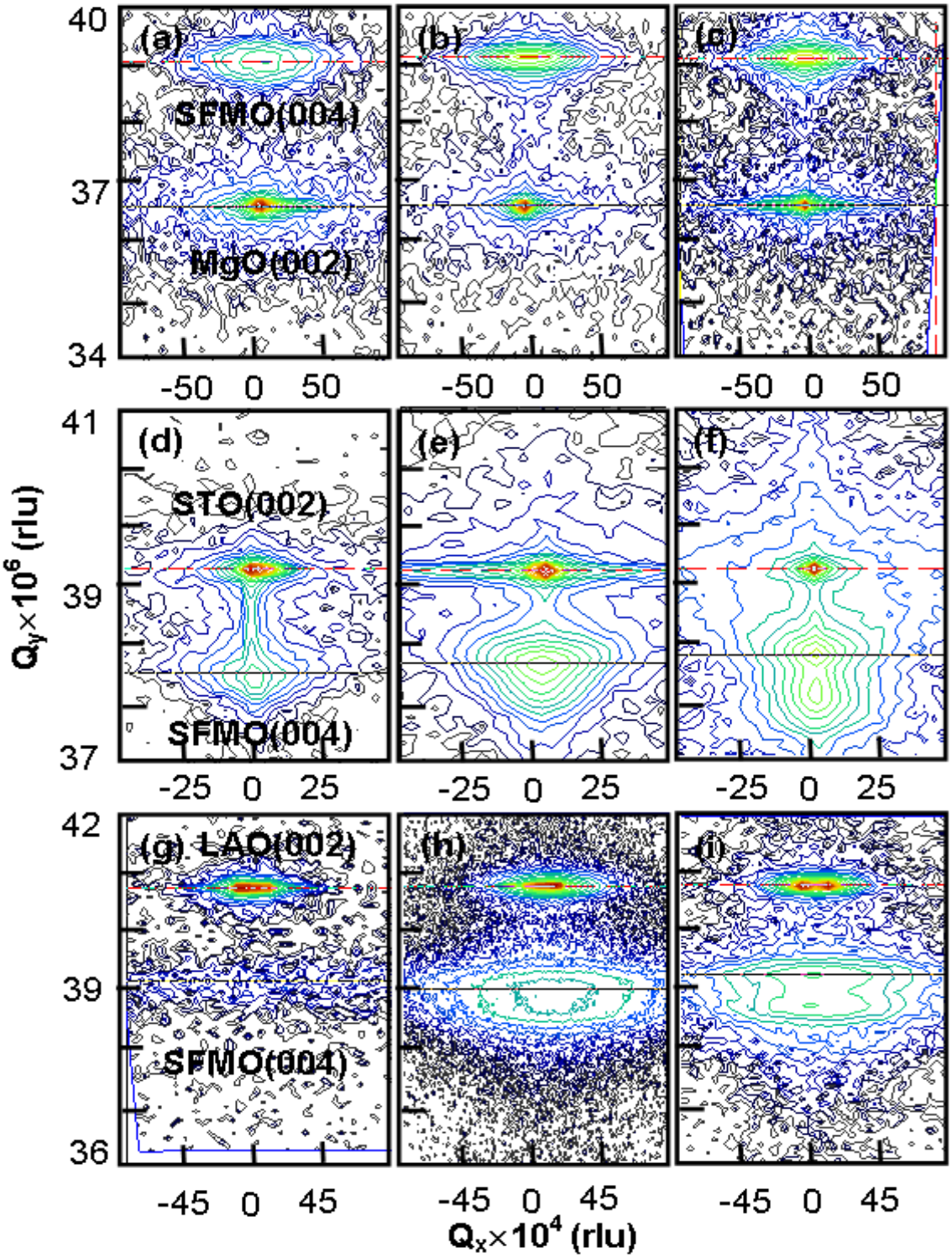

Figure 3-22: Reciprocal space maps of the (004) plane of Sr_2FeMoO_6 films grown on the (002) plane of MgO (top row), $SrTiO_3$ (middle row) and $LaAlO_3$ (bottom row) for deposition of 5 minutes (left column), 30 minutes (centre column) and 50 minutes (right column).

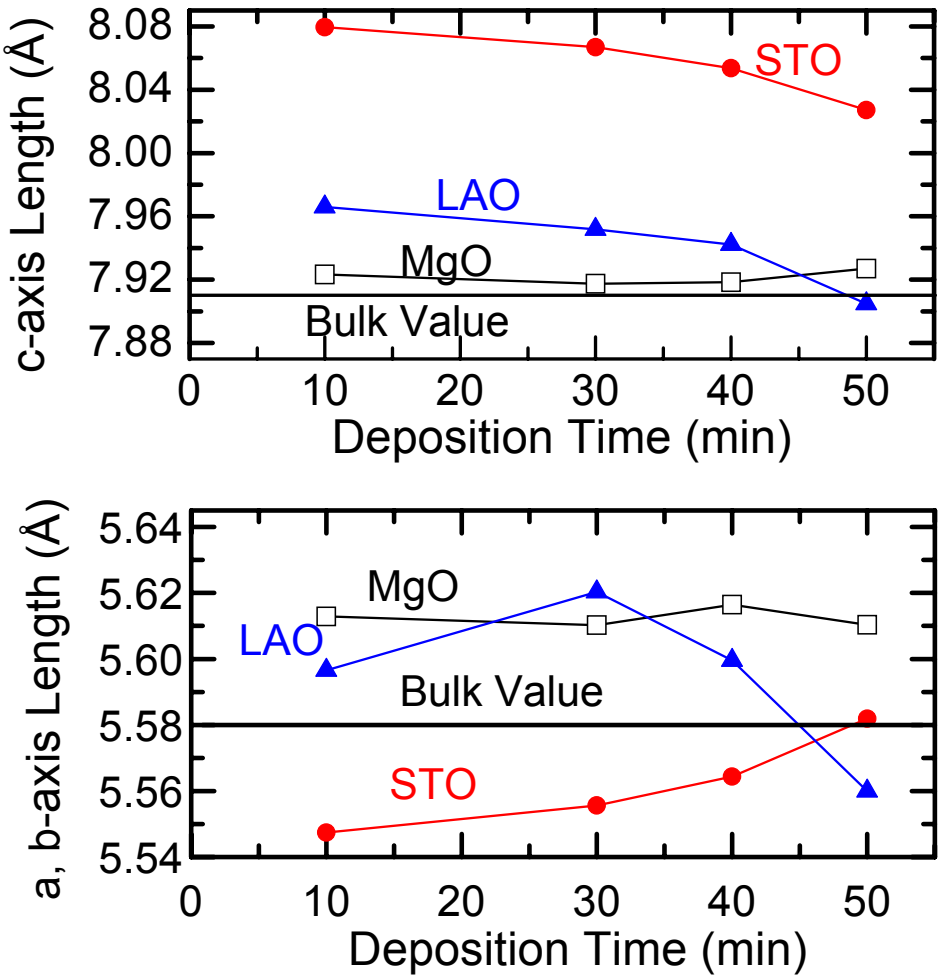

Figure 3-23: c-axis length (top) and a and b-axis lengths (bottom) as a function of deposition time for Sr_2FeMoO_6 films grown on MgO(100) (open squares, □), $SrTiO_3$(100) (solid circles, ●), and $LaAlO_3$(100) (solid triangles, ▲).

3.4.3 Conclusion

Using pulsed laser deposition, we have grown epitaxial SFMO films on three different substrates with different lattice matches: MgO(100) (+6.2%), STO(100) (−1.2%) and LAO(100) (−4.3%). In order to study the effects of strain induced by substrates on the growth evolution of the SFMO films, we have deposited films on all three substrates simultaneously (under the same growth conditions) for different deposition times, corresponding to different film thicknesses of 20 to 200 nm. Using AFM, we observed different evolution of surface morphology with increasing film thickness on the three substrates. In particular, SFMO grown on LAO has the highest number of nucleation sites and three-dimensional growth can be clearly observed from the early stage. For SFMO grown on MgO and STO, even though MgO contains more nucleation sites than STO, the observed growth trends were similar to each other. For both substrates, the SFMO films tend to grow layer by layer in the early stage, with a large number of square terraces forming an epitaxial relationship with the substrate. This initial layer-by-layer growth is followed by spiral growth clusters and three-dimensional growth at longer deposition times.

We also performed high-resolution XRD and reciprocal space mapping measurements, which indicate that the c-axis oriented growth of Sr_2FeMoO_6 films on the three substrates. Rocking curve analysis shows that the SFMO films on STO and LAO have the smallest and largest FWHMs, respectively. Although SFMO and MgO have the largest lattice mismatch, the FWHM of the SFMO film on MgO lies between the STO and LAO values, suggesting a different growth mechanism for the former. While the lattice parameters (a, b, c-axis lengths) of the as-grown SFMO films on STO and LAO are found to converge to the bulk value, reflecting the reduced strain on the as-grown SFMO films, with increasing film thickness, those for SFMO on MgO remain relatively constant. The cell volume for all the films is greater than that determined for bulk SFMO. Interestingly, for films thickness greater than ~120 nm, reciprocal space mapping revealed phase separation on the STO and LAO. The powder XRD measurements showed that a higher deposition time promotes the formation of a parasitic phase (i.e. $SrMoO_4$) on STO and LAO, but not on those grown on MgO substrates. The formation of a second phase may provide strain relief for SFMO films grown on STO and LAO. The present work shows that MgO, despite its large lattice mismatch, appears to be fully relaxed at the early growth stage, therefore offering the best substrate for growing high-quality, epitaxial, single-phase SFMO films.

Chapter 4

Pulsed laser deposition of CrO_2

4.1 Introduction CrO_2

Chromium dioxide is known to be the only ferromagnetic, metallic, binary oxide [112,113], and it has long been a technologically important material, widely used as a particulate recording medium for magnetic tapes. The crystal structure of CrO_2 is shown in Figure 4-1. CrO_2 has a tetragonal structure with lattice parameters of a=b=4.41Å and c=2.91Å. It is ferromagnetic at room temperature, with a Curie temperature at T_C=395 K and a saturation magnetic moment of $2\mu_B$/f.u. [113,114]. In 1986, Schwarz [115] predicted that CrO_2 was half-metallic from density-of-states calculations. A year later, this half-metallic property of CrO_2 was partially confirmed by Kämper et al. [116], who observed nearly 100% spin polarization within 2 eV below the Fermi edge by spin-polarized photoemission. Theoretical calculations and experimental results of other groups also confirmed the highly polarized spin of CrO_2 [117,118,119].

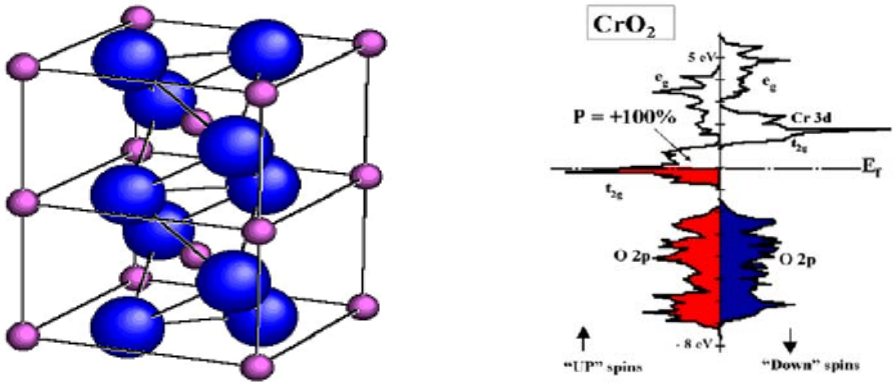

Figure 4-1: Rutile structure of CrO_2 (Left side) and the density of states of CrO_2 Figure adapted from Ref. [120] (Right side).

A schematic diagram of the density of states of CrO_2 is shown in Figure 4-1. The large carrier spin polarization seen in Figure 4-1 could make CrO_2 a very useful electrode for giant magnetoresistant spin valves and spin-dependent tunnel junction devices [112,121,122].

CrO_2 is metastable under ambient conditions and it has a tendency to convert to Cr_2O_3, which is more stable. The phase diagram of CrO_x in high oxygen pressures has been reported previously [123,124] and several different oxidation states can be achieved by varying the oxygen pressure and temperature (Figure 4-2). Some of these chromium oxides have technological applications as catalysts, gas sensors, and as and protective layers for preventing oxidation [125,126,127,128]. The metastable nature of CrO_2 at room temperature makes its synthesis difficult. To date, high quality, single crystal CrO_2 films could only be grown on highly lattice-matched substrates, and by using specialized growth techniques such as high-pressure synthesis [129,130] or atmospheric pressure chemical vapour deposition (CVD) [122,131,132]. For many proposed spintronic devices, multilayer epitaxial films with high quality interfaces are necessary in order to preserve and extract the spin polarization information. Physical vapor deposition (PVD) techniques, such as molecular beam epitaxy (MBE) or pulsed laser deposition (PLD), are commonly used to fabricate multilayer films in-situ and to develop high-quality interfaces in other material systems. Several groups have therefore attempted to prepare CrO_2 films on TiO_2(100), Si(100), Si(111), $LaAlO_3$(100), and Al_2O_3(0001) by using MBE [133,134] and PLD [135,136,137]. Since the most stable chromium oxide phase is Cr_2O_3, these groups have focused on reaching higher oxidation states by either reacting Cr metallic vapour with atomic oxygen in MBE [133] or by using oxygen-rich chromium oxide targets (CrO_3 and Cr_8O_{21}) in PLD [136]. Thus far, these efforts have led to films that either exhibit weak and broad XRD features (indicating poorly aligned crystallites) or contain a mixture of various chromium oxide phases, including Cr_2O_3, CrO_2, and CrO_3. Although successful epitaxial growth of CrO_2 by CVD on MgO(001) and Si(100) has been reported, these groups have used a TiO_2 buffer layer prior to the chromium oxide growth [138,139].

In Section 4.2, we investigate the use of the PLD technique for the growth of a single-phase CrO_x film (particularly CrO_2), with focus on the nature of the resulting nanostructured

films grown on different substrates, including MgO(001), Al_2O_3(0001), $SrTiO_3$ (100), $LaAlO_3$(100), and Si(100). Our goal was to develop a set of optimized growth conditions for producing an epitaxial, single phase (high-quality) film. We systematically varied the substrate temperature, the O_2 pressure, the laser fluence, and the target-to-substrate distance. Unlike the previous PLD studies that did not produce a single-phase CrO_x film [140,141], the present work shows that single-phase CrO_x films could be obtained for the first time on MgO(001) under a narrow set of conditions. In Section 4.3, we focus on the formation of different chromium oxides on MgO (100) substrates and study the surface quality of the sample. In conclusion, we determine the key parameters to produce single phase CrO_2 films by PLD. The key points are to use a compatible substrate (MgO(001)) and sufficient oxygen pressure during growth.

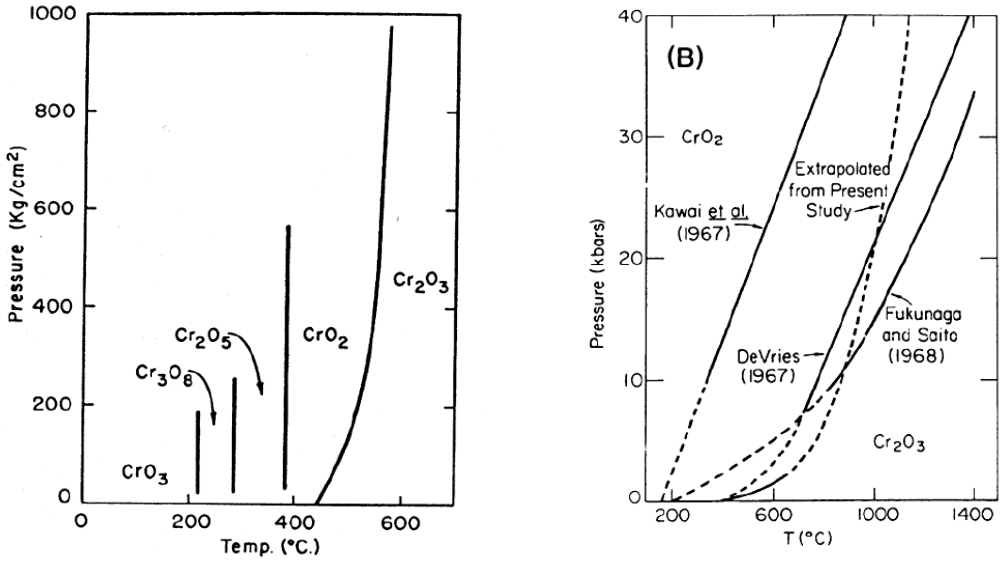

Figure 4-2: Pressure versus temperature phase diagram of CrO_x (a) adapted from Kubota et al. [123] and (b) from Shibasaki et al. [124].

4.2 Pulsed Laser Deposition of Chromium Oxides: Substrate Effects[6]

4.2.1 Experimental details

The PLD experiments were conducted in a turbomolecular-pumped NanoPLD system with a base pressure better than 5×10^{-7} torr. A 248-nm excimer laser with a laser fluence of 350-550 mJ/pulse was used to ablate the Cr metal target (99.95% purity, 1 inch diameter) at a repetition rate of 10 Hz. Oxygen was introduced into the chamber by a variable leak valve to a typical growth pressure of 10-400 mTorr. The use of higher substrate temperature, laser fluence and O_2 pressure is found to be important to achieving a single-phase film. The present system allows for film growth at higher temperatures and higher oxygen pressures than that have been previously attempted [140,141]. The substrates (5×10 mm^2, or 10×10 mm^2) used in the present work were cut from wafers of MgO(001), $SrTiO_3$(100), and $LaAlO_3$(100) substrates, and of Al_2O_3(0001) and Si(100). The morphology and topography of the as-grown films were characterized by using scanning electron microscopy and atomic force microscopy, respectively, while the corresponding crystal structure was analyzed by high-resolution X-ray diffraction.

4.2.2 Results and discussion

4.2.2.1 Morphology

Various growth conditions have been attempted to develop a homogenous, single-phase CrO_x film. Of these experiments, we found that single-phase CrO_x films were more readily obtained at substrate temperature of 480°C, 400 mTorr O_2 pressure and laser fluence of 550 mJ/pulse. Except for the film grown on Si(100) that appears to be silvery black in colour similar to that of bare Si, the resulting films obtained on Al_2O_3(0001), $SrTiO_3$(100), and $LaAlO_3$(100) are brownish in colour while that on MgO(001) appears grayish. Figure 4-3 shows the corresponding SEM images of the as-grown CrO_x films on different substrates

[6] This work has been published in Mater. Res. Proc. Symp. Proc. 998 (2007).

at the aforementioned conditions. Except for the Si(100) sample, silver paste was applied to the side of all of the other (insulating) samples to minimize the effect of charging. For the insulating samples, we show in Figure 4-4 their corresponding AFM images in order to better illustrate their morphologies. Evidently, needle-like nanostructures with an average size of 300 nm (wide) × 1-2 μm (long) and 30-40 nm in height (Figure 4-4a) are found. Furthermore, these needles are distributed in an orthogonal cross pattern (Figure 4-3a, Figure 4-4a), suggesting that these nanostructures are epitaxially grown with respect to the surface registry of the MgO(001) substrate at 400 mTorr O_2 pressure. However, at a lower O_2 pressure of 10 mTorr (Figure 4-4b) and also at 100 mTorr (not shown), the as-grown film appears to be smooth and devoid of nanostructures. It should be noted that the films obtained at a lower O_2 pressure (10 mTorr, 100 mTorr) on MgO(001) are found to be yellow-green in colour. For all other substrates, smooth films decorated with nanoparticles of various sizes and shapes and number densities are observed. In particular, randomly oriented nanoparticles of 10-30 nm in size and nanorods with a typical length of 100 nm are found on Al_2O_3(0001) (Figure 4-3c, Figure 4-4b) and Si(100) (Figure 4-3f). For $SrTiO_3$(100) (Figure 4-3d,Figure 4-4c) and $LaAlO_3$(100) (Figure 4-3e, Figure 4-4d), the nanoparticles are generally less dense, larger (100-300 nm) and irregular in shape.

4.2.2.2 Crystal structure analysis

To further characterize the nature of CrO_x and their crystallinity, we collected high-resolution XRD data for all the samples shown in Figure 4-3. For the Al_2O_3(0001) (Figure 4-3c), $LaAlO_3$(100) (Figure 4-3e), and Si(100) samples (Figure 4-3f), no features other than the substrate peaks are observed, despite the presence of the discernibly visible films on the substrates. This suggests that the as-grown films are amorphous (or extremely thin). For the MgO(001) samples, the corresponding XRD patterns reveal additional features attributable to CrO_2 (Figure 4-5a) and Cr_2O_3 stressed films (Figure 4-5b) grown with O_2 pressures of 400 mTorr and 10 mTorr, respectively. For the sample grown on $SrTiO_3$(100) with 400 mTorr O_2 pressure, weak features attributable to CrO_3 and Cr_3O_4 (Figure 4-5c) are evident. At an

O_2 pressure of 100 mTorr, no Cr related features are observed for the brownish film on the $SrTiO_3$(100) substrate.

In Table 4-1, we show the space group and lattice parameters of the substrates and possible chromium oxide films [142]. Evidently, all three lattice parameters of CrO_2 closely match with those of TiO_2, while all but the c parameter match with those of MgO. The earlier CVD studies on CrO_2 epitaxially grown on TiO_2 [138,143,144] indicate that the as-grown CrO_2 film consists of well-defined needle structures, in close resemblance to the needle structures on MgO shown in Figure 4-3a. The presence of the observed needle structures on MgO in the present case is therefore in accord with the closely matched a and b lattice parameters between CrO_2 and MgO. At the lower O_2 pressure, the formation of Cr_2O_3 is not surprising due to the insufficient amount of oxygen present to allow the stoichiometric formation of CrO_2. The very weak intensity of the Cr_2O_3 feature observed in the XRD pattern (Figure 4-5b, note log scale) suggests that this may be due to randomly aligned crystalline precipitates, as suggested by the nanoparticles observed in the corresponding AFM image (not shown). In the case of $SrTiO_3$, we observe both Cr_3O_4 and CrO_3 peaks, also with very weak intensities.

4.2.3 Conclusions

PLD method was found to be a versatile technique to grow CrO_x nanostructured films using Cr metal as the target on several different substrates, including MgO(001), Al_2O_3(0001), $SrTiO_3$(100), $LaAlO_3$(100), and Si(100). The CrO_x films obtained on most of the substrates are found to be either amorphous [Al_2O_3(0001), $LaAlO_3$(100), and Si(100)] or consisting of more than a single phase [$SrTiO_3$(100)], or both. A single-phase nanostructured film of epitaxially grown CrO_2, decorated with the characteristic needle morphology, was found only on MgO(001). The present work also shows that the use of high O_2 pressure and high laser fluence is essential to the production of these novel needle nanostructures.

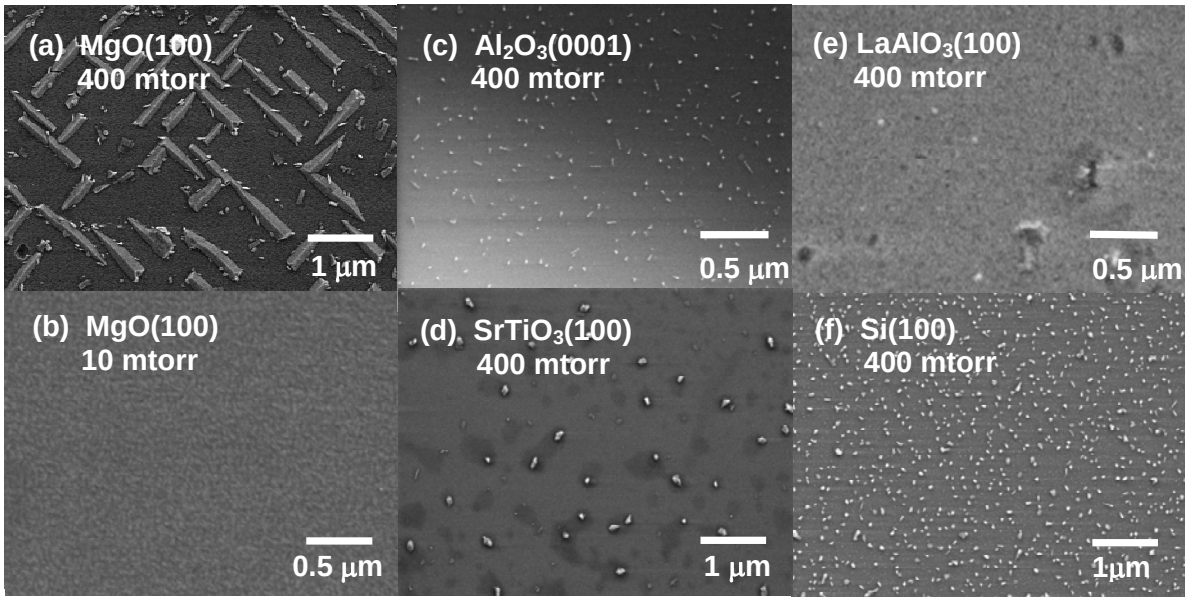

Figure 4-3: SEM images of CrO_x grown on MgO(001) with O_2 pressure of (a) 400 mTorr and (b) 10 mTorr, and on (c) Al_2O_3(0001), (d) $SrTiO_3$(100), (e) $LaAlO_3$(100) and (f) Si(100) with O_2 pressure of 400 mTorr, all at 480°C and with 550 mJ/pulse laser fluence.

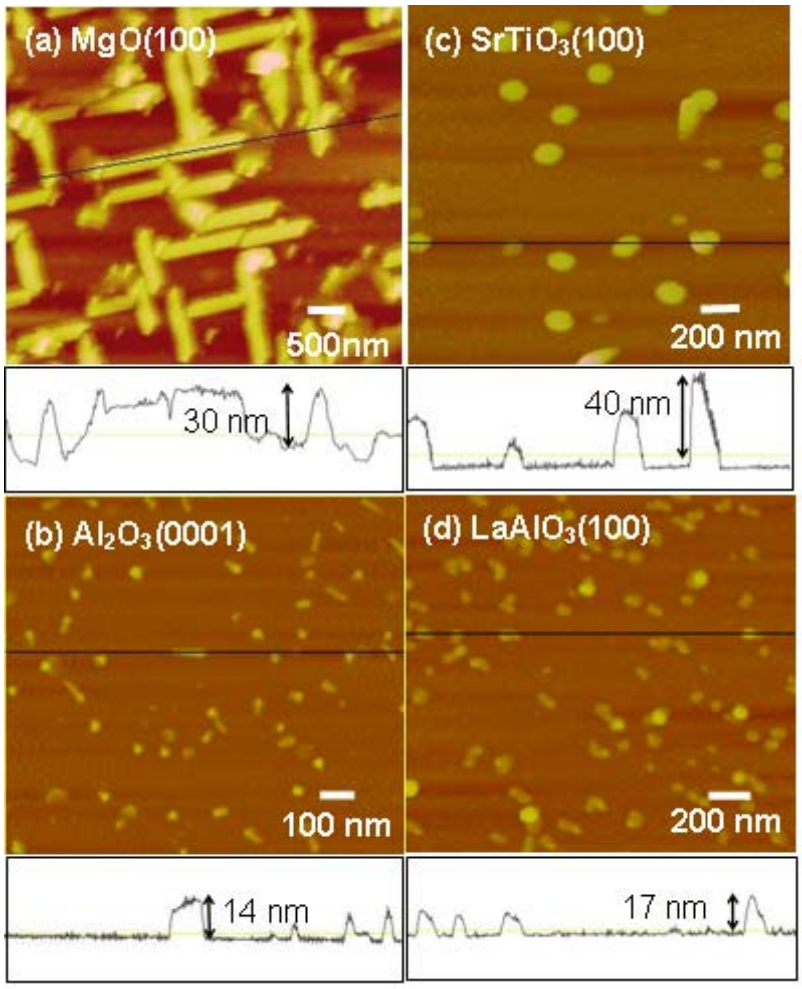

Figure 4-4: AFM images of CrO_x nanostructured films grown on (a) MgO(001), (b) Al_2O_3(0001), (c) $SrTiO_3$(100), and (d) $LaAlO_3$(100) at 480°C with O_2 pressure of 400 mTorr and 550 mJ/pulse laser fluence. The topography line scan of each image is also shown in the panel below the respective AFM image.

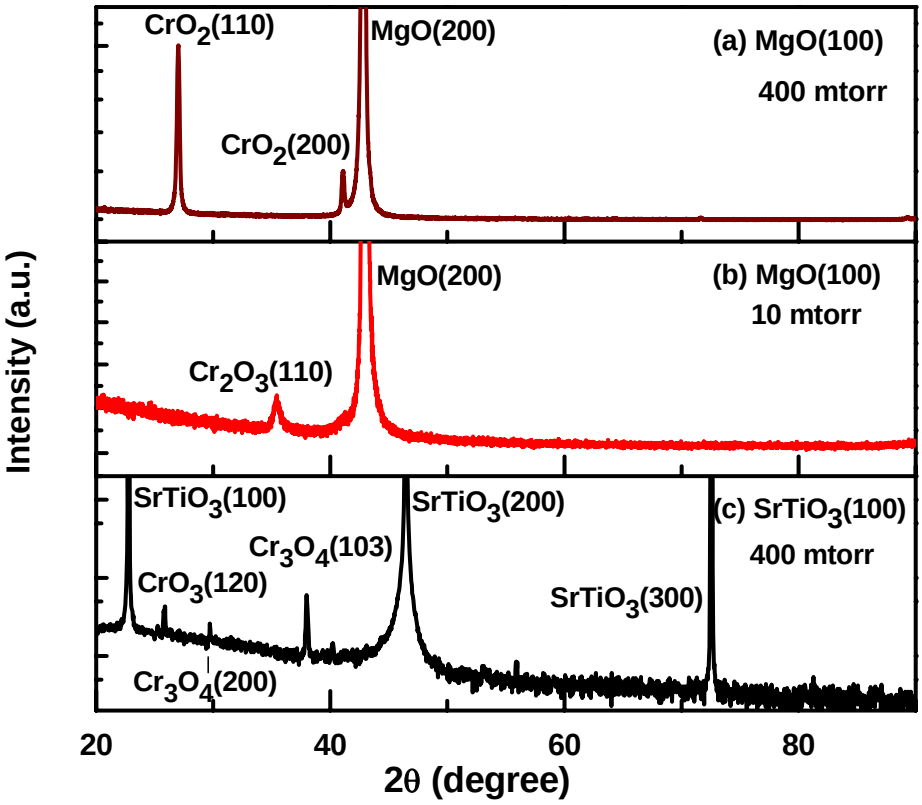

Figure 4-5: (θ–2θ) scan of CrO_x nanostructured films grown on MgO(001) with O_2 pressure of (a) 400 mTorr and (b) 10 mTorr, and on (c) $SrTiO_3$(100) with O_2 pressure of 400 mTorr, all at 480°C and 550 mJ/pulse laser fluence.

Table 4-1: Lattice parameters of selected substrates and chromium oxides.

Material	**Space Group**	**Lattice Parameters**		
		a (Å)	**b (Å)**	**c (Å)**
Cr	Im-3m	2.9	2.9	2.9
Cr_3O_4	141/amd	6.1	6.1	7.5
Cr_2O_3	R-3c	4.9	4.9	13.6
CrO_2	**P42/mnm**	**4.41**	**4.41**	**2.91**
CrO_3	Ama2	5.7	8.5	4.8
TiO_2	**P42/mnm**	**4.59**	**4.59**	**2.95**
MgO	**Fm-3m**	**4.21**	**4.21**	**4.21**
Al_2O_3	R-3c	4.76	4.76	13
$SrTiO_3$	Pm-3m	3.90	3.90	3.90
$LaAlO_3$	R-3m	5.36	5.36	13.11
Si	Fd-3m	5.43	5.43	5.43

4.3 Fabrication of epitaxial CrO_2 nanostructures directly on MgO(001) by Pulsed Laser Deposition[7]

4.3.1 Experimental details

A NanoPLD system with a base pressure better than 5×10^{-7} torr was used for the film growth experiments. The MgO(001) substrates 5×10 mm^2 (or 10×10 mm^2) in size, were mounted on the substrate holder with silver epoxy. Metallic Cr (99.95% purity) was used as the target, with a target-to-substrate distance set to 42 mm. The pressure of O_2 was kept constant between 10 and 900 mTorr by using a mass flow controller during growth, and the substrate temperature during growth could be fixed between 300°C and 780°C by using a temperature controller. The films were grown for 20 minutes, with the laser running at a 10 Hz repetition rate and its fluence typically set at 350-550 mJ/pulse (with the higher laser fluence 550 mJ/pulse producing more crystalline films).

For each growth condition, the morphology of the resulting film was characterized by field-emission scanning electron microscopy (FE-SEM) and atomic force microscopy (AFM), operated in tapping mode. The structure of the film was analysed by using a high-resolution X-ray diffractometer (XRD). The chemical-state composition of the film was studied by using a X-ray photoelectron spectrometer (XPS). The collected XPS data were fitted, where appropriate, with a combination of Gaussian-Lorentzian lineshapes, after correction with the Shirley background by using the CasaXPS software.

4.3.2 Results and Discussion

Since the earlier PLD studies on chromium oxide film growth suggest that a higher oxygen pressure is necessary for CrO_2 growth [135,136,137] we performed the initial PLD

[7] This work has been published in *Applied Physics Letters, 91, 253102* (2007).

growth on MgO(001) with a relatively high O_2 pressure of 400 mTorr but at several substrate temperatures, including 300°C, 400°C, and 480°C. Only the samples grown at 480°C exhibit XRD features that could be attributed to CrO_2, while the other two samples show no XRD peaks. With the substrate temperature held at 480°C, we repeated the growth at different O_2 pressures, including 10 mTorr, 100 mTorr, and 900 mTorr, and the XRD data of the resulting films are shown in Figure 4-6. The samples grown at 10 mTorr and 100 mTorr both appear yellow-green in colour, while the samples obtained at 400 mTorr and 900 mTorr are grey and semi-transparent, respectively.

In addition to the intense MgO(200) substrate feature at $2\theta=42.9°$ found for all the films, the film grown at 10 mTorr exhibits a small peak at $2\theta=35.5°$ that can be attributed to Cr_2O_3(110) (JCPDS 38-1479, Figure 4-6a). This weak feature, together with the lack of other intense peaks typically found in the Cr_2O_3 powder pattern (i.e. Cr_2O_3(104), Cr_2O_3(116)) suggest a poorly crystalline film. The yellow-green color of the film is also typical of Cr_2O_3. On the other hand, no XRD peak was observed for the other yellow-green film grown at 100 mTorr (Figure 4-6b), which suggests an amorphous Cr_2O_3 film. For the semi-transparent film grown at 900 mTorr O_2 pressure, the very weak peak observed at $2\theta = 31.1°$ can be assigned to CrO_3(200) (JCPDS 32-0285, Figure 4-6d).

For the grey sample grown at 400 mTorr, there are two strong XRD peaks that could be attributed to the film (Figure 4-6c). We assign the peaks at $2\theta=27.1°$ and $2\theta=41.2°$ to CrO_2(110) and CrO_2(200), respectively, according to the powder XRD pattern (JCPDS 9-0332), which, however, shows that the CrO_2(110) peak is the most intense while the CrO_2(200) feature has a relative intensity of only 8%. Other intense peaks, including the CrO_2(101) and CrO_2(211), in the powder pattern are not observed in the present work (Figure 4-6). This data suggests that the as-grown film consists of CrO_2 crystallites with two possible epitaxial relationships with the MgO(001) surface: CrO_2(110) || MgO(001), and CrO_2(200) || MgO(001). From the relative intensities of the two CrO_2 peaks, we estimate that significantly more crystallites are oriented with CrO_2(200) || MgO(001). Furthermore, the CrO_2(110) peak is found to be shifted from the powder value reported in the literature (JCPDS 9-0332), consistent with a 4.8% expansion of the lattice of the as-grown film. The

CrO_2(200) peak is also slightly shifted from the powder value, consistent with a 0.7% compression of the lattice.

Of the large number of possible chromium oxides, few have diffraction peaks near the positions that we observe for the film grown at 400 mTorr (Figure 4-6c). The closest alternative assignment for the peak at 2θ=27.1° would be $Cr_2O_5(\bar{2}\,2\,1)$ (JCPDS 36-1329). However, the corresponding Cr 2p XPS envelope is found to consist of a single peak (shown below), in marked contrast to the Cr_2O_5 envelope reported in the literature [145]. The observed differences in our XPS result can therefore be used to rule out the formation of Cr_2O_5 in the present work.

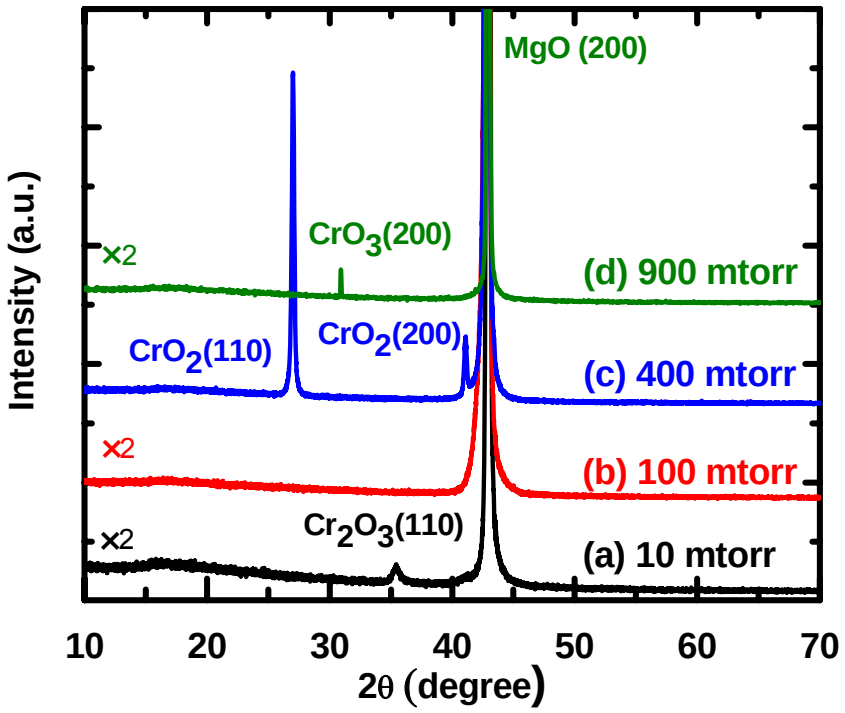

Figure 4-6: 2θ–ω XRD spectra for the CrO_x films grown on MgO(001) substrates at O_2 pressure of 10, 100, 400 and 900 mTorr. The intense feature at 2θ=42.9° corresponds to the MgO(200) substrate peak.

The corresponding SEM images for the CrO_2 film grown on MgO(001) at 400 mTorr (Figure 4-6c) are shown in Figure 4-7 Needle-like nanostructures (Figure 4-6a) with an

average size of 300 nm (wide) × 1-2 μm (long) and 30-40 nm in height are found mostly near the edges and corners of the sample. These needles are distributed in an orthogonal cross pattern, suggesting that these nanostructures are epitaxially grown with respect to the surface registry of the MgO(001) substrate. For the rest of the sample, we observe micropallet structures with a rectangular footprint, with an average edge size of 0.6-1.2 μm and height of 30-50 nm (Figure 4-7b). The heights of these nanostructures are obtained from AFM measurements (not shown). Needle structures similar to those shown in Figure 4-6 are also found at the edges of some of the micropallets. While these morphological features are highly reproducible in the films grown at 480°C and 400 mTorr O_2 pressure on the MgO(001) substrate, they were not observed on films grown under similar conditions on other substrates, including $LaAlO_3$(100), Al_2O_3(100), $SrTiO_3$(100) and Si(100) [146]. Given that the a and b lattice parameters for MgO (a=b=c= 4.21 Å) are similar to those of CrO_2 (a=b=4.41 Å, c=2.91 Å), this result suggests that lattice matching is important for obtaining a highly oriented CrO_2 film.

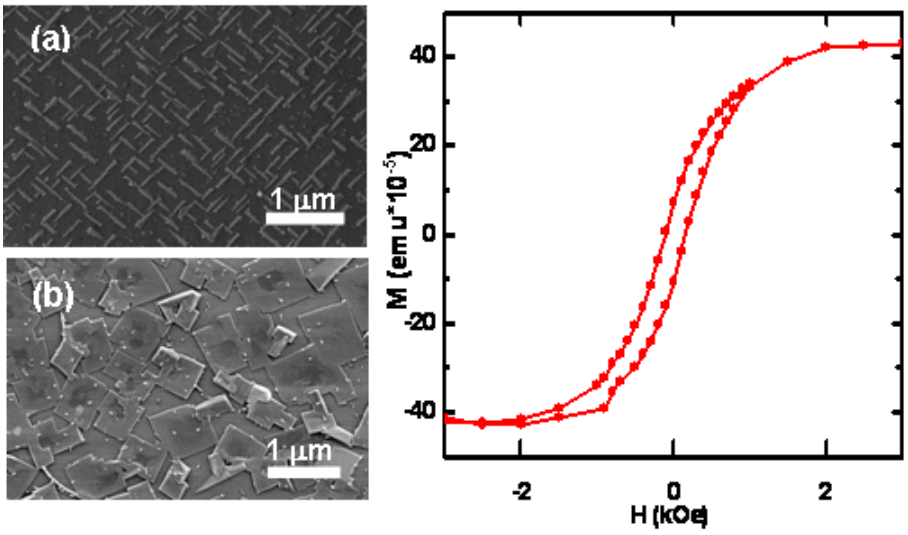

Figure 4-7: SEM images of a CrO_2 film grown at 480°C with 400 mTorr O_2 pressure, depicting both (a) nanoneedles near the edges and corners of the sample, and (b) plates near the film center. (c) shows the magnetization (M) vs field (H) curve at 5 K, with H parallel to the film surface. The paramagnetic contribution has been subtracted from the curve.

Figure 4-8 shows the Cr 2p and O 1s XPS spectra for the center region of the CrO_2 film grown on MgO(001) at 480°C with 400 mTorr O_2 pressure and as a function of sputtering depth. For the as-grown film, the Cr $2p_{3/2}$ ($2p_{1/2}$) envelope (Figure 4-8a) can be fitted to two components at 576.6 eV (586.4 eV) and 579.3 eV (588.5 eV) corresponding to CrO_2 and CrO_3, respectively [147,148]. The binding energy location of Cr $2p_{3/2}$ for the Cr(IV) state observed in the present work is in general accord with the earlier results [149,150]. In particular, Bullen and Garrett [147] observed the CrO_2 $2p_{3/2}$ feature at 576.4 eV for the CrO_2 powder and that at 576.6 eV for a 850-nm thick CrO_2 film grown on TiO_2 by CVD. Brand et al. [151] reported a Cr $2p_{3/2}$ feature at 577 eV for their 21-nm thick CrO_2 film also grown on TiO_2 by CVD. Furthermore, Liu et al. [148] found the Cr $2p_{3/2}$ peak for bulk CrO_3 located at 579.2 eV, which is in good agreement with the weaker feature in the present work. The presence of CrO_3 is expected due to the conversion of CrO_2 to CrO_3 under a high O_2 pressure in the chamber. Upon sputtering to 160 s, the Cr $2p_{3/2}$ ($2p_{1/2}$) feature at 579.3 eV (588.5 eV) for CrO_3 is diminished while the corresponding CrO_2 feature at 576.6 eV (586.4 eV) strengthens. Further sputtering completely removes the CrO_3 peak, leaving behind only an intense CrO_2 feature. The observed spectral evolution upon sputtering therefore suggests that the film consists primarily of CrO_2, covered by a thin CrO_3 overlayer. The Cr 2p intensities of the CrO_2 features appear to reach a maximum after 330 s sputtering and then decrease upon further sputtering, consistent with a relatively thin film (<50 nm) as illustrated by the AFM images (not shown). It should be noted that despite using Cr metal as our target for growing the present film, no Cr $2p_{3/2}$ features for metallic Cr located at 574.2 eV [152] are detected, even after sputtering for 500 s. Because the sputtered chromium feature can be fitted to a single peak, it is unlikely that the film contains other chromium oxide phases than CrO_2.

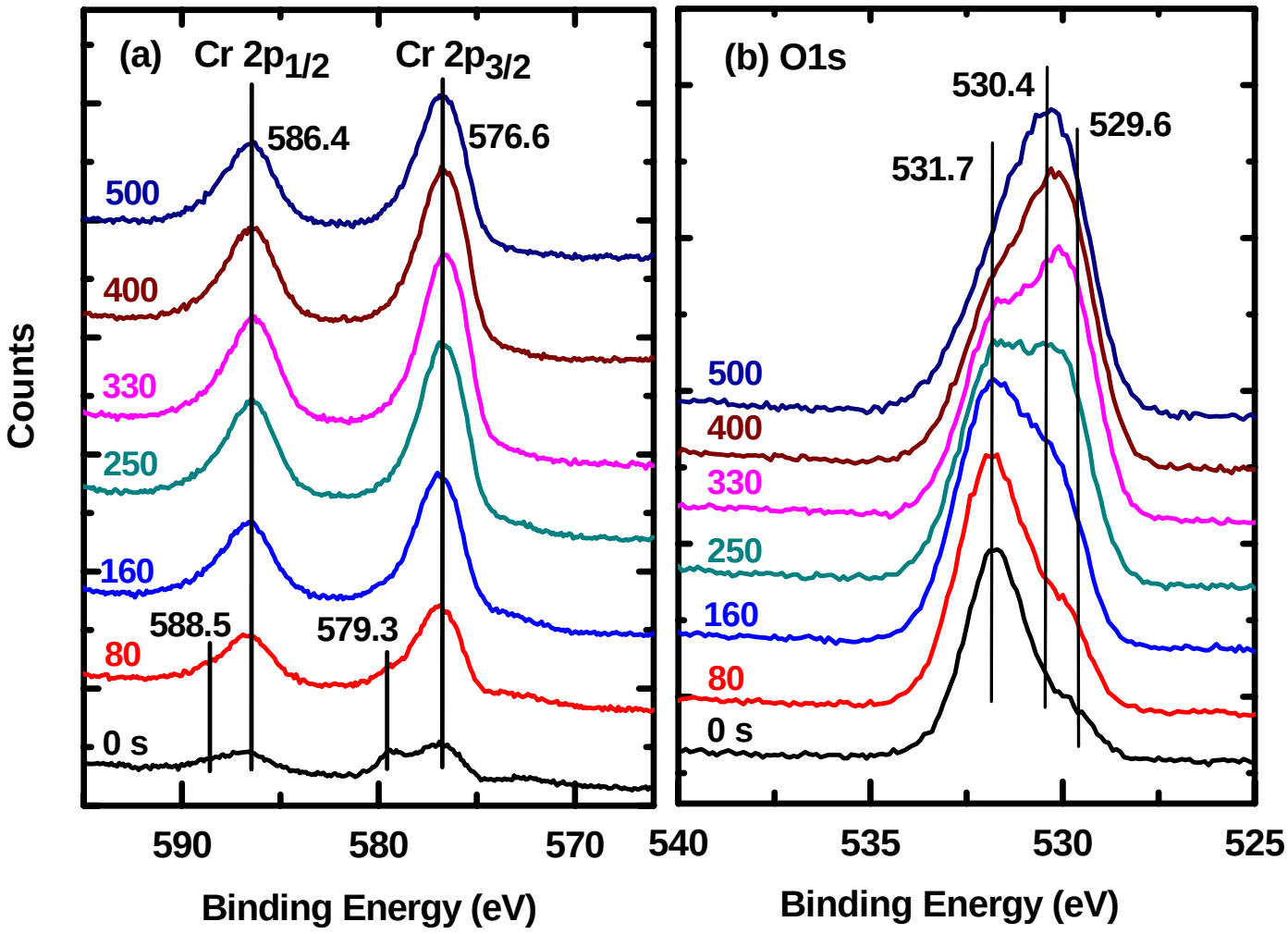

Figure 4-8: XPS spectra of (a) Cr 2p and (b) O 1s regions of a chromium oxide film as grown on MgO(001) at 480° C with 400 mTorr O_2 pressure and upon sputtering for 80, 160, 250, 330, 400 and 500 s.

4.3.3 Conclusions

Using pulsed laser ablation, we have grown CrO_2 films directly on MgO(001) substrates with a metallic Cr target in an O_2 environment. The films were characterized by XRD, SEM, AFM, and XPS. In a limited set of growth conditions (550 mJ/pulse laser fluence, 480°C substrate temperature and 400 mTorr O_2 pressure), we were able to reproducibly grow very thin single phase CrO_2 films (~50 nm thick) by PLD, as shown by our XRD and XPS data. To our knowledge, this is the first demonstration that single-phase CrO_2 can be produced directly using a physical vapor deposition method. This was possible likely because of the high laser fluence and high oxygen pressures used. With further optimization, it should be possible to use the PLD method to produce high quality single crystal CrO_2 films as part of the multilayer structure appropriate for spintronic applications.

Chapter 5
Concluding remarks and outlook for future work

Pulsed laser deposition has been used to grow two particular half-metallic oxide films (Sr_2FeMoO_6 and CrO_2) on different substrates. Effects of the growth parameters and lattice mismatch on the crystal and surface quality of these films have been studied. For applications in the microelectronic industry, silicon is the most widely used and desirable substrate for fabricating integrated devices. Despite the large amount of work that has been done to grow Sr_2FeMoO_6 on different substrates, no-one has to date reported successful single-phase growth of Sr_2FeMoO_6 on Si. In Section 3.2, succesful deposition of Sr_2FeMoO_6 on Si(100) substrate under different growth temperatures and deposition times has been disscussed. In contrast to earlier work on other substrates (typically grown at temperatures ranging from 800°C-1100°C), nanocrystalline, single-phase Sr_2FeMoO_6 films were obtained at a low growth temperature of 600°C. Lower growth temperatures are more desirable from an industrial point of view. Under optimized growth conditions, these Sr_2FeMoO_6 films were high quality with saturation magnetic moments (3.4 μ_B per formula unit (or /f.u.) at 77 K), and they are comparable to the best Sr_2FeMoO_6 films epitaxially grown on lattice-matched substrates (such as $SrTiO_3$ and MgO) reported to date. As revealed by MFM, the as-grown Sr_2FeMoO_6 films on Si also exhibit micrometer-sized magnetic domains at room temperature, which are signficantly larger than the crystalline grain size (200-250 nm) indicating that the Sr_2FeMoO_6 grains are well connected electromagnetically. In order to better understand the growth mechanism of these polycrystalline films, several Sr_2FeMoO_6 on Si films of different thicknesses were grown and the crystal structures of these films were probed as a function of depth using GIXRD. These X-ray diffraction measurements were carried out where the incident angle of the X-ray beam was changed. Surprisingly, for as-grown Sr_2FeMoO_6 films thicker than 60 nm, a preferential orientation of the nanocrystals in the film is observed. The mechanism for the preferential oriented growth on Si, despite the lack of lattice matching, is related to the substrate-to-target distance as shown in Section

3.2.4. While it is not clear how this oriented growth may occur, it is plausible that the incident plume from the target resputters some of the Sr_2FeMoO_6 from the substrate, and this re-sputtering depends on the Sr_2FeMoO_6 crystallite orientation. This is similar to the well known IBAD (ion beam assisted deposition) process [153]. This type of oriented growth has a lot of technological potential, as lattice-matched epitaxial crystal growth is expensive and difficult for industrial applications that may take advantage of single crystal functionality.

In the second part (Sections 3.3 and 3.4) of the project, epitaxially grown films were the focus of this research. Using pulsed laser deposition, the Sr_2FeMoO_6 films epitaxially grown on MgO(001), $SrTiO_3$(100) and $LaAlO_3$(100). The effects of the growth parameters have been studied and optimum growth conditions have been obtained. High resolution X-ray diffraction studies revealed the single-phase Sr_2FeMoO_6 material can be epitaxially grown on the MgO even at temperature as low as 600°C. However, higher deposition temperature (800°C) can improve the crystal quality (Section 3.3). The film grown at 800°C was annealed in oxygen, producing epitaxial $SrMoO_4$ overlayer on the Sr_2FeMoO_6 film. The corresponding magnetization data showed that the post annealing treatment lowered the saturation magnetic moment from 3.4 μ_B/f.u. for as-grown Sr_2FeMoO_6 film to 1.4 μ_B/f.u. after annealing, but the coercive field remains the same for both films. To study chemical-state composition of the near-surface region, depth-profiling X-ray photoemission of the valence-band and core shells of O 1s, Sr 3d, Fe 2p and Mo 3d regions has been conducted on the Sr_2FeMoO_6 films, before and after annealing. In core-shell spectra, similar features have been observed for both as-grown and post-annealed samples before sputtering. These results suggest that $SrMoO_4$ is a stable phase and it readily forms on the surface, which is an important consideration for multilayered device fabrication. Furthermore, depth profile XPS reveal that the intensity ratios of the 3d features of Mo^{4+}, Mo^{5+}, and Mo^{6+} for Sr_2FeMoO_6 (before and after annealing) remain unchanged with sputtering depth (after 160 s). This XPS result, combined with magnetization data indicates that post-annealing in O_2 has no notable effect on the grain formation in the bulk and the observed secondary phase ($SrMoO_4$) is formed predominantly on the surface. This overlayer effect can be responsible for the observed reduction in the saturation magnetic moment.

In Section 3.4, in order to study the effects of strain induced by the substrates on the growth evolution of the Sr_2FeMoO_6 films, films were deposited for different time intervals of (5, 10, 30, 40 and 50 minutes). Substrates of MgO(001), $SrTiO_3$(100) and LAO(100) with lattice mismatch of 6.2%, -0.9 %, and -4.1 %, respectively, have been studied for this section. Surface morphology, grain size, film epitaxy, and crystal quality were determined by atomic force microscopy, X-ray diffraction, and reciprocal space mapping, and all these parameters have been studied as a function of deposition time. Different types of growth were observed. On $SrTiO_3$, Sr_2FeMoO_6 tends to grow layer by layer in the early stage, and then become more 3D for thicker films. On MgO, layer by layer growth is also observed, but there are more nucleation sites, and more 3D growth. On $LaAlO_3$, 3D growth was observed for all film thicknesses. In agreement with earlier work, the FWHM of (004) plane of Sr_2FeMoO_6 on $SrTiO_3$ (for the films thinner than ~120 nm) had the narrowest width, showing the higher crystal quality, which is expected due to the least lattice mismatch of the substrate and film. However, interestingly, for films thicker than ~120 nm, reciprocal space mapping revealed Sr_2FeMoO_6 phase separation on the $SrTiO_3$ and $LaAlO_3$. High resolution X-ray diffraction studies showed that the parasitic phase, including $SrMoO_4$ and Fe_2O_3, that forms in thicker films grown on $SrTiO_3$ and $LaAlO_3$ substrates, but not on those grown on MgO substrates. As is shown by the reciprocal space mapping, the formation of the secondary phase helps the Sr_2FeMoO_6 films to release the stress originated from the lattice mismatch with the substrates. Although MgO has the largest mismatch with the Sr_2FeMoO_6 films the surface energy and nature of the chemical bonding of the Sr_2FeMoO_6 and MgO most probably prevent the phase separation.

As the results of Sections 3.3 and 3.4 show, MgO is the most promising candidate substrate for Sr_2FeMoO_6 because of the low strain in the as-grown films, highly crystalline film grown (with sharp rocking curves), wide temperature range 600-850ºC for good growth, lack of phase separation, and high saturation magnetic moments. Moreover, MgO is non-magnetic and therefore will not introduce any magnetic signature to the deposited film and it can be used as an inert support for constructing devices.

On a separate project, studying the growth parameters for the formation of CrO_2 was the focus of the research. To our knowledge, this is the first demonstration that single-phase CrO_2 can be produced directly using a physical vapor deposition method. In order to study the effect of the substrates on the growth of CrO_2, several different substrates were used, including MgO(001), Al_2O_3(0001), $SrTiO_3$(100), $LaAlO_3$(100), and Si(100). Chromium metal has been used as a target, and considering Cr_2O_3 is the most stable phase, oxidizing the ablated Cr to the right oxidation state of +4 was quite challenging. Systematic studies of different growth conditions showed that the deposition of CrO_2 was possible in a narrow window of growth temperature of 480 ºC, oxygen pressure of 400 mTorr, and high laser power of 550 mJ/ pulse. The CrO_x films obtained on most of the substrates were found to be either amorphous [Al_2O_3(0001), $LaAlO_3$(100), and Si(100)] or consisting of more than a single phase [$SrTiO_3$(100)], or both. A single-phase nanostructured film of epitaxially grown CrO_2, decorated with a characteristic needle morphology, was found only on MgO(001). Morphology, crystal and electronic structure of all the films were characterized by XRD, AFM, SEM and XPS.

Future plan

Magnetic tunnel junctions are a prototypical spintronic device and it consists of two magnetic layers sandwiching a very thin insulating layer (Section 1.2.3). It has been shown that [19] magnetic tunnel junctions with ferromagnetic metal (Fe, Cr) layers work well at room temperature. Given the fact that oxides materials are generally multifunctional materials and they may have better high temperature properties and higher spin polarization, therefore replacing ferromagnetic metals layers with ferromagnetic oxide layers may improve performance of this magnetic tunnel junctions. There have been a few groups, including Asano et al. [154], Bibes et al. [155] and Fix et al. [156], who have fabricated the magnetic junction. However, the formation of secondary phases on the surface was always a problem and it lowered the efficiency of the system. It is also worth mentioning that all these oxide magnetic tunnel junctions have been grown on $SrTiO_3$ substrates. This thesis shows that in order to minimize the amount of secondary phase on the surface, a high vacuum during the

growth is one of the key requirements which makes in-situ fabrication the only way to grow multilayer films. Furthermore, all the relevant work in this thesis [Sections 3.3, 3.4, Appendix C] has shown that MgO is a better and more reliable substrate to grow Sr_2FeMoO_6 . Fabricating magnetic tunnel junctions of Sr_2FeMoO_6 has been attempted here, and the preliminary result are promising (Figure 5-1, Figure 5-2). These magnetic tunnel junctions consisted of four layers of Sr_2FeMoO_6 (15 nm)/MgO(5 nm)/Sr_2FeMoO_6 (20 nm)/Au(1nm). The HRXRD (Figure 5-1) and reciprocal space mapping (Figure 5-2) show that the whole stack was epitaxial. The well-defined fringes in the X-ray reflectivity data indicates the sharp interface between layers (Figure 5-2). Since the efficiency of the magnetic tunnel junctions depends on the thickness of the layers, especially the barrier layer, finding the optimum thickness of the barrier in this structure could be worth while study.

Another project that can be done regarding Sr_2FeMoO_6 films is using Si substrates for epitaxial growth. This possibly can be done by using buffer layers of MgO and $SrTiO_3$ because of their good lattice match with the Sr_2FeMoO_6 films.

For the CrO_2 project, although we have been able to grow epitaxial CrO_2 on MgO, the morphology analysis of the surface indicated that CrO_2 is not a continuous film. Further optimization of the growth parameters may produce more uniform, continuous films.

Finally, more detailed magnetic studies of these high quality Sr_2FeMoO_6 films. In particular, by applying the magnetic field in parallel and perpendicular direction with respect to the Sr_2FeMoO_6 c-axis at different temperatures, one can gain insight into how the various defects (parasitic phases, strain and grain boundaries) influence the magnetic properties, therefore allowing one to tailor these materials for spintronics applications.

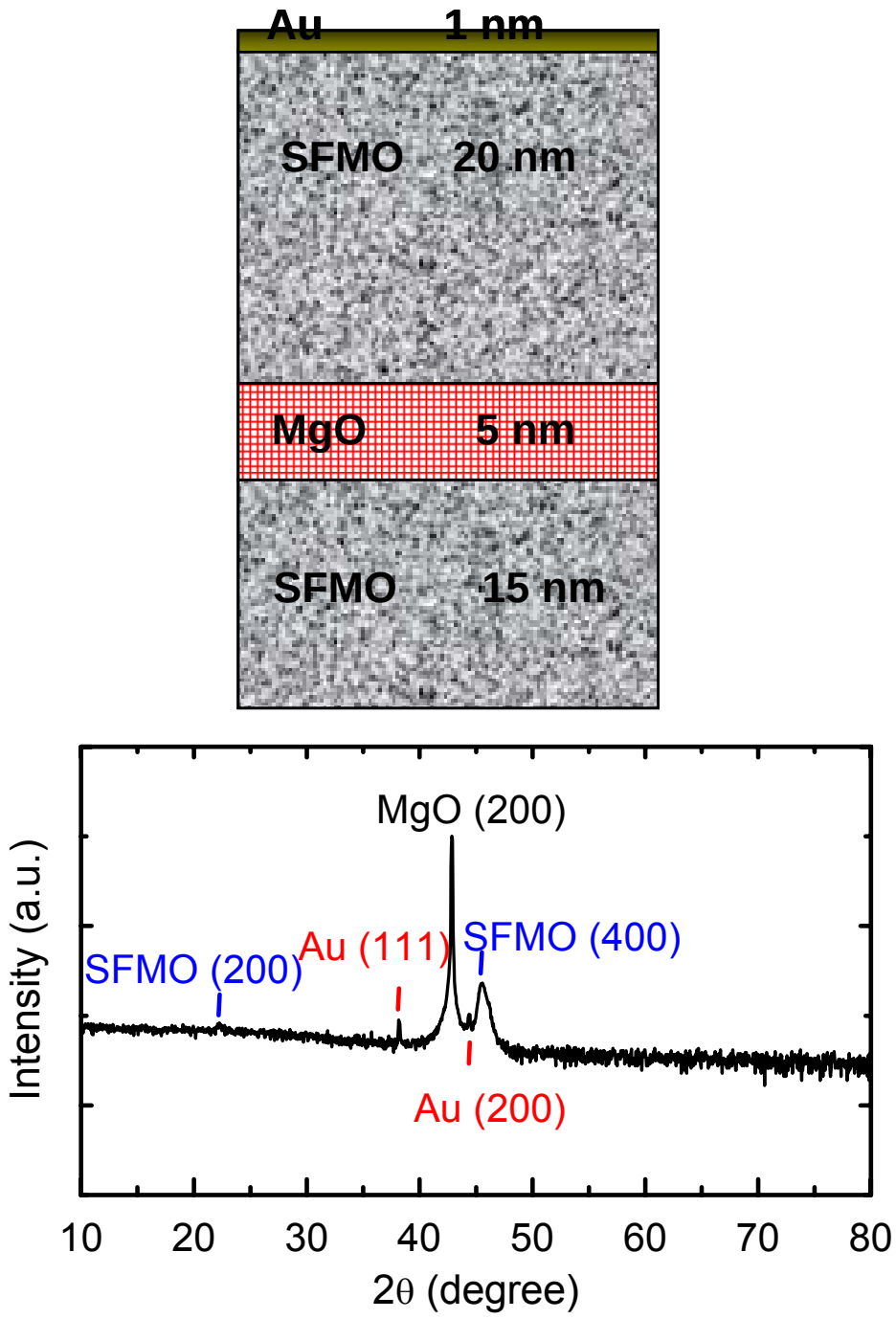

Figure 5-1: Schematic plot of the multilayer stack of Sr_2FeMoO_6 /MgO/Sr_2FeMoO_6 /Au with their respective thickness (top figure).HRXRD of the multilayer film of MgO/Sr_2FeMoO_6 /MgO/Sr_2FeMoO_6 /Au (bottom figure), y-axis shows the logarithmic scale of the intensity of the peaks.

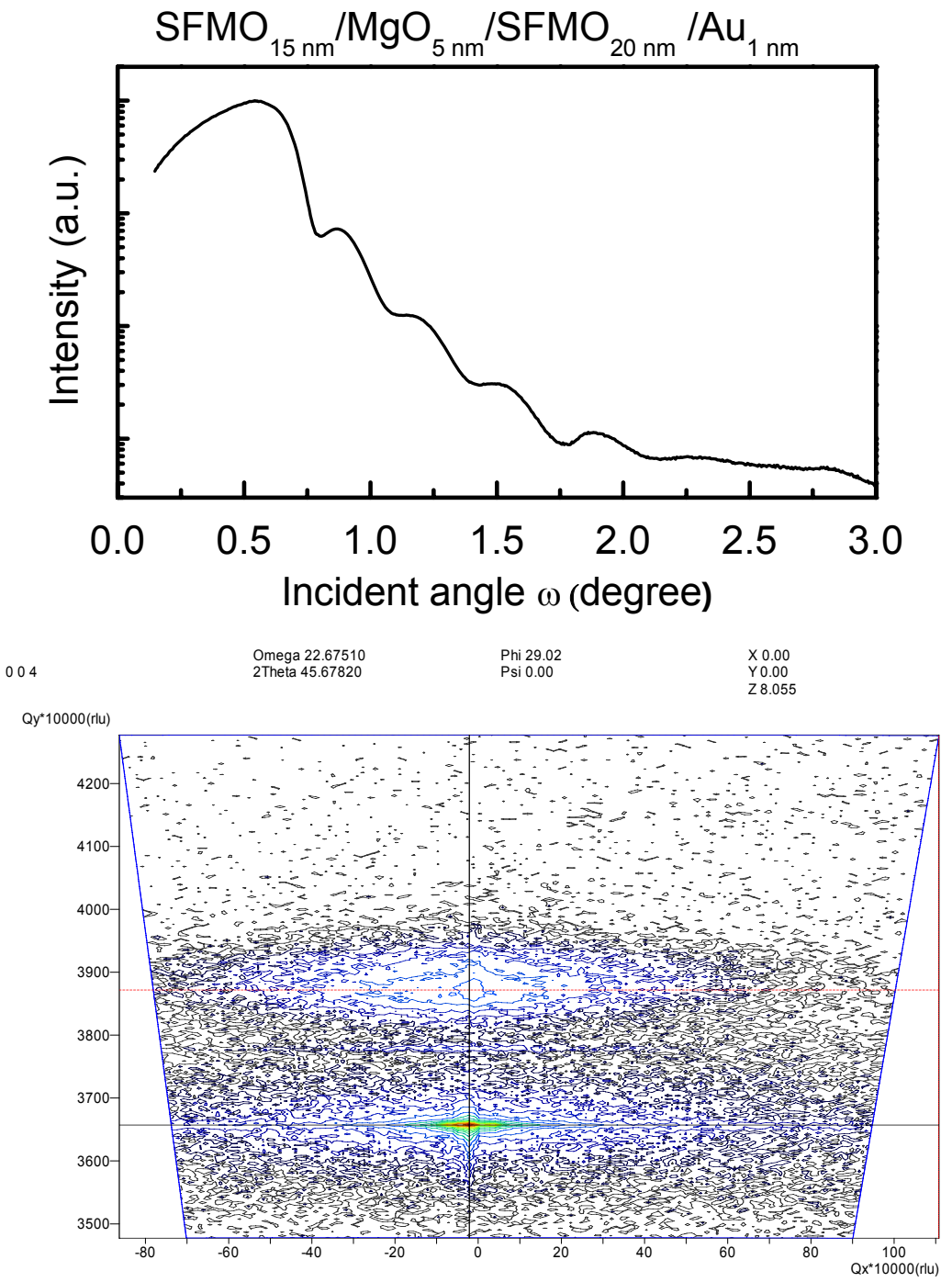

Figure 5-2: X-ray reflectivity of the multilayer films. Well defined fringes show the sharp interface between layers (left figure). Reciprocal space mapping of the Multilayer film, epitaxially grown Sr_2FeMoO_6 and Gold on the MgO substrate.

Appendix A

Effects of laser power

In order to find the optimum growth conditions for Sr_2FeMoO_6, the effects of applying different laser powers of 300 mJ/Pulse, 400 mJ/Pulse and 500 mJ/pulse during the growth process have also been studied. Figure 5-3 shows the ω–2θ XRD scans for the Sr_2FeMoO_6 films grown on MgO(001) with laser power of 300 mJ/Pulse, 400 mJ/Pulse and 500 mJ/pulse at 600°C. The HRXRD shows epitaxially grown Sr_2FeMoO_6(002) on MgO (100) for all laser powers. However, for the highest laser power of 500 mJ/Pulse, a well defined peak due to diffraction from the (112) plane of Sr_2FeMoO_6 can be seen. It should be noted that, this peak has the highest intensity in the diffraction pattern PDF file, suggesting that by applying higher laser power, the thermodynamics of the system changed and the deposited atoms have higher energy to overcome the surface registry. The φ-scan of the optimally grown films shows the 4-fold symmetry. Interestingly, the XRD results of the Sr_2FeMoO_6 films grown at a higher laser power show the emergence of a second set of 4-fold symmetric peaks, which indicates that the higher laser power promotes the growth of two different crystal orientation.

For the Sr_2FeMoO_6 samples grown on Si(100), applying different laser powers also had some interesting results. As was discussed in Section 3.2, using the Si(100) substrate and laser power of 400 mJ/pulse results in formation of polycrystalline Sr_2FeMoO_6, and the optimum growth temperature was found to be 600°C. Applying higher laser power had two significant effects on Sr_2FeMoO_6 films grown on Si. The first effect was the promotion of the formation of the parasitic phase, $SrMoO_4$. This effect can be clearly seen in the GIXRD measurement shown in Figure 5-4. The second effect can be seen in the morphology of the Sr_2FeMoO_6 films. As shown in Figure 5-5 applying a higher laser power reduced the porosity on the Sr_2FeMoO_6 films, which is an interesting effect from the industrial point of view.

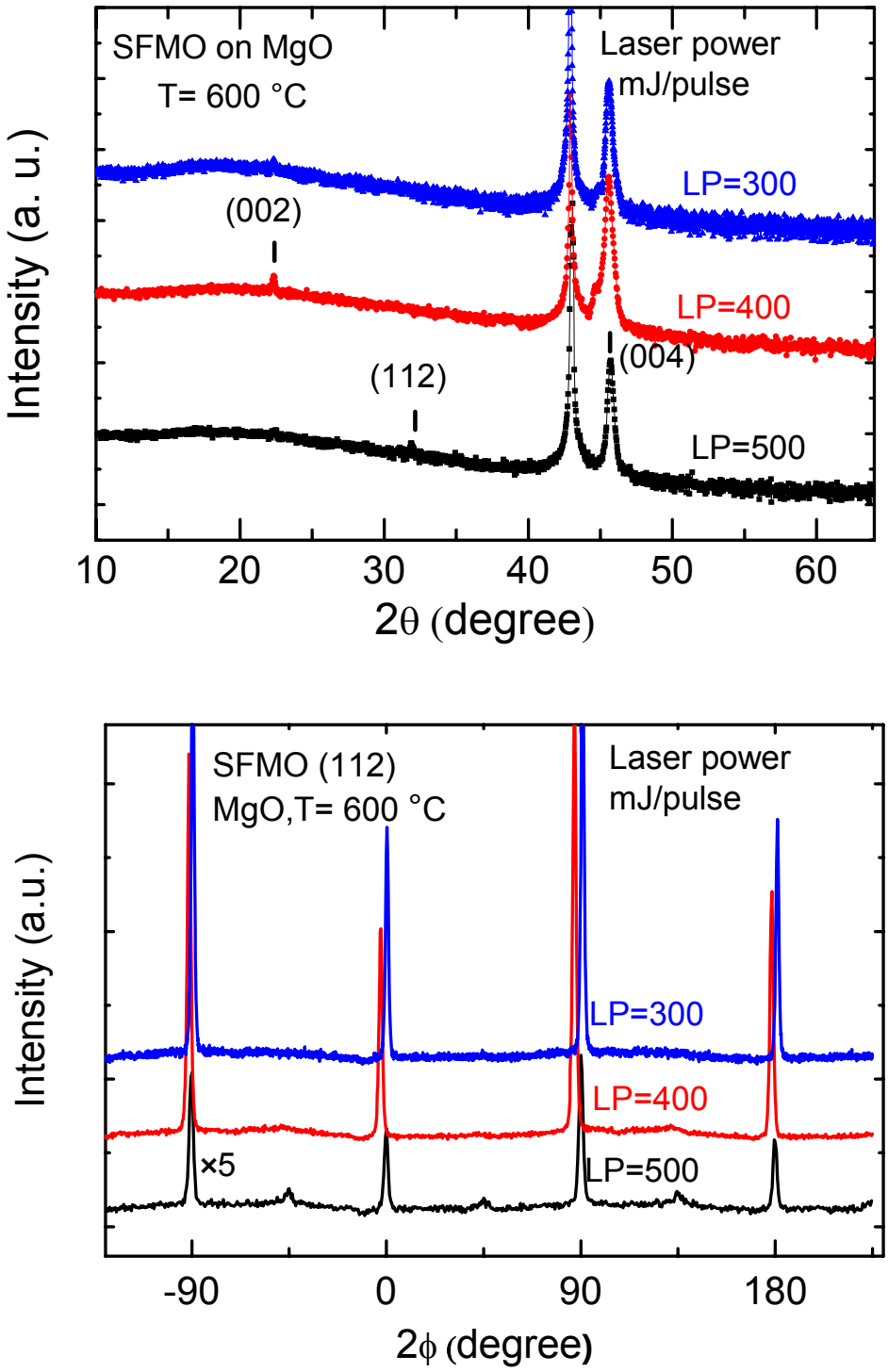

Figure 5-3: High resolution XRD (top) and Phi-Scan XRD (bottom) for Sr_2FeMoO_6 samples, grown at 600 ˚C, and different laser powers of 500 mJ/pulse, 400 mJ/pulse and 300 mJ/pulse shown by black curve (bottom curve), red curve (middle curve) and blue curve(top curve), respectively.

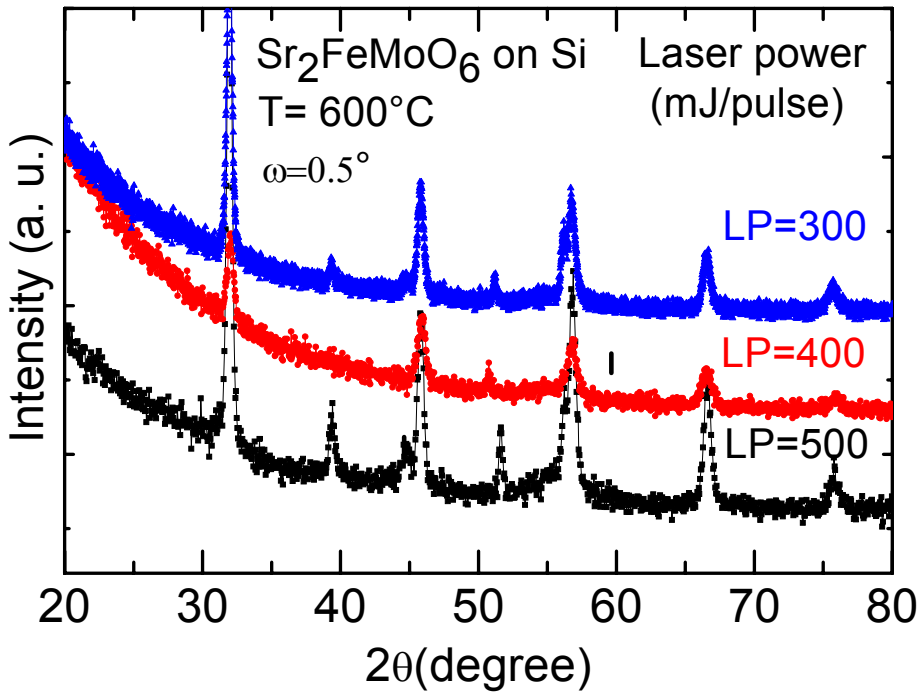

Figure 5-4: GIXRD of Sr_2FeMoO_6 grown on Si (100) with different laser power.

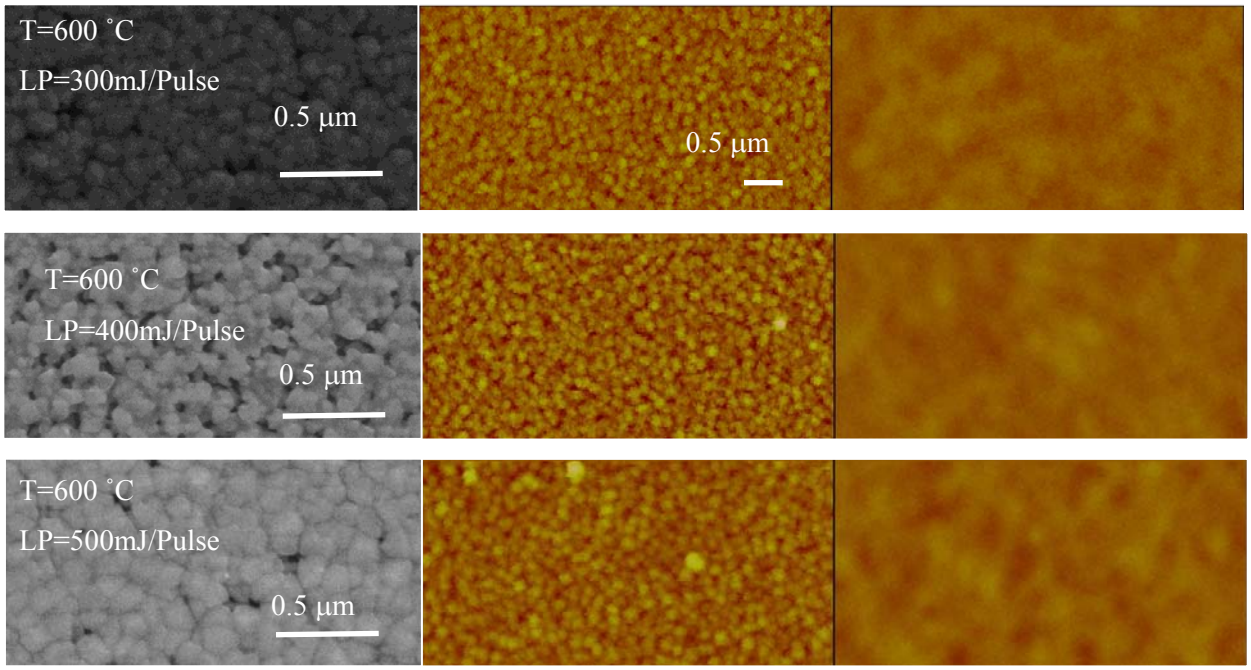

Figure 5-5: SEM (left column), AFM (middle column) and MFM (right column) of the Sr_2FeMoO_6 grown on Si (100) at different laser power.

Appendix B

Comparison of XPS spectra of Mo 3d of Sr_2FeMoO_6 grown on different substrates of MgO, $SrTiO_3$ and Si

As is shown in Section 3.3, Sr_2FeMoO_6 can be grown epitaxially on MgO and $SrTiO_3$ but not on Si, therefore expect single crystal with no or very low amount of grain boundaries on the Sr_2FeMoO_6 films grown on MgO and $SrTiO_3$ whereas a large amount of grain boundaries are expected for the polycrystalline Sr_2FeMoO_6 films grown on Si. It has been proposed by many groups that these grain boundaries contain secondary phases of $SrMoO_4$ or $SrMoO_3$. To investigate this further, the depth profile XPS of three samples were studied. To analyze those films grown on $SrTiO_3$ and MgO, films grown at a higher deposition temperature were chosen because they had the best quality, whereas Sr_2FeMoO_6 films grown at 600°C were chosen for Si (the magnetization data showed that the films deposited at a lower temperature have a larger coercive field therefore more grain boundaries). Figure 5-6 shows the percentage ratio of Mo^{6+}, Mo^{5+} and Mo^{4+} obtained from the respective fitted Mo 3d features for the films grown on MgO, $SrTiO_3$ and Si using CasaXPS. Surprisingly, the only difference that can be seen in these three graphs is a strong surface effect. For all the samples, regardless of their crystalline form Mo^{6+} has the highest value on the surface due to formation of $SrMoO_4$ on the surface (as we discussed in Section 3.3). Since the ratio of Mo ions for all the samples after approximately 160 s of sputtering time tend to have a constant ratio, it suggests that the grain boundary does not contain a secondary phase and it has the same nature as the grains.

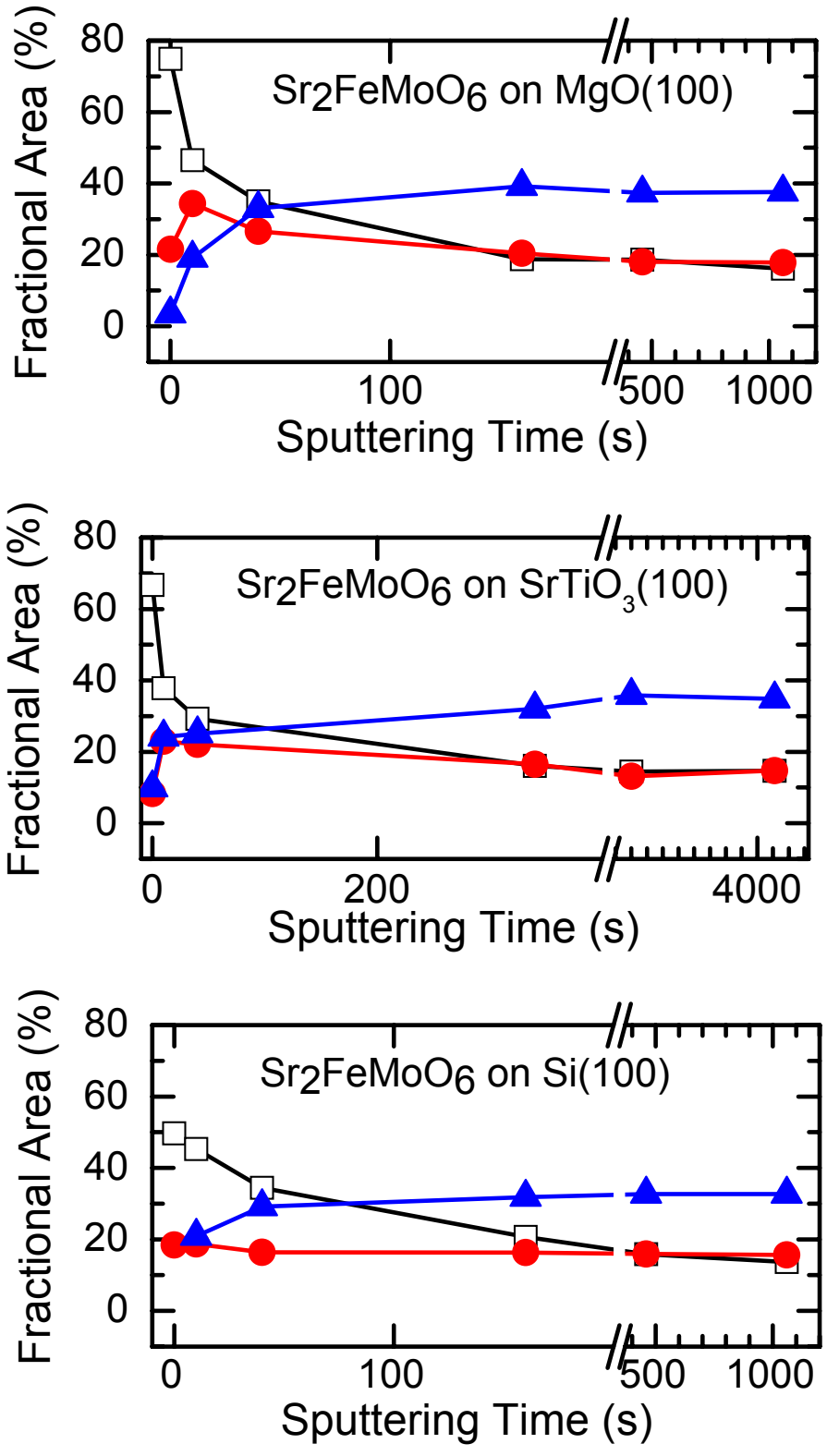

Figure 5-6: Relative intensity of Mo^{x+} as a function of sputtering time for as-grown Sr_2FeMoO_6 on MgO (top), $SrTiO_3$ (middle) and Si (bottom).

Appendix C

Comparison of magnetization and magnetoresistance of Sr_2FeMoO_6 deposited on MgO and $SrTiO_3$ at different growth temperatures

The effects of strain induced by substrates on epitaxially grown Sr_2FeMoO_6 films on MgO and $SrTiO_3$ (Sections 3.3,3.4) have been studied. Effects of the growth temperature on the physical properties of the Sr_2FeMoO_6 grown on these two substrates of MgO and $SrTiO_3$ have also been studied. Figure 5-7 shows the ω-2θ scan of Sr_2FeMoO_6 films deposited on (a) MgO(001) and (b) $SrTiO_3$ (100). The laser fluence was 400 mJ/pulse and the samples were grown at different temperature of 400°C, 600°C, 800°C. For the Sr_2FeMoO_6 films grown on the MgO substrates (Figure 5-7a), a lower deposition temperature (T=400°C) does not show any crystallinity and epitaxial growth can be observed for temperature higher than 600 °C. However, for the films grown on $SrTiO_3$ (Figure 5-7b), partial epitaxial growth can be seen at temperatures as low as 400°C. The magnetic properties of the two sets of films grown at 600°C and 800°C are compared in Figure 5-8. As has been discussed in Sections 3.3 and 3.4, a few groups have compared the magnetic properties of the Sr_2FeMoO_6 films grown on MgO and $SrTiO_3$ [80,106]. These reports show that either the magnetic moment of the film grown on MgO is smaller than that of the $SrTiO_3$ or that the substrate has no effect on the magnetic properties of the films. In contrast to the previous reports, our magnetization data shows that the magnetic moment of the films grown on MgO at 600 °C or 800 °C is clearly larger than the films grown on $SrTiO_3$. Films grown on MgO at 600 °C have a much larger coercive field compared to the film grown on $SrTiO_3$, and for the deposited films at higher temperature, the coercive field for both cases is the same. Figure 5-9 shows the resistance of the Sr_2FeMoO_6 samples grown on MgO and $SrTiO_3$, measured by a 4-point probe, under different applied magnetic fields of (a) H=500 Oe and (b) H=55000 Oe. The resistance of both films increase with decreasing temperature, showing semiconducting behaviour. A small kink can be observed around 80 K for MgO independent of the applied magnetic field, however for the film grown on $SrTiO_3$ substrate this kink is not being

observed at higher magnetic field. This kink has not been reported by other groups, and may be due to the magnetic impurities in the substrate, or perhaps an experimental artifact. It can be a subject of future studies.

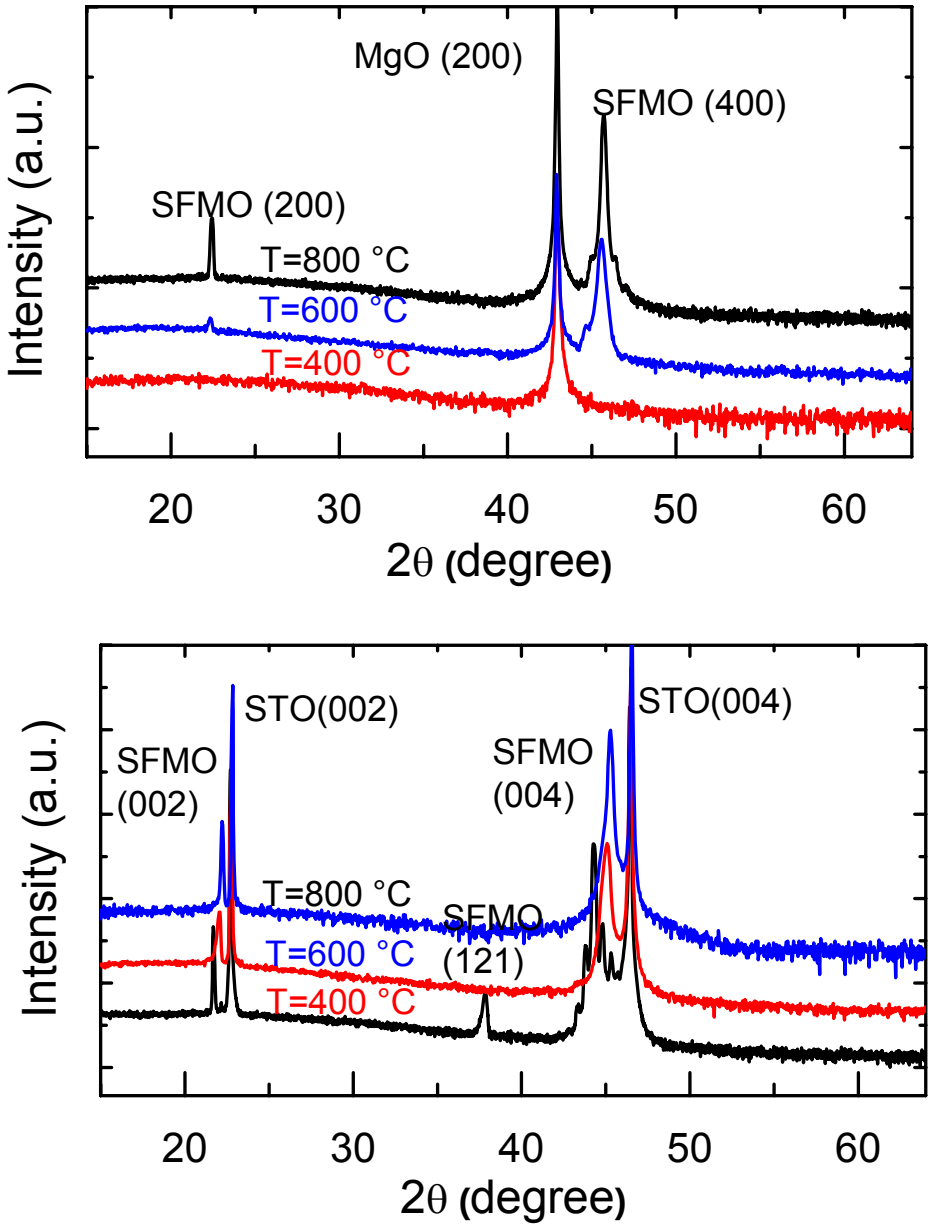

Figure 5-7: ω-2θ scan of Sr_2FeMoO_6 films deposited on (a) MgO (100) and (b) $SrTiO_3$ (100) in vacuum with a laser fluence of 400 mJ/ pulse at temperatures of 400°C, 600°C, 800°C.

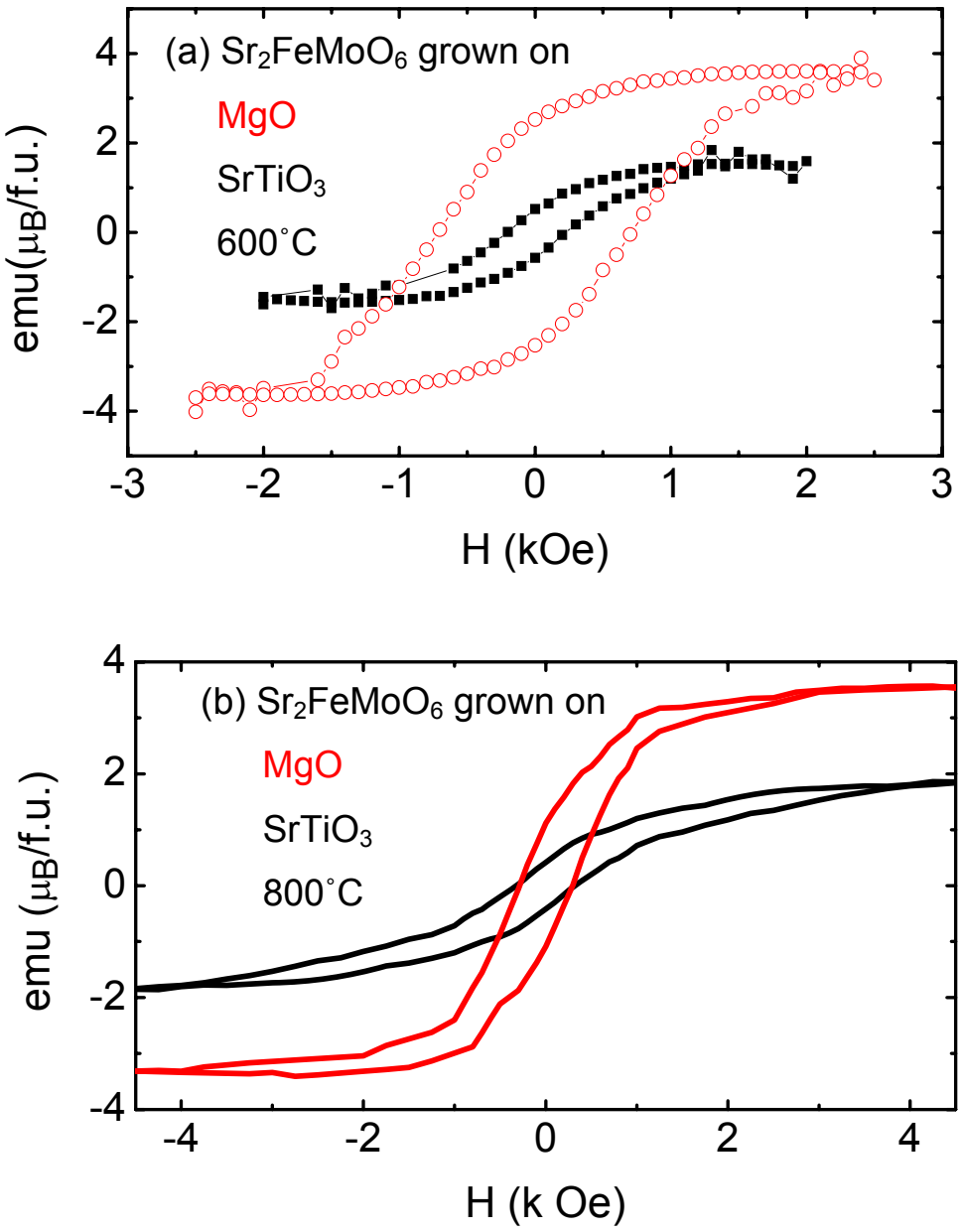

Figure 5-8: (a) Magnetization curve of Sr_2FeMoO_6 film deposited on MgO(001) and $SrTiO_3$ (100) in vacuum with laser fluence of 400 mJ/ pulse at (a) 600°C and (b) 800°C. The applied magnetic field was perpendicular to the c-axis of the Sr_2FeMoO_6 films.

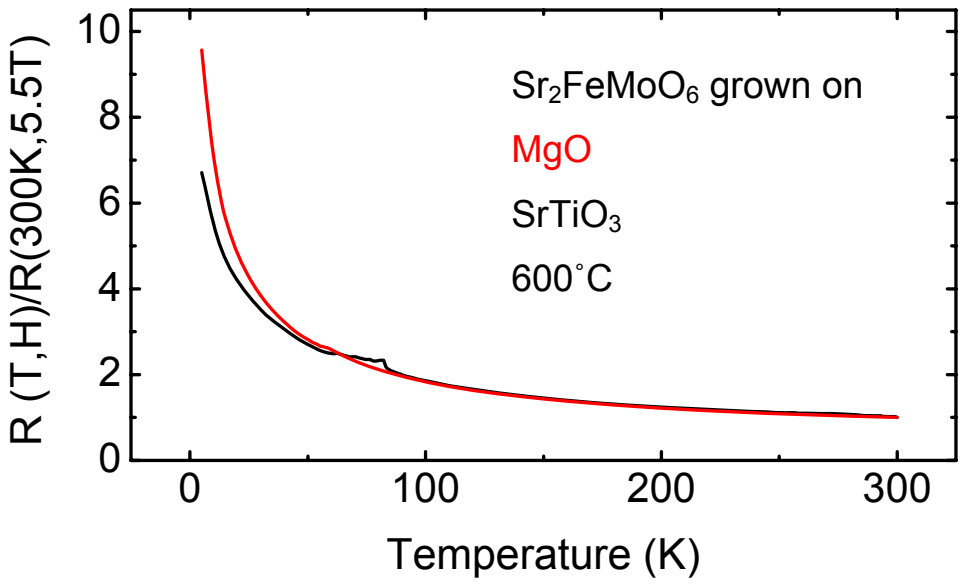

Figure 5-9: Resistance of Sr_2FeMoO_6 films grown on MgO (lower black curve) and STO (upper red curve) under an applied magnetic field of H=55000 Oe. The applied magnetic field was perpendicular to the c-axis of the Sr_2FeMoO_6 films.

References

[1] http://nobelprize.org/nobel_prizes/physics/laureates/2007/press.html.
[2] www.freescale.com.
[3] S. A. Wolf, D. D. Awschalom, R. A. Buhrman, J. M. Daughton, S. Von Molnar, M. L. Roukes, A. Y. Chtchelkanova, D. M. Treger, Science 294, 1488 (2001).
[4] J. S. Moodera, Colloquium , IQC , Waterloo, Auguest (2008).
[5] M. N. Baibich, J. M. Broto, A. Fert, F. Nguyen Van Dau, F. Petroff, P. Eitenne, G. Creuzet, A. Friederich, J. Chazelas, Phys. Rev. Lett. 61, 2472 (1988).
[6] G. Binasch, P. Grunberg, F. Saurenbach, W. Zinn, Phys. Rev. B. 39, 4828 (1989).
[7] W. Thomson, Proceedings of the Royal society of London, 81, 546 (1856).
[8] Nicola Spaldin, Magnetic materials, Fundemental and device applications, United Kingdom University Press, Cambridge (2003).
[9] N. F. Mott, Proc. Roy. Soc. A 153, 699 (1936).
[10] J. Kondo, Prog. Theor. Phys. 27, 772 (1962).
[11] A. Fert, I. A. Campbell, Phys. Rev. Lett. 21, 1190 (1986).
[12] G. Prinz, Science, 282, pp. 1660 (1998).
[13] R. A. de Groot, F. M. Mueller, P. G. Engen, K. H. J. Buschow, Phys. Rev. Lett. 50, 2024 (1983).
[14] J. M. D. Coey, M. Venkatesan, J. Appl. Phys.(invited talk) 91, 8345 (2002).
[15] K. Schwarz, J. Phys. F. 16, L211 (1986).
[16] K. –I. Kobayashi, T. Kimura, H. Sawada, K. Terakura, Y. Tokura, Nature, 395 (1998).
[17] C. Chappert, A. Fert, F. Nguyen Van Dau, Nature materials, 6, 813 (2007).
[18] M. Jullier, Phys. Lett. A 54 25 (1975).
[19] J. S. Moodera, L. R. Kinder, T. M. Wong, R. Meservey, Phys. Rev. Lett. 74, 3273 (1995).
[20] J. S. Moodera. G. Mathon, J. Magn. Magn. Mater. 200, 248 (1999).
[21] J.M. de Teresa, A. Barthelemy, A. Fert, J.P. Contour, F. Montaigne, and P. Seneor, Science 286, 507-509 (1999).
[22] D. B. Chrisey, G. K. Hubler, "Pulsed Laser Deposition of thin films", John Wiley & Sons. Inc. (1994).
[23] www.veeco.com.
[24] R. Wiesendanger" Scanning probe microscopy and spectroscopy: methods and applications", Cambridge [England]: Cambridge University Press (1994).
[25] www.chbe.gatech.edu/pandp/Jorge.ppt.
[26] R. F. Egerton, "Physical Priniples of Electron Microscopy", Springer Science+Business Media, Inc. (2005).
[27] M. Birkholz, "Thin film analysis by X-Ray scattering", Wiley-VCH Verlag GmbH & Co. KGaA, Wienheim (2006).
[28] A. Stierle. MPI fur metallforschung, X-Ray diffraction from surfaces, interfaces and thin films, summer school, July 4 (2005).
[29] I. Cernatescu, J. Woitok, B. Litteer, S. Wyma, Panalytical XRR and HRXRD presentation (2006).

[30] V. Holy, U. Pietsch, T. Baumbach, " High-Resolution X-Ray scattering from thin films and multilayers" Springer-Verlag Berlin Heidelber (1999).
[31] I. Cernatescu, Panalytical, Nanomaterial workshop, Waterloo (2007).
[32] http://www.chem.qmul.ac.uk/surfaces/scc/scat5_3.htm.
[33] M. McElfresh,"Fundamentals of mmagnetism and magnetic measurements featuring quantum design's magnetic property measurement system", Purdue University, Quantum design (1991).
[34] F. S. Galasso, Structure, Properties and preparation of Perovskite-type compounds Pergamon, London (1969).
[35] D. Serrate, J. M. De Teresa, M. R. Ibarra, J. Phys. :Condens. Matter, 9, 023201 (2007).
[36] D. Topwal, D. D. Sarma, H. Kato, Y. Tokura, M. Avignon, Phys. Rev. B 73, 094419 (2006).
[37] C. L. Yuan, Y. Zhu, P. P. Ong, J. Appl. Phys. 91, 4421 (2002).
[38] J. M. Michalik, J. M. De Teresa, D. Serrate, J. Blasco, M. R. Ibarra, J. Magn. Magn. Mater. 316, 413 (2007).
[39] H. Chang, M. Garcia-Hernandez, M. Retuerto, J. A. Alonso, Phys. Rev. B 73 104417 (2006).
[40] X. M. Feng, G. H. Rao, G. Y. Liu, H. F. Yang, W. F. Liu, Z. W. Ouyang, J. K. Liang, Physica B 344, 21 (2004).
[41] E. K. Hemry, G. V. M. Williams, H. J. Trodahl, J. Magn. Magn, Mater. 310, 1958 (2007).
[42] Y. Sui. X. J. Wang, Z. N. Qian, J. G. Cheng, Z. G. Liu, J. P. Miao, Y. Li, W. H. Su, C. K. Ong, Appl. Phys. Lett. 85, 269 (2004).
[43] D. Rubi, C. Frontera, J. Fontcuberta, M. Wojcik, E. Jedryka, C. Ritter, Phys. Rev. B. 70, 09445 (2004).
[44] F. Sriti, A. Maignan, C. Martin, B. Raveau, Chem. Mater. 13, 1746 (2001).
[45] W. Zhong, X. L. Wu, N. J. Tang, W. Liu, W. Chen, C. T. Au, Y. W. Du, Eur. Phys. J. B 41, 213 (2004).
[46] T. Okuda, K. –I. Kobayashi, Y. Tomioka, Y. Tokura, Phys. Rev. B 68, 144407 (2003).
[47] K. –I. Kobayashi, T. Kimura, Y. Tomioka, H. Sawada, K. Terakura, Phys. Rev. B. 59, 11159 (1999).
[48] A. Maignan, B. Raveau, C. Martin, M. Hervieu, J. Solid State Chem. 144, 224 (1999).
[49] T. Asaka, X. Z. Yu, Y. Tomioka, Y. Kaneko, T. Nagai, K. Kimoto, K. Ishizuka, Y. Tokura, Y. Matsui, Phys. Rev. B. 75, 184440 (2007).
[50] J. Linden, T. Yamamoto, M. Karppinen, H. Yamauchi, T. Pietari, Appl. Phys. Lett. 76, 2925 (2000).
[51] B. Garcia-Landa, C. Ritter, M. R. Ibarra, J. Blasco, P. A. Algarabel, R. Mahendiran, J. Garcia, Solid Stat Comm. 110, 435 (1999).
[52] M. Raekers, K. Kuepper, H. Hesse, I. Balasz, I. G. Deac, Constantinescu, E. Burzo, M. Valeanu, M. Neumann, J. Opto. Adv. Mater. 8, 455 (2006).
[53] D. D. Sarma, E. V. Sampathkumaran, S. Ray, R. Nagarajan, S. Majumdar, A. Kumar, G. Galini, T. N. Guru Row, Solid State Commun. 114, 465 (2000).

[54] LI. Balcells, J. Navarro, M. Bibes, A. Roig, B. Martinez, J. Fontcuberta, Appl. Phys. Lett. 78, 781 (2001).
[55] Y. Tomioka, T. Okuda, Y. Okimoto, R. Kumai,, K.-I. Kobayashi, Phys. Rev. B 61, 422 (2000).
[56] Y-H. Huang, H. Yamauchi, M. Karppinen, Phys. Rev. B 74, 174418 (2006).
[57] H. Q. Yin, J. –S, Zhou, J. –P, Zhou, R. Dass, J. T. McDevitt, J. B. Goodenough, App. Phys. Lett. 75, 2812 (1999).
[58] A. Di Trolio, R. Larciprete, A. M. Testa, D. Fiorani, P. Imperatori, S. Turchini, N. Zema, J. Appl. Phys. 100, 013907 (2006).
[59] T. Manako, M. Izumi, Y. Konishi, K.-I. Kobayashi, M. Kawasaki, Y. Tokura, Appl. Phys. Lett. 74, 2215 (1999).
[60] M. Gracia-Hernandez, J. L. Martinez, M. J. Martinez-Lope, M. T. Casais, J. A. Alonso, Phys. Rev. Lett. 86, 24443 (2001).
[61] J. Navarro, L. I. Balcells, F. Sandiumenge, M. Bibes, A. Roig, B. Martinez and J. Foncuberta, J. Phys. Condens. Matter 13, 8481 (2001).
[62] T. Saha-Dasgupta, D. D. Sarma, Phys. Rev. B 64, 064408 (2001).
[63] D. Stoeffler, S. Colis, Mater. Sci. Eng. B, 126, 133 (2006).
[64] A. S. Ogale, S. B. Ogale, R. Ramesh, T. Venkatesan, Appl. Phys. Lett. 75,537 (1999).
[65] D. Niebieskikwiat, A. Caneiro, R. D. Sanchez, J. Fontcuberta, Phys. Rev. B 64,180406 (2001).
[66] Y. Sui, X. Zhang, X. Wang, J. Cheng, W. Su, J. Tang, J. Appl. Phys. 102, 023903 (2007).
[67] J. L. MacManus-Driscoll, A. Sharma, Y. Bugolslavsky, W. Branford, L. F. Cohen, M. Wei, Adv. Mater. 18, 900 (2006).
[68] D. D. Sarma, P. Mahadevan, T. Saha-Dasgupta, S. Ray, A. Kumar, Phys. Rev. Lett. 18, 2549 (2000).
[69] W. Zhong, W. Liu, C. T. Au, Y.W. Du, Nanotechnology, 17, 250 (2006).
[70] H. Asano, M. Osugi, Y. Kohara, D. Higashida, M. Matsui, Jpn. J. Appl. Phys. 40, 4883 (2001).
[71] W. Zhong, W. Liu, C. T. Au, Y.W. Du, Nanotechnology 17, 250 (2006).
[72] J. Santiso, A. Figueras, J. Fraxedas, Surf. Interface Anal. 33, 676 (2002).
[73] Q. Gan, R. A. Rao, C. B. Eom, J. L. Garrett, M. Lee, Appl. Phys. Lett. 72, 978 (1998).
[74] C. U. Jung, H. Yamada, M. Kawasaki, Y. Tokura, Appl. Phys. Lett. 84, 2590 (2004).
[75] U. Gebhardt, N. V. Kasper, A. Vigliante, P. Wochner, H. Dosch,, F. S. Razavi, H. –U. Habermeier, Phys. Rev. Lett. 98, 096101 (2007).
[76] R. B. Praus, G. M. Gross, F. S. Razavi, H, -U. Habermeier, J. Magn. Magn. Mater. 211, 41 (2000).
[77] F. S. Razavi, G. V. Sudhakar Rao, H. Jalili, H, -U. Habermeier, Appl. Phys. Lett. 88, 174103 (2006).
[78] M. Besse, F. Pailloux, A. Barthelemy, K. Bouzehouane, A. Fert, J. Olivier, O. Durand, F. Wyczisk, R. Bisaro, J.–P. Contour, J. Crys. Growth 241, 448 (2002).
[79] K. Szot, W. Speier, R. Carius, U. Zastrow and W. Beyer, Phys. Rev. Lett. 88, 077508 (2002).

[80] R. P. Borges, S. Lhostis, M. A. Bari, J. J. Versluijs, J. G. Lunnes, J. M. D. Coey, M. Besse, J. –P. Contour, Thin Solid Films, 429, 5 (2003) .
[81] L. Y. Zhao, H. Jalili, N. Panjwani, T. Chan, Z. H. He, N. F. Heinig, K. T. Leung, Electrochemical and Solid-State Lett. 10, K47 (2007).
[82] P. E. J. S. Zhang, L. D. Yao, F. Y. Li, Z. X. Bao, J. X. Li, Y. C. Li, J. Liu, C. Q. Jin, R. C. Yu, J. Mater. Sci. 41, 7374 (2006).
[83] M. F. Doerner, S. Bernnan, J. Appl. Phys. 63, 126 (1988).
[84] M. F. Toney, T. C. Huang, S. Brennan and Z. Rek, J. Mater. Res. 3, 351 (1988).
[85] S. Debnath, P. Predecki, R. Suryanarayan, Pharmaceutical Research 21 , 149 (2004).
[86] T. C. Huang, Advances in X-Ray Analysis 33, 91 (1990).
[87] K. Omote, J. Harada, Advances in X-Ray Analysis 43, 223 (2000).
[88] H. Jalili, N. F. Heinig, K. T. Leung, (2008), to be submitted.
[89] M. Besse, F. Pailloux, A. Barthelemy, K. Bouzehouane, A. Fert, J. Olivier, O. Durand, F. Wyczisk, R. Bisaro, J. –P. Contour, J. Crys. Growth 241, 448 (2002).
[90] S. Ray, P. Mahadevan, A. Kumar, D. D. Sarma, R. Cimino, m. Pedio, L. Ferrari, A. Pesci, Phys. Rev. B 67, 085109 (2003).
[91] K. Kuepper, M. Kadiroglu, A. V. Postnikov, K. C. Prince, M. Matteucci, V. R. Galakhov, H. Hesse, G. Borstel, M. Neumann, J. Phys.:Condens. Matter 17, 4309 (2005). Also: K. Kuepper, I. Balasz, H. Hesse, A. Winiarski, K. C. Prince, M. Matteucci, D. Wett, R. Szargan, E. Burzom, M. Neumann, Phys. Stat. Sol. 201, 3252 (2004).
[92] R. Polini, A. Falsetti, E. Traversa, O. Schaf, P. Knauth, J. Euro. Ceram. Soc. 27, 4291 (2007).
[93] P. Wang, L. Yao, M. Wang, W. Wu, J. Alloys and compounds 311, 53 (2000).
[94] J. C. Sczancoski, L. S. Cavalcante, M. R. Joya, J. A. Varela, P. S. Pizani, E. Longo, Chem. Eng. J. 140, 632 (2008).
[95] J.F. Moulder, W.F. Stickle, P.E. Sobol, K.D. Bomben, "Handbook of X-ray Photoelectron Spectroscopy", 2nd ed., J. Chastain (ed.), Perkin-Elmer Corp., Eden-Prairie, MN (1992).
[96] T. Choudhury, S.O. Saied, J.L. Sullivan, A.M. Abbot, J. Phys. D 22, 1185 (1989).
[97] J. Santiso, A. Figueras, J. Fraxedas, Surf. Interface Anal. 33, 676 (2002).
[98] A. Katrib, V. Logie, M. Peter, P. Wehrer, L. Hilaire, G. Maire, J. Chim. Phys. 94, 1923 (1997).
[99] D. Rubi, J. Navarro, J. Fontcuberta, M. Izquierdo, J. Avila, M. C. Asensio, J. Phys. Chem. Solid 67, 575 (2006).
[100] A. Katrib, V. Logie, M. peter, P Wehrer, L. Hilaire, G. Maire, J. Chim. Phys. 94, 1923 (1997).
[101] H. Jalili, N. F. Heinig, K. T. Leung, J. Appl. Phys., in press (2009).
[102] S. R. Shinde, S. B. Ogale, R. L. Greene, T. Venatesan, K. Tsoi, S. –W. Cheong, A. J. Millis, J. Appl. Phys. 93, 1605 (2003).
[103] D. Sanchez, M. Garcia-Hernandez, N. Auth, G. Jacob, J. Appl. Phys. 96, 2736 (2004).
[104] A. Venimadhav, M. E. Vickers, M. G. Blamire, Solid State Comm, 130, 631 (2004).
[105] J. Venable, "Introduction to Surface and Thin Film Processes", Oxford Uni. Press, (2000).

[106] R. Boucher, J. Phys. and Chem. of Solids, 66, 1020 (2005).
[107] Panalytical Expert Epitaxy. X'Pert MRD application.
[108] W. Westerburg, D. Reisinger, G. Jakob, Phys. Rev. B, 62, R767 (2000).
[109] T. Fix, D. Stoeffler, S. Colis, C. Ulhaq, G. Versini, J. P. Vola, F. Huber, A. Dinia, J. Appl. Phys. 98, 023712 (2005).
[110] H. Asano, S. B. Ogale, J. Garrison, A. Orozco, Y. H. Li, E. Li, V. Smolyaninova, C. Galley, M. Downes, M. Rajeswari, R.. Ramesh, T. Venkatesan, Appl. Phys. Lett. 74, 3696 (1999).
[111] E. Gommert, H. Cerva, J.Wecker, K.Samwer, J. Appl. Phys., 85(8), 5417 (1999).
[112] J. M. Coey, M. Venkatesan, J. Appl. Phys. 91, 10 (2002).
[113] B.L. Chamberland, CRC Crit. Rev. Solid State Mater. Sci. 7, 1 (1977).
[114] A. Gupta, J. Z. Sun, J. Magn. Magn. Mater. 200, 24 (1999).
[115] K. Schwarz, J. Phys. F: Met. Phys. 16, L211 (1986).
[116] K. P. Kämper, W. Schmitt , G. Güntherodt, R. J. Gambino, R. Ruf, Phys. Rev. Lett. 59, 2788 (1987).
[117] A. Korotin, V. I. Anisimov, D. I. Khomskii, G. A. Sawatzky, Phys. Rev. Lett. 80, 4305 (1998).
[118] S. P. Lewis, . B. Allen, T. Sasaki, Phys. Rev. B, 55, 10253 (1997).
[119] I. I. Mazin, D. J. Singh, C. Ambrosch-Draxl. Phys. Rev. B, 59, 411 (1999).
[120] P. S. Robbert, H. Geisler, C. A. Ventrice, Jr. J. Van Ek, S. Chaturvedi, J. A. Rodriguez, M. Kuhn, U. Diebold , J. Vac. Sci. Tech. A 16, 990, (1998).
[121] A. Barry, J. M. D. Coey, M. Viret, J. Phys.: Condens. Matter 12, L173 (2000).
[122] X. W. Li, A Gupta, G. Xiao, Appl. Phys. Lett. 75, 713 (1999).
[123] B. Kubota, J. Am. Ceram. Soc. 44, 247 (1961).
[124] Y. Shibasaki, F. Kanamaru, M. Koizumi, S. Kume, J. Am. Ceram. Soc., 56 248 (1973).
[125] M. P. McDaneil, Catal. 33, 47 (1985).
[126] B. K. Miremadi, R. C. Singh, Z. Chen, S. Roy Morrison, K. Colbow, Sensors Actuators B 21, 1 (1994).
[127] M. W. Mensch, C. M. Byrd, D. F. Cox, Catal. Today 85, 279 (2003).
[128] R. O. Adamas, J. vac. Sci. Technol. A 1, 12 (1983).
[129] R.C. DeVries, Mat. Res. Bull. 1, 83 (1966).
[130] L. Ranno, A. Barry, J. M. D. Coey, J. Appl. Phys. 81, 5774 (1997).
[131] S. Ishibashi, T. Namikawa, M. Satou, Mat. Res. Bull. 14, 51, (1979).
[132] K. Suzuki, P. M. Tedrow, Phys. Rev. B 58, 11597 (1998).
[133] N. J. C. Ingle, R. H. Hammond, M. R. Beasley, J. Appl. Phys. 89, 4631 (2001).
[134] P. G. Ivanov, Ph.D. thesis, Florida State University, Tallahassee (2002).
[135] M. Shima, T. Tepper, C. A. Ross, J. Appl. Phys. 91, 7920 (2002).
[136] D. Stanoi, G. Socol, C. Grigorescu, F. Guinneton, O. Monnereau, L. Tortet, T. Zhang, I. N. Milailescu, Mater. Sci. Eng. B 118, 74 (2005).
[137] N. Popovici, M. L. Parames, R. C. Da Silva, O. Monnereau, P. M. Sousa, A. J. Silvestre, O. Conde, Appl. Phys. A: Materials Science & Processing 79, 1409 (2004).
[138] N. Umada, H. Yanagihara, A. Hatanaka, E. Kita, Jpn. J. Appl. Phys. 44, 6538 (2005).

[139] S. J. Liu, J. Y. Juang, K. H. Wu, T. M. Uen, Y. S. Gou, J. Y. Lin, Appl. Phys. Lett. 80, 4202 (2002).
[140] M. Shima, T. Tepper, C. A. Ross, J. Appl. Phys. 91, 7920 (2002).
[141] D. Stanoi, G. Socol, C. Grigorescu, F. Guinneton, O. Monnereau, L. Tortet, T. Zhang, I. N. Milailescu, Mater. Sci. Eng. B 118, 74 (2005).
[142] PDF22004 (Highscore)
[143] N. Umada, H. Yanagihara, A. Hatanaka, E. Kita, Jap. Soc. Appl. Phys. 44, 6538 (2005).
[144] T. Yu, Z. X. Shen, J. He, W. X. Sun, S. H. Tang, J. Y. Lin, J. Appl. Phys. 93, 7 (2003).
[145] T. Tsutsumi, I. Ikemoto, T. Namikawa, H. Kurdo, Bull. Chem. Soc. Jpn. 54, 913 (1981).
[146] H. Jalili, N. F. Heinig, K. T. Leung, Mater. Res. Proc. Symp. Proc. 998 (2007).
[147] H. A. Bullen, S. J. Garrett, Surf. Sci. Spect. 8, 3 (2001); H. A. Bullen, S. J. Garrett, Chem. Mater. 14, 243 (2002).
[148] B. Liu, Y. Fang, M. Terano, J. Mol. Catal. A: Chemical 219, 165 (2004).
[149] R. Cheng, B. Xu, C. N. Borca, A. Scokolov, C. S. Yang, L. Yuan, S. H. Liou, B. Doudin, P. A. Dowben, Appl. Phys. Lett. 79, 3122 (2001).
[150] I. Ikemoto, K. Ishii, S. Kinoshita, H. Kuroda, M. A. Alarofranco, J. M. Thomas, J. Solid State Chem. 17, 425 (1978).
[151] E. Brand, D. Kellett, M. D. Enever, J. T. Fellows, R. G. Egdell, J. Mater. Chem. 15, 1141 (2005).
[152] M. C. Biesinger, C. Brown, J. R. Mycroft, R. D. Davidson, N. S. McIntyre, Surf. Interf. Anal. 36, 1550 (2004).
[153] D.J. Kester and R. Messier, J. Appl. Phys. 72, 504 (1992).
[154] H. Asano, N. Koduka, K. Imaeda, M. Sugiyama, M. Matsui, IEEE Trans. Magn. 41, 2811 (2005).
[155] M. Bibes, K. Bouzehouane, A. Barthelemy, M. Besse, S. Fusil, M. Bowen, P. Seneor, J. Carrey, V. Cros, A. Vaures, J. –P. Contour, A. Fert, Appl. Phys. Lett. 83, 2629 (2003).
[156] T. Fix, D. Stoeffler, Y. Henry, S. Colis, A. Dinia, T. Dimopoulos, L. Bar, J. Wecker, J. Appl. Phys. 99, 08J107 (2006).